DESIGNING OF A GRID TIE INVERTER FOR COMMERCIAL AND HOUSEHOLD SOLAR POWER INSTALLATIONS BASED ON A SOLID-STATE TRANSFORMER TOPOLOGY

Paranagamage Shirosh Ayeshmantha Peiris

(139515H)

Degree of Master of Science

Department of Electrical Engineering

University of Moratuwa

Sri Lanka

January 2018

DESIGNING OF A GRID TIE INVERTER FOR COMMERCIAL AND HOUSEHOLD SOLAR POWER INSTALLATIONS BASED ON A SOLID-STATE TRANSFORMER TOPOLOGY

Paranagamage Shirosh Ayeshmantha Peiris

(139515H)

Thesis/Dissertation submitted in partial fulfillment of the requirements for the degree Master of Science

Department of Electrical Engineering

University of Moratuwa

Sri Lanka

January 2018

Declaration

I declare that this is my own work and this thesis/dissertation does not incorporate without acknowledgement any material previously submitted for a Degree or Diploma in any other University or institute of higher learning and to the best of my knowledge and belief it does not contain any material previously published or written by another person except where the acknowledgement is made in the text.

Also, I hereby grant to University of Moratuwa the non-exclusive right to reproduce and distribute my thesis/dissertation, in whole or in part in print, electronic or other medium. I retain the right to use this content in whole or part in future works (such as articles or books).

…….. ……

Signature of the candidate Date:

The above candidate has carried out research for the Masters Dissertation under my supervision.

…… ……

Signature of the supervisor: Date

(Dr L.N.W Arachchige)

…… ……

Signature of the supervisor: Date

(Dr H.M.Wijekoon)

Abstract

Solar PV installations have gained a rapid popularity in Sri Lanka due to the reduction of PV panel costs and government incentives to promote renewable energy. The presence of these PV inverters has introduced power quality problems at the LV grid, mainly due to the injection of harmonics and DC currents.

The objective of this thesis is to study the power quality issues of the existing transformerless inverters and propose a solar PV inverter configuration based on a solid-state transformer (SST) topology. Upon recognizing the drawbacks of the existing configurations, three inverter configurations were developed based on the dual active bridge (DAB) and Tri active bridge (TAB) configurations utilized in the solid-state transformer.

Two configurations for the DAB based inverter are presented. Mathematical modelling of the TAB converter is presented with its associated converter currents and voltages. Based on the mathematical model, controllers were derived to maintain the DC bus voltages and the power flow of the TAB. Output filter designs, MPPT algorithm selection, power flow controllers and PV array selection procedures are presented along with the inverter configurations.

The developed systems were simulated and compared with the transformerless system in the MATLAB Simulink platform to assess their improvements. The load side harmonic isolation capabilities and the fault current limiting capabilities of the DAB and TAB based PV inverter systems are presented. The TAB and transformerless systems were also simulated with the presence of grid voltage harmonics. In all the cases tested, the TAB based system provides excellent power quality and fault current limiting capabilities over the transformerless system.

Dedication

Dedicated to my loving parents, wife and daughter

Acknowledgement

My sincere gratitude goes to my supervisors, Dr H.M. Wijekoon (Chief Engineer-Transmission Planning, Ceylon Electricity Board) and Dr Lidula Widanagama Arachchige (Senior Lecturer, University of Moratuwa) for continuously encouraging and guiding me throughout this research. If not for their continued guidance and inspiration, none of this would have been possible.

Next, I would also like to thank the Mr Ronald Commester (Deputy General Manager, R&D Branch, Ceylon Electricity Board) for allowing me to utilize the resources of the R&D branch of CEB to carry out my research.

I would also like to thank all the staff at the department of electrical engineering in providing me support to complete this research. Being the friendliest department in the university, the guidance provided by the academic staff during the progress reviews were immensely helpful during my research.

Most importantly, this dissertation would not have been possible unless the understanding, encouragement and patience provided by my wife Nimashi and my parents Jayantha Peiris and Suneetha Peiris. Therefore, I owe my deepest gratitude to them.

Table of Contents

List of Figures

List of Tables

List of Abbreviations

AAC	All aluminum conductor
CEB	Ceylon Electricity Board
DAB	Dual active bridge
HF	High frequency
IGBT	Insulated gate bipolar junction transistor
KCL	Kirchhoff's current law
KVL	Kirchhoff's voltage law
LECO	Lanka Electricity Company
MOSFET	Metal oxide field effect transistor
MPP	Maximum power point
MPPT	Maximum power point tracking
P&O	Perturb and observe
PCC	Point of common coupling
PI	Proportional integral
PSM	Phase shift modulation
PV	Photovoltaic
PWM	Pulse with modulation
RMS	Root mean square
SST	Solid state transformer
SVM	Space vector modulation
TAB	Tri active bridge
TDD	Total demand distortion
THD	Total harmonic distortion

1 INTRODUCTION

1.1 Background

Renewable energy and Solar based power generation has recently started to gain popularity among the commercial and household electricity consumers in Sri Lanka. Increase of electricity tariffs, reduced PV panel costs and availability of solar insolation throughout the year has made Solar PV installations popular among the other renewable energy sources. Apart from net metering options, hybrid solar installations with battery banks and diesel generators are also gaining popularity.

The net metering scheme was introduced to the public by CEB (Ceylon Electricity Board) and LECO (Lanka Electricity Company) in the year of 2008 as an effort to promote renewable energy and give the opportunity for its customers to participate in the electricity production. This allowed consumers to generate power to satisfy their own demand while supplying the excess energy to the grid. As of 30th April 2014, the solar PV penetration of Sri Lanka had reached up to 6.1 MW totaling to 1041 installations. Out of the 6.1 MW, around 5 MW was being generated from the western province [1] . By the year 2015 the number of consumers increased from 1041 to 3025, reaching a total of 5029 in the year of 2016. The current total generation is 31 MW amounting to a 46.4% increase with respect to the previous year [2] . This shows a rapid increase in the PV penetration. With the recent introduction of the low interest loan schemes by CEB and LECO, and the government induced promotional projects like “Surya Bala Sangramaya,”, these figures are expected to increase exponentially.

However, the presence of solar power at the LV distribution grid is known to cause power quality problems. Harmonic distortion, electromagnetic interference, frequency and power fluctuation, inrush currents are some of the known power quality problems associated with the solar PV installations [3] . These power quality issues can be varied with the type of inverter that is utilized to interface solar PV installations to the grid.

The Solid-State Transformer (SST) is a novel power conversion device that incorporates multiple AC-DC, DC-DC and DC-AC conversion stages providing galvanic isolation with the use of a high frequency transformer. The main advantages

include, active and reactive power flow control, power factor correction, harmonic resistance, fault Isolation and communication interfaces. Furthermore, availability of DC-DC conversion stage provides a DC power port for integration of DC power sources. Utilizing these conversion stages for a solar power inverter provides the above-mentioned advantages. The Dual active bridge and Tri active bridge arrangements of the solid-state transformer can be utilized to integrate the energy storage and the PV panels with isolation.

1.2 Problem Statement

Even though, the CEB and LECO have stringent connection code, due to lack of post commissioning assessment of solar PV generation, which have been connected to CEB and LECO distribution network under net metering scheme, many net metering consumers have used inverters with poor power quality at the output. Thus, a proper assessment has to be conducted among the solar PV installations in Sri Lanka to assess the impact on power quality due to the type of inverters used. Among most of the inverters that are being used, transformerless inverters are popular due to their modularity and compactness. However, they also pose power quality problems such as, injection of DC power to the grid and the presence of harmonics. Thus, investigation of power quality issues in existing solar PV generation under net metering schemes and proposing a solution to reduce the impact on power quality for future solar PV integration is a timely requirement.

1.3 Objectives

The overall objective of this research is to investigate the power quality issues associated with the inter-connection of solar PV to the utility, and propose effective solutions to overcome them. This goal is achieved by fulfilling a number of specific objectives:

1. Assessing the impact on the system power quality when solar PV is integrated using currently available inverters.

2. Developing a novel inverter topology based on the solid-state transformer topologies to minimize the impact on system power quality.

1.4 Thesis Overview

Thesis is focused on developing a grid tied solar PV inverter based on dual active and tri active bridge arrangements. MPPT algorithms and controllers were utilized to extract the maximum power from the PV panel and provide it to the grid. Controllers were built to regulate the DC voltages and power flow.

This chapter provides the introduction, giving the background information with the problem statement and the research objectives. The rest of the report is organized as follows:

Chapter 2 presents the literature review, covering the areas of:

- Transformerless inverter
- Solid state transformer topologies
- Grid tie inverter topologies
- Maximum power point tracking technologies

The methodology and the outcome of the investigation on power quality issues with existing grid-tie inverters is presented in Chapter 3. Chapter 4 is focused on designing the transformerless inverter with PV panels, MPPT controllers and the grid tie inverter. MATLAB Simulink Simulation software was used to design and simulate the system parameters and to demonstrate the results. The design of the dual active bridge controllers and its two arrangements are discussed in Chapter 5. Chapter 6 and Chapter 7 contains the mathematical modeling and controller design of the tri active bridge and its design in Simulink involving the other controllers of the PV system and household.

Finally, the simulation results, comparisons, major conclusions, and several suggestions for future research are highlighted in Chapter 8 and 9.

2 LITREATURE REVIEW

The objective of this literature review is to identify the drawbacks of the existing transformerless system and study about other technologies that can be utilized to eliminate its drawbacks.

The first section describes the transformerless inverter operation and its drawbacks when compared to high frequency (HF) transformer isolated systems. The second describes the solid-state transformer and its various topologies. The operation and advantages of the core component of the solid-state transformer which includes the dual active bridge and triple active bridge is described.

The other two sections contain information about the grid tie inverter topologies and maximum power point tracking algorithms.

2.1 Transformerless PV arrangement

The transformerless inverter is the most commonly used inverter topology for Solar PV generation in Sri Lanka. it can be easily implemented, due to the simplicity in design and reduced component count. The system usually consists of a PV panel, boost converter and a grid tie inverter. The boost converter increases the PV panel output voltage and feeds it to the grid tie inverter in order to supply power to the grid. The boost converter switching is driven by a maximum power point (MPPT) algorithm that maintains the output voltage of the PV panel at a specific value to extract the maximum power from the panel. If the voltage output of the PV array lie above the grid peak voltage at all operating states, it can be directly connected to the Grid Tie inverter with a DC link capacitor [4] .

The transformerless system imposes a set of problems when compared with the other high frequency transformer isolated systems. The mainly discussed problem is the common mode leakage current. The stray capacitance of the PV panels forms a closed circuit current loop through the PV panel, inverter and the filter circuit. The magnitude of the current loop can vary based on the stray capacitance created by the PV panel frame structure, weather conditions, dust and humidity. This leakage current raises concerns over the safety issues and creates electromagnetic interferences, losses

and grid current ripples. Lin ma, et al. [5] have presented an analysis on the leakage currents of the transformerless inverters with a comparison of different modulation technologies used. T. Kheng, et al. [6] have presented a comparison of multiple inverter topologies along with their leakage current generation. Out of the compared systems, only the galvanically isolated HF transformer systems completely eliminate the leakage current.

The presence of a galvanic closed loop poses another safety concern over the DC faults occurring at the PV panel side. As no isolation is present, the DC faults at the PV array can be fed by the grid causing large currents to flow through the inverter freewheeling diodes and the DC bus.

The other issue observed is the DC current injection. V. Salas, et al. [7] have presented a comparison of the DC current injection between transformerless and HF transformer isolated systems concluding that the HF transformer isolated system preforms better in terms of minimizing DC current injection. The presence of DC offset is harmful for the distribution transformers and creates additional harmonics in the grid current and voltage leading to reduced power quality.

2.2 Solid-State Transformer

The solid-state transformer (SST) is a novel power conversion device incorporated in smart grid applications to replace the conventional power transformer. It can be utilized in solar PV systems to connect PV panels with HF transformer isolation. B. Liu, et al. [8] have presented a Solid-state transformer based solar PV system using dual half bridge converters stating its advantages over the conventional arrangements. N.C Foureaux, et al. [9] have presented a modular converter based on a SST topology that overcome the drawbacks of the central inverter arrangement used in utility scale power plants. A modular multilevel SST topology is also presented with increased power density and improved MPPT performance.

The construction of the SST consists of switching devices to control and direct power flow through the high frequency transformer which provides galvanic isolation similar to a conventional transformer. The use of the high frequency transformer

drastically improves its power density while maintaining a good efficiency. The switching devices and the active nature of the devices provide much better controllability and flexibility. Some of the main advantages of the solid-state transformer include

- Smaller size and less weight
- Fault isolation and fault management
- Power factor correction
- Active and reactive power flow control
- Good voltage regulation capabilities
- Ability to incorporate DC inputs and outputs
- Communication interfaces to exchange information with other devices of the system
- No propagation of harmonics from either side

The disadvantages are increased complexity in control and limited power capability due to the limits imposed by the voltage ratings and power handling capabilities of the switching devices. However recent introduction of Silicon Carbide (SiC) switching devices combined with multilevel topologies have addressed this problem to a greater extent.

2.2.1 Known topologies

There are mainly four topologies found in literature for the solid-state transformer [10] . The first topology is known as the single stage, where the conversion is provided using a high frequency transformer without a DC stage. This is shown in Figure 2.1. The 50 Hz AC voltage is switched using a full bridge to high frequency AC and fed through the transformer. Both ends of the winding incorporate full bridge converters for frequency conversion to facilitate bidirectional power flow. Even though the component count and the complexity are low in this topology, the lack of a DC stage prevents PV integration, reactive power control and power factor correction while requiring large filters to eliminate harmonics. In addition to this, the fluctuations

in voltage at one side are transferred to the other similar to a conventional transformer [11] .

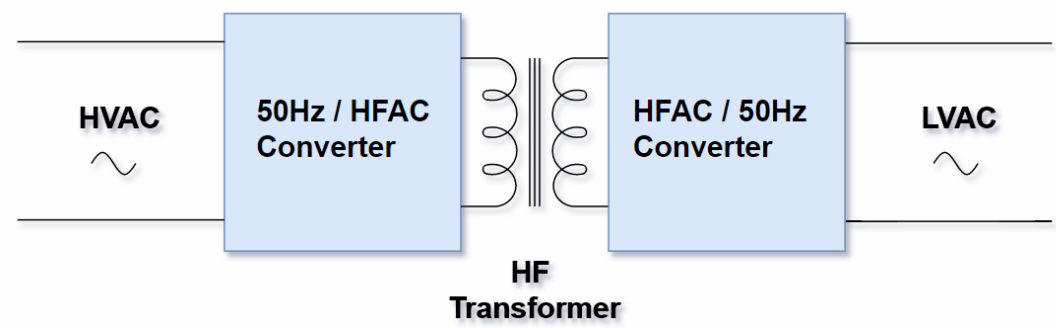

Figure 2.1: Single stage SST

The second and third topologies shown in Figure 2.2 incorporate a DC stage in either the HV or LV sides with one side of the HF transformer having a direct HFAC to 50 Hz AC conversion. This provides a DC bus for distributed resources interconnection. However, since the other side directly converts HFAC to 50 Hz, it requires large filters and contribute to harmonic generation. Reactive power flow control and power factor correction is possible only at one side (HV or LV side with DC bus).

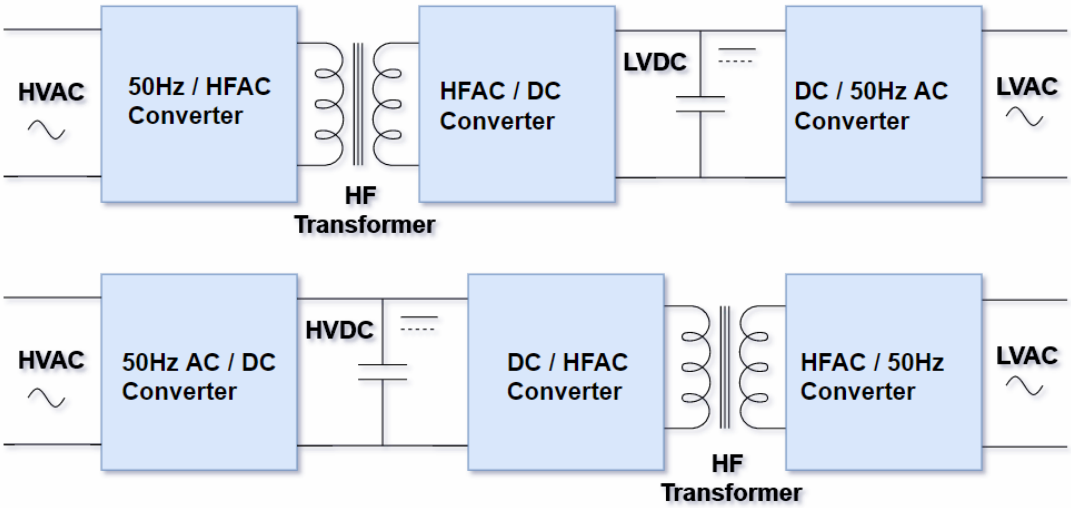

Figure 2.2: Two stage SST configurations

Having three conversion stages, the third topology is known as the three-stage topology and it is shown in Figure 2.3. This incorporates two DC buses in either sides of the HF transformer. The 50 Hz AC is converted into DC and then converted to

HFAC and provided to the HF transformer. This topology is more common and is widely utilized in most of the designs. The DC stages allow distributed resource interconnection with isolation which is an advantage for micro-grids. Since the 50 Hz conversion is from DC, it provides good voltage regulation capabilities with reduced harmonics.

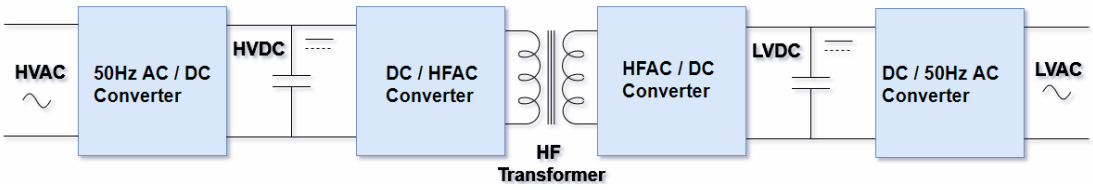

Figure 2.3: Three stage SST

2.2.2 Dual active bridge.

The Dual active bridge (DAB) is the core component of the three-stage solid-state transformer. It consists of two active bridges connected through a high frequency transformer creating the DC to DC conversion stage of the SST. The two active bridges convert the DC into HFAC or HFAC into DC based on the direction of the power flow. The duty ratio of each bridge is maintained at 50 % while the power transfer is controlled by generating a phase shift between the voltage waveforms of the two active bridges. W.A.A Doneker [12] has presented a relationship between the power flow and phase shift with detailed descriptions on the soft switching boundaries of the DAB. D.S. Segaran [13] has presented a harmonic model for the output voltage of the DAB by applying Kirchhoff's voltage law (KVL) to the current flowing through the HF transformer and the converters.

One advantage of this system is that the DAB can operate in both buck and boost mode without a change in construction. Furthermore, by tuning the snubber circuit capacitances with the transformer leakage inductance, soft switching can be obtained to reduce the devices ratings.

The DAB can also be used with a power storage such as super capacitors to smooth out power oscillations caused by PV panels. S. Poshtkouhi, et al. [14] have

shown that a lithium ion ultra-capacitor can be used to provide power at intermittent irradiance variations to maintain the power quality at the output. However, the application is for nano-grids that employ micro inverters in the 100 W scale. Furthermore, integrating battery storage with isolation needs additional conversion circuits as the voltage at the PV panel side varies continuously with the irradiance and temperature. Therefore, similar integrations of a larger scale can be more conveniently done with galvanic isolation using the triple active bridge.

2.2.3 Triple active bridge

The Triple active bridge (TAB) is an extension to the dual active bridge. A three-winding high frequency transformer is used with an additional full bridge converter. Similar to the other two ports, HFAC to DC conversion and vice versa provides bidirectional power flow. The ability to have different transformer ratios allow connection of distributed resources with different voltage ratings. Multiple configurations can be found in literature for this arrangement. J. Duarte [15] has presented a system that integrates a fuel cell, load and grid using a TAB. The power flow control is achieved by mathematically computing the phase shift required to transfer the power from one port to the other. A Δ-Π transformation of the equivalent circuit of the three-winding transformer is also presented with only leakage and magnetic inductances taken into consideration.

Similar to the dual active bridge, soft switching can be achieved in the TAB to minimize the ratings of the switching devices [12] . But this requires voltages among the ports to be identical with identical transformer ratios.

In additional to the triple active bridge, quad active and other multi active bridges can also be implemented. A quad active bridge is presented by S. Falcones [16] integrating a PV panel and battery storage with grid and loads. The presented system also includes a gyrator based averaging model to determine the power flow throughout individual ports. However, it also shows that as the number of ports increase above four, the controller complexity drastically increases, making the design impractical.

The above studies were mainly focused on managing the power flow of the TAB. The power quality improvements and fault isolation capabilities of the TAB needs to be investigated using detailed simulations and mathematical models.

2.3 Grid-Tie Inverter

The grid tie inverter is the DC to 50 Hz AC conversion stage of the PV system. The most common and simplest approach is the H-Bridge inverter with sinusoidal PWM. The main requirement is to provide active power flow control and minimize harmonic generation.

Many topologies have been developed to improve harmonic generation. N.A Rahim [17] has presented a 7-level inverter with level shifted PWM as the modulation technique. While maintaining the switching device configuration similar to the H-bridge, the input DC bus is divided to sections using a capacitor voltage divider. The voltage divider arrangement provides seven different voltage levels to the H-Bridge through two more additional switching devices. The switching pulses are generated by comparing three level shifted reference waveforms with a single carrier. This arrangement reduces devices stresses while reducing the THD of voltage in half over the 3-step inverter.

Another approach is using space vector modulation (SVM). SVM is known to have a good DC bus utilization and improved harmonic spectrum. It is commonly implemented in three phase systems. In the three phase SVM, the 8 switching states of a three-leg inverter are represented as vectors of a hexagon. A reference vector is usually generated by transforming the reference three-phase system into a single rotating vector using the $\alpha\beta0$ transform. This rotating vector is placed in the middle of the hexagon and synthesized using two adjacent vectors to generate the turn on and turn off times of the respective switching devices.

This approach can also be used for single phase systems. In a single-phase system with an H-Bridge, there are only 4 switching states. These four switching states are represented on a line where the reference vector moves back and forth. They are synthesized by the adjacent vectors to generate the timing of the switching pulses [18]

. The switching states used in single phase and three phase SVM are shown in Figure 2.4.

Single phase space vector modulation is not very common in literature. H. Dehbonei [19] has compared the existing unipolar sinusoidal PWM and single phase SVM and demonstrated that they both exhibit a similar harmonic spectrum, thus making it less advantageous in a single-phase system.

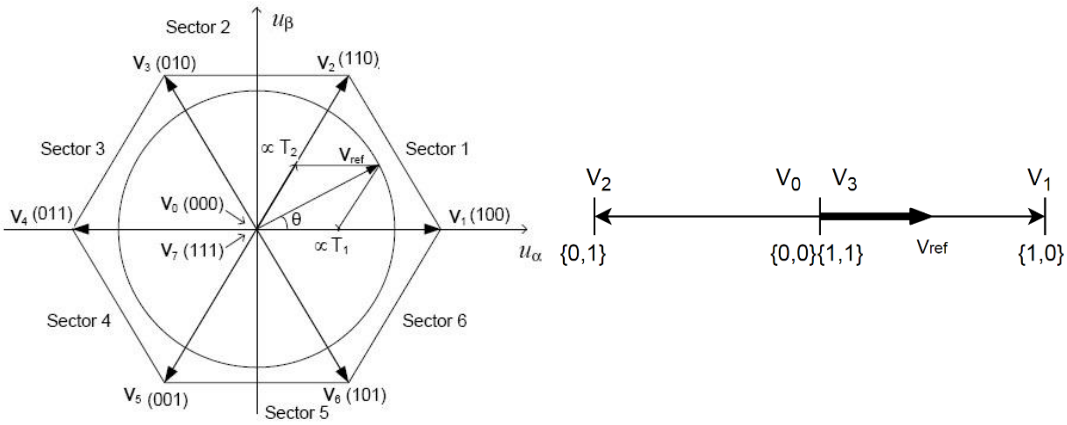

Figure 2.4: Three phase and single-phase space vector modulation

However, the controller complexity and switch count increases with these arrangements. Bidirectional power flow is difficult to achieve as most of these inverter topologies are mainly designed for unidirectional power flow. For a low voltage single-phase application, a H bridge inverter with unipolar sinusoidal PWM is more suited. As the grid tie inverter in this application is connected to a DC output of a SST, good voltage regulation reduces the harmonics generated. A properly tuned LCL filter can be used to eliminate the other higher order harmonics generated due to switching.

2.4 Maximum Power Point Tracking (MPPT)

The power output of the PV panel changes with varying irradiance and temperature. Usually the P-V and the I-V characteristic of a PV panel are given in the manufacturers datasheet with standard test conditions. The P-V characteristic usually shows a gradual increase of power with voltage until its maximum power point is reached. Upon reaching the maximum power point, the power output rapidly decreases with increasing DC output voltage. Typical P-V and I-V characteristics of a Mitsubishi 185 W PV panel are shown in Figure 2.5.

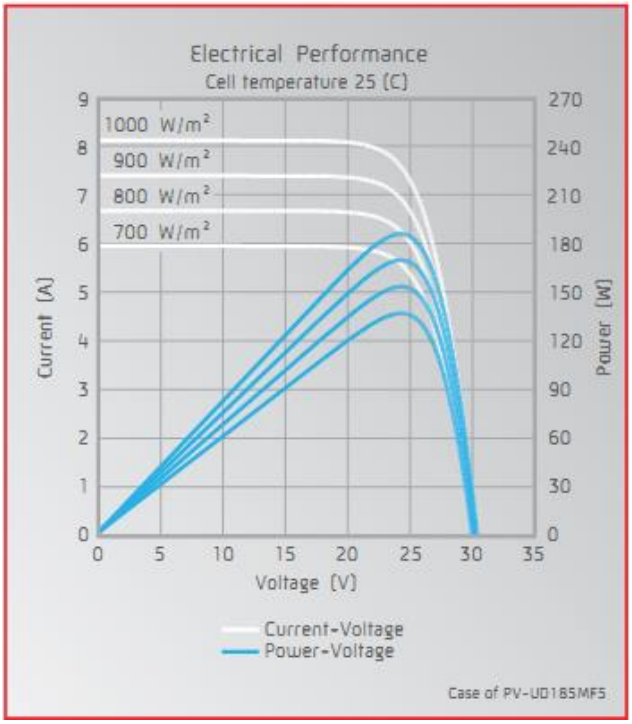

Figure 2.5: MPPT characteristic for power and voltage [20]

This characteristic shows that maintaining a specific voltage in the output DC bus is critical to extract the maximum power out of the PV array. Therefore, it is necessary to use an algorithm to maintain this output DC voltage by controlling the output of the boost converter or the grid tie inverter.

Various algorithms can be found in literature. Perturb and Observe, Incremental conductance, Current sweep, Fractional open circuit voltage [21] are commonly used. In addition Kalman filter based MPPT algorithms [22] , can also be found in literature.

The perturb and observe algorithm is the simplest and most commonly used MPPT algorithm. The algorithm measures the output power and voltage and compares the current value with the previous (n-1) condition. Based on the power output variation, the voltage is either increased or decreased until the maximum power point is reached. However, even at the maximum power output the voltage and power output get subjected to oscillations as the algorithm continuously compares the current power output with the previous (n-1) value.

The incremental conductance algorithm, on the other hand measures the incremental change of current and voltage individually and generate the voltage increments. It also measures the rate of change of current with respect to voltage (incremental conductance) to speed up the algorithm. This is known to respond faster for irradiance variations compared to the Perturb and Observe algorithm. However similar to the P&O algorithm, this also generates slight oscillations at the maximum power point.

The fractional open circuit method is based on the fact that the maximum power point voltage is a fraction of the open circuit voltage. This factional constant depends on the characteristics of the PV array used. However, in order to make use of this algorithm, the PV panel current has to be interrupted momentarily to measure the open circuit voltage. Furthermore, due to the fact that the fractional constant is not an exact figure, the maximum power point estimate has less accuracy. [23]

The current sweep method uses a current sweep to determine the I-V characteristic, and calculates the maximum power point through computation. The current sweep in this method takes around 50 ms to execute, thereby resulting in some loss of power during the sweep period. [23]

Many other algorithms can be found in literature. However out of all these algorithms. P&O and Incremental conductance are found to be the most popular due to the simplicity in implementation and higher accuracy.

This concludes the literature review of this thesis. The next chapter describes the outcomes of the power quality investigation conducted on existing transformerless inverters in Sri Lanka.

3 EXISTING INVERTERTS: PERFORMANCE EVALUATION

Located near the equator, Sri Lanka receives ample of solar insolation throughout the year making solar PV a good power generation option. The advancements in the technology and widespread use have resulted in rapid decline in Solar PV prices making the solution more attractive to the consumers and utilities. Utility-scale solar installations are with a capacity usually above 1 MW requiring large, open land areas. Residences, commercial, and industrial buildings are installing roof-top solar PV systems with a capacity usually less than 1 MW. Currently, there are three different schemes being practiced for rooftop solar PV introduced by the utility providers (Ceylon Electricity Board (CEB) & Lanka Electricity Company (LECO)), naming Net-metering, Net-Accounting and Net-Plus while Net-metering scheme being the most popular scheme among residential consumers. As the household loads are minimal at daytime, the net metering scheme allowed the consumers to balance their night-time energy consumption over the daytime generation facilitating a reduction on their overall electricity bill.

Even though the standards are imposed on the solar power generation schemes, a recent set of measurement carried out by the research and development branch of the CEB indicated that the majority of the inverters were generating current and voltage harmonics above the specified TDD and THD limits [24] . However, a detailed study on the individual harmonics, DC offsets and voltage measurement had to be carried out to get a comprehensive measure on the power quality issues with the integration of rooftop solar PV.

Since the first part of the thesis is to assess the existing solar arrangements, a survey was carried out to assess the power quality output of several commercial solar PV installations. Different types of solar PV installations were identified and field measurements were carried out to assess their impact on the grid power quality.

3.1 Applicable Standards

The CEB guidelines indicate that the Solar PV installations should comply with the IEEE 519:2014 standard [25] .

According to the guidelines, since the PV inverter falls into the power generation equipment category, the applicable Total Demand Distortion (TDD) current limits fall into the $I_{sc}/I_L>20$ category of the standard. The scope of this study, is limited to the solar PV installations connected at the low voltage (LV, 230V line to ground) voltage buses. Therefore, the voltage Total Harmonic Distortion (THD) limits applicable are within the $V \leq 1.0\ kV$ category.

In addition to the harmonic limits specified, the CEB grid code has limited the DC current injection to be less than 1% of the fundamental [26] .The Harmonic limits stated in the IEEE 519:2014 standard are shown in Table 3.1 and Table 3.2.

Table 3.1: Voltage distortion limits

Bus Voltage V at PCC	**Individual harmonics (%)**	**Total Harmonic distortion THD (%)**
$V \leq 1.0\ kV$	5.0	8.0
$1kV \leq V \leq 69.0\ kV$	3.0	5.0

Table 3.2: Current distortion limits (120 V through 69 kV systems)

Maximum harmonic current distortion in percent of I_L						
Individual harmonic order (odd harmonics) [a,b]						
I_{sc}/I_L	$3 \leq h < 11$	$11 \leq h < 17$	$17 \leq h < 23$	$23 \leq h < 35$	$35 \leq h < 50$	**TDD**
<20[c]	4.0	2.0	1.5	0.6	0.3	5.0
20<50	7.0	3.5	2.5	1.0	0.5	5.0
20<100	10.0	4.5	4.0	1.5	0.7	12
100<1000	12.0	5.5	5.0	2.0	1.0	15
>1000	15.0	7.0	6.0	2.5	1.4	20

[a]Even harmonics are limited to 25% of odd harmonic limit above

[b]Current distortion that result in a dc offset e.g half wave converters are not allowed

[c]All power generation equipment is limited to these values of currents distortions regardless of actual I_{SC}/I_L

where I_{SC} – Maximum short-circuit current at PCC

I_L – Maximum demand load current (fundamental frequency components) at PCC under normal operating condition

3.2 Measuring Instrument

The instrument used for measurements was a Fluke 430 Series II power quality analyzer which is shown in Figure 3.1. This instrument is capable of measuring harmonics of voltage and current up to the 50th order of the fundamental. This also provides the 90th, 95th and 99th percentile of harmonic measurements making it easier to compare with the standard. In addition to this RMS (root mean square) voltage and current, harmonics and flicker can be measured. TDD can also be calculated by the software provided for the instrument. As the primary requirement was to measure the current and voltage harmonics, this instrument deemed suitable for the measurement.

Figure 3.1: Fluke 430 Series II power quality analyzer

3.3 Measurement Setup

There are two types of inverters installed in the Sri Lankan households. The majority of them are central inverters which contain a strings of PV panels connected to a central grid tie inverter. The other type is the micro inverter type where the power of each panel is generated by an individual micro-inverter. The advantage of micro inverter is that it provides good efficiency at partial shading of the panels. This is not very useful for rooftop PV installations as they employ only a small area compared to

utility scale installations. Anyhow, central inverters are more popular as their cost of installation is relatively low.

Both of these inverter arrangements do not provide any form of galvanic isolation for the PV panels. The inverters are directly connected to the grid through a circuit breaker.

For this study, the measurements were taken from the point of common coupling(PCC) where the output of the PV inverter and the household were connected to the Grid. The existing PV arrangement and the measurement configuration is shown in Figure 3.2. The two colors blue and yellow are used to distinguish the consumer and utility side components. The voltage probes of the instrument were used to directly measure the grid voltage while a current probe based on the Rogowski principle was used to measure the inverter current output.

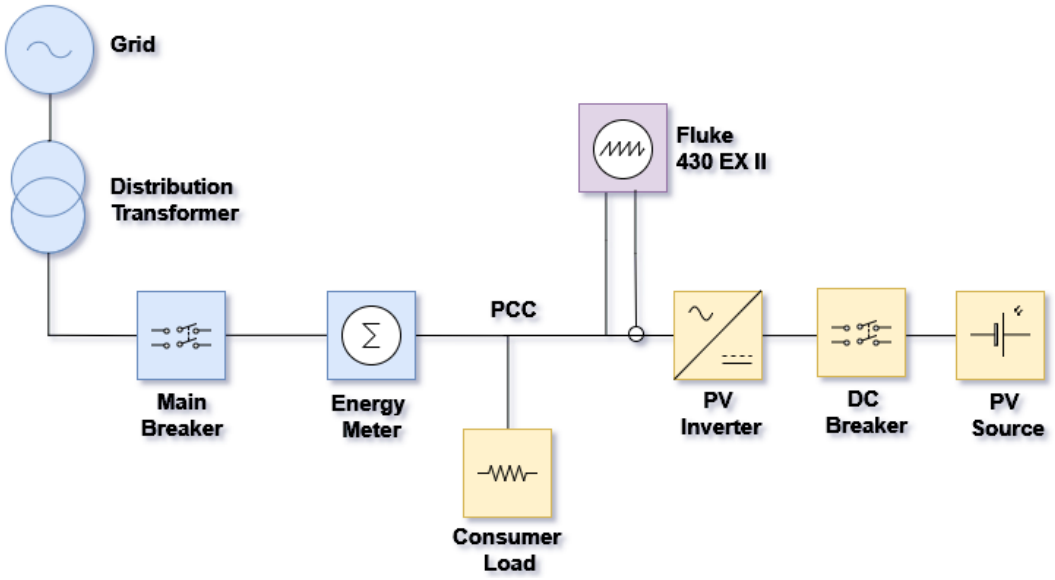

Figure 3.2: Measurement setup

Measurements were carried out on three 2 kW transformerless commercial inverters in the Piliyandala area of Sri Lanka. Measurements were conducted for one hour with a measurement resolution of 200 ms. THD of Voltage, TDD of current, DC current injection and power output variations were recorded.

3.4 Measurements and Analysis

3.4.1 Inverter No 1

This inverter was operating at half of its maximum power output due to the cloud cover and lack of irradiance. The power output and voltage variations of the inverter are shown in Figure 3.3 and Figure 3.4. The maximum power output for the measured period reached 1100 W. Occasional dips in power output can be observed with changes of irradiance. Similarly, the grid voltage has been subjected to irradiance variations but the total drop had not been more than 3 V.

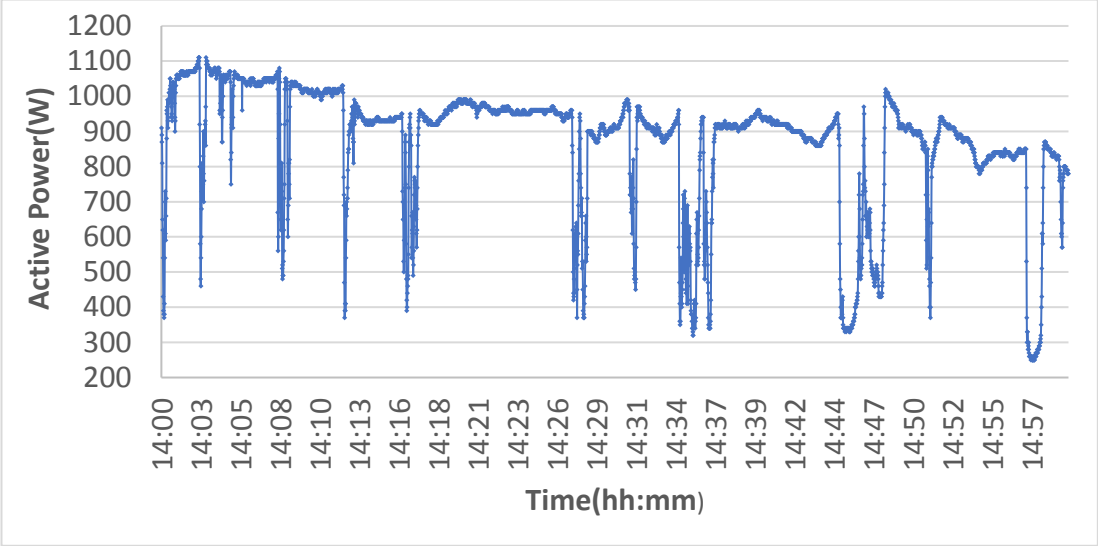

Figure 3.3: Measured active power output of "Inverter No 1"

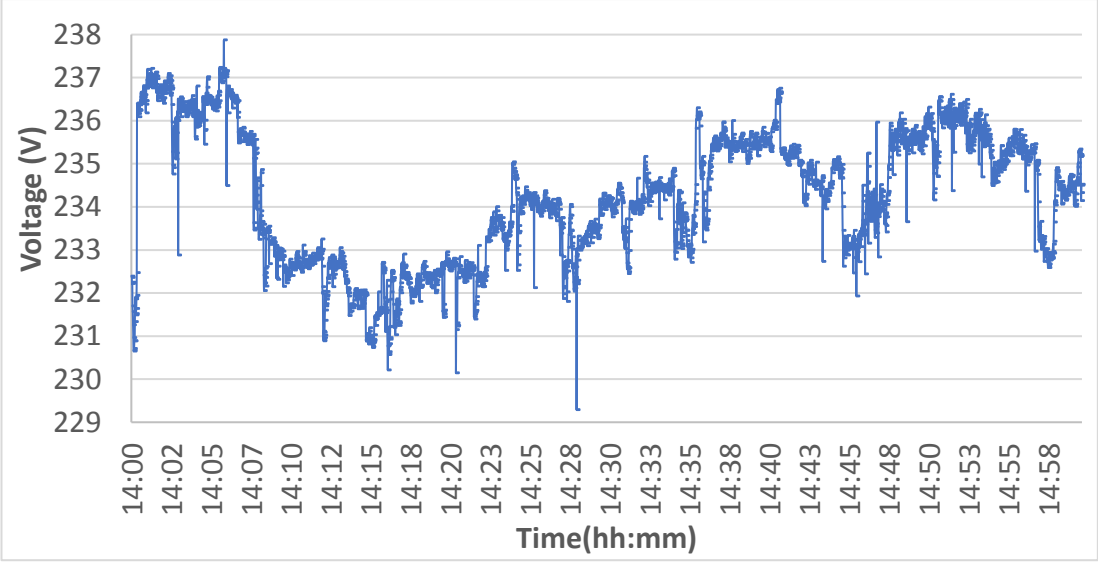

Figure 3.4: Measured inverter terminal voltage "Inverter No 1"

The harmonic variations of Inverter No. 1, are shown in Figure 3.5 and Figure 3.6. The THD measurement of voltage varied in a range of 2.2% to 2.4% while the TDD varied from 4.2% to 4.7%. The TDD of the inverter had exceeded the harmonic limit of 5% during the irradiance transients. However, when considering the overall measurement, the average value of TDD stayed below the accepted limits given in Table 3.2.

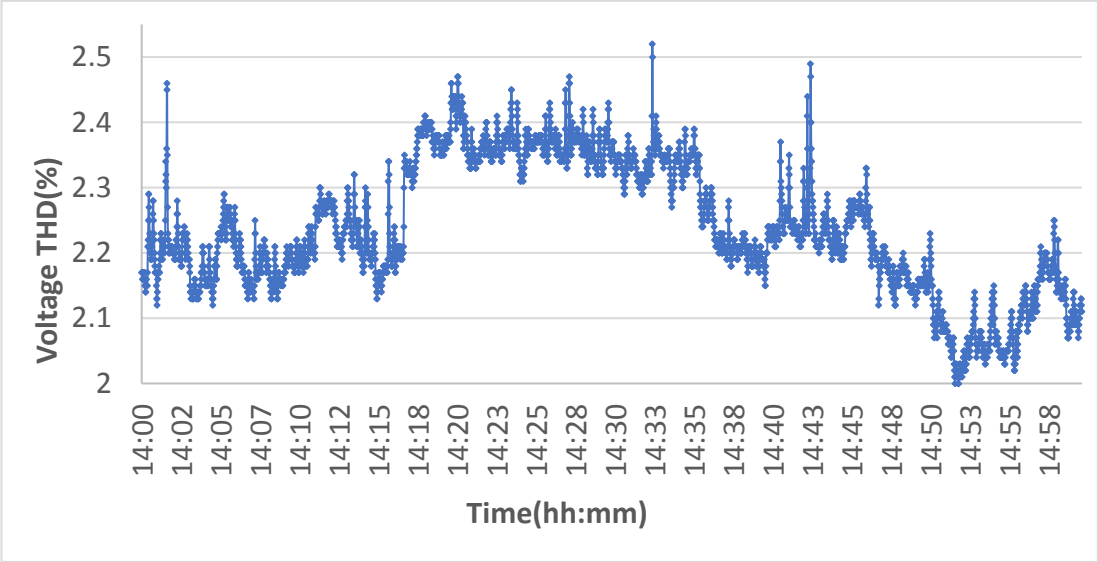

Figure 3.5: Voltage THD of "Inverter No. 1."

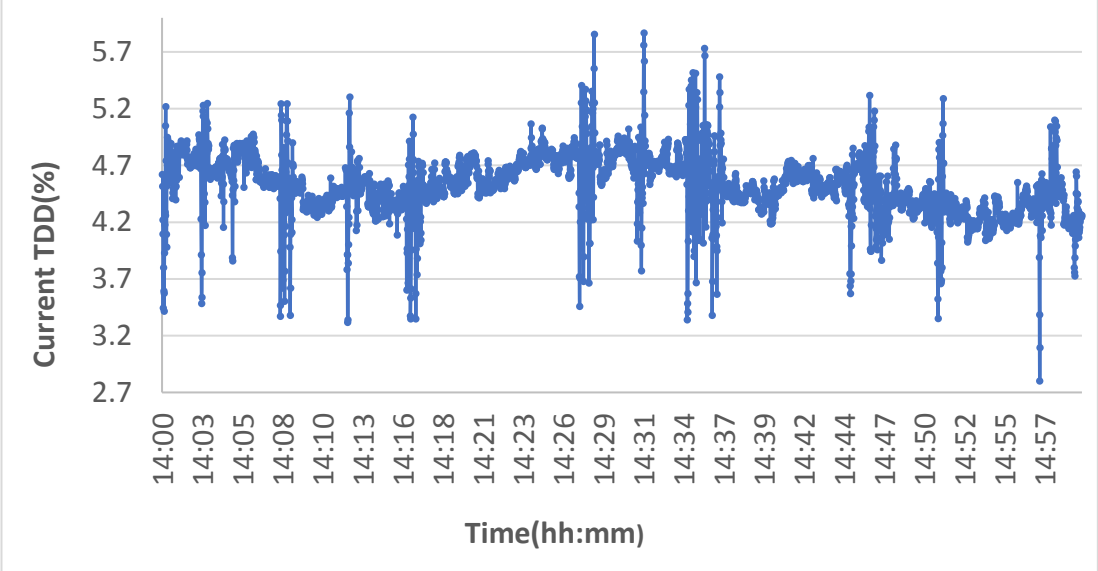

Figure 3.6: Current TDD of "Inverter No. 1."

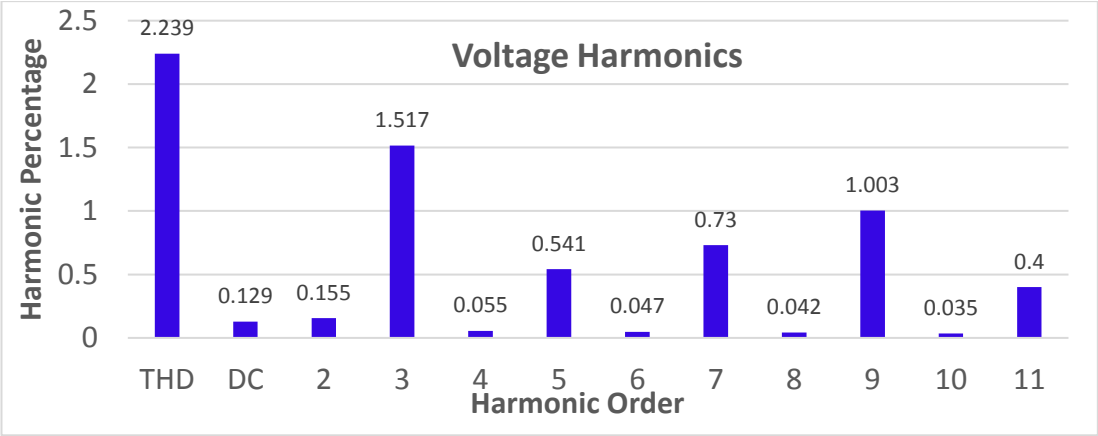

Figure 3.7: Voltage harmonic spectrum for "Inverter 1"

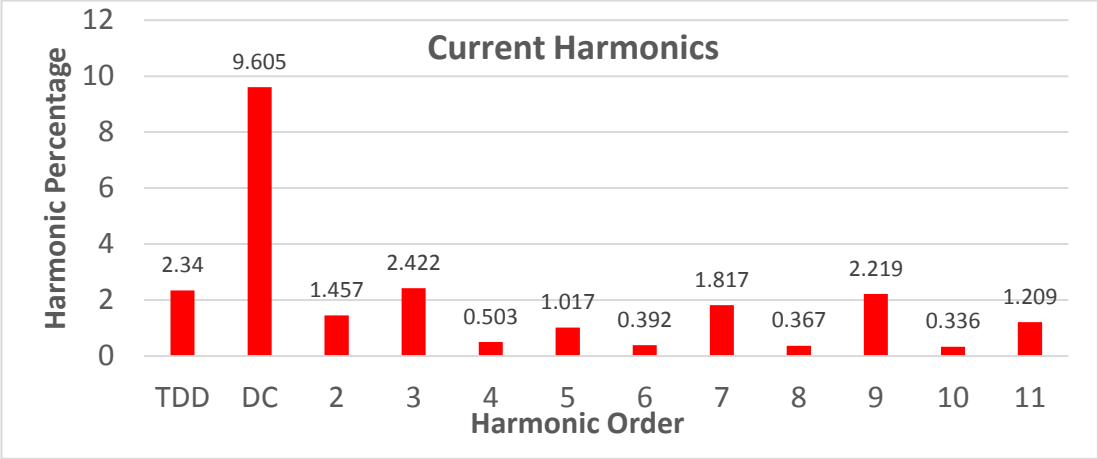

Figure 3.8: Current harmonics spectrum for "Inverter 1"

The harmonic spectrum for voltage and current are shown in Figure 3.7 and Figure 3.8 respectively, and the Figure 3.8 indicates a DC component of 9.6% which is above the 1% acceptable limit specified by the CEB grid code [26] . Furthermore, there is also a presence of a second harmonic above the specified odd harmonic limit. The 3rd, 7th and 9th harmonics are dominant in both voltage and current.

3.4.2 Inverter No 2

Similar to the previous inverter, this inverter was also operating at almost half of the total power output at the beginning of the measurement. The variations of power and voltage are shown in Figure 3.9 and Figure 3.10 respectively. The power output has gradually decreased from 1300 W to 1150 W over the one-hour period. A rapid

variation of 5 W in the output power can be observed in the plot. This is most likely due to the operation of the MPPT controller.

The variation of the grid voltage is independent from the power output unlike the previous inverter. Therefore, it can be concluded that the dips in output voltage were caused by external factors associated with the grid.

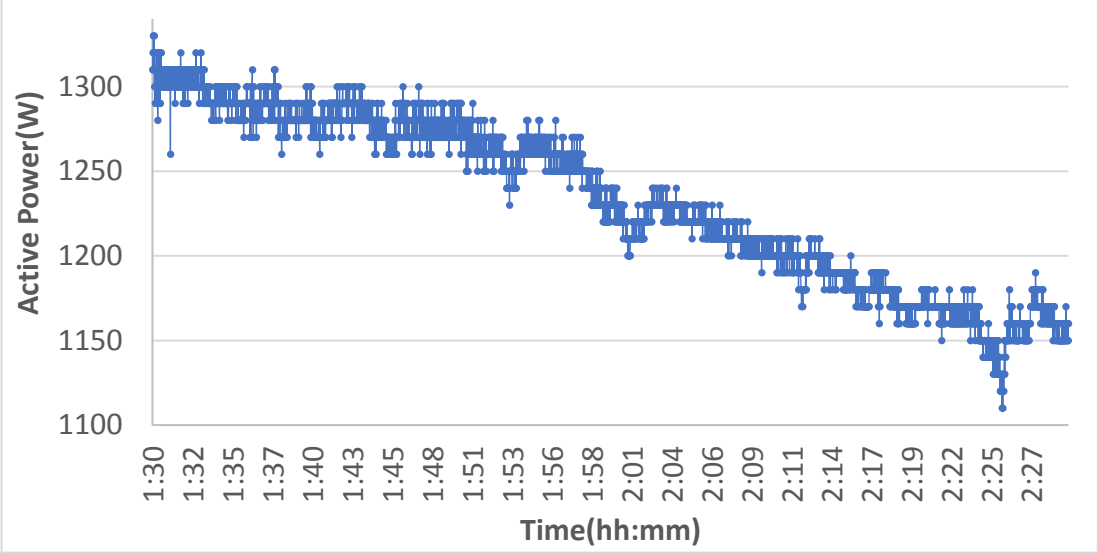

Figure 3.9: Measured active power output of "Inverter No. 2."

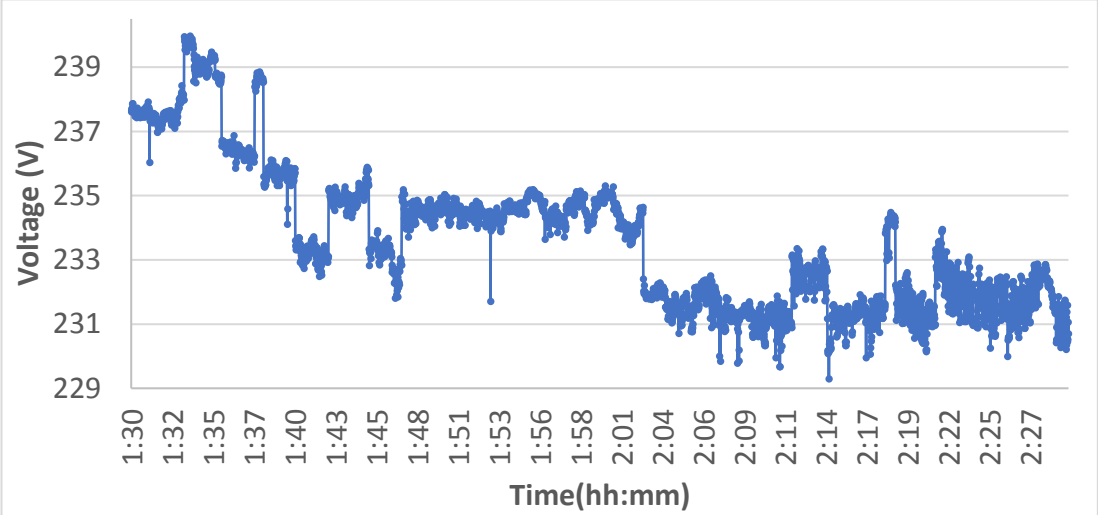

Figure 3.10: Inverter terminal voltage of "Inverter No. 2."

The TDD and THD variations of inverter No 2 are shown in Figure 3.11 and Figure 3.12 respectively. The voltage THD of this inverter shows an acceptable variation between 1.5% and 1.8%, which is within the limits. In contrast, the measured

TDD of current shows a variation between 65% and 115% indicating that the harmonics present are above the acceptable limits of the standard.

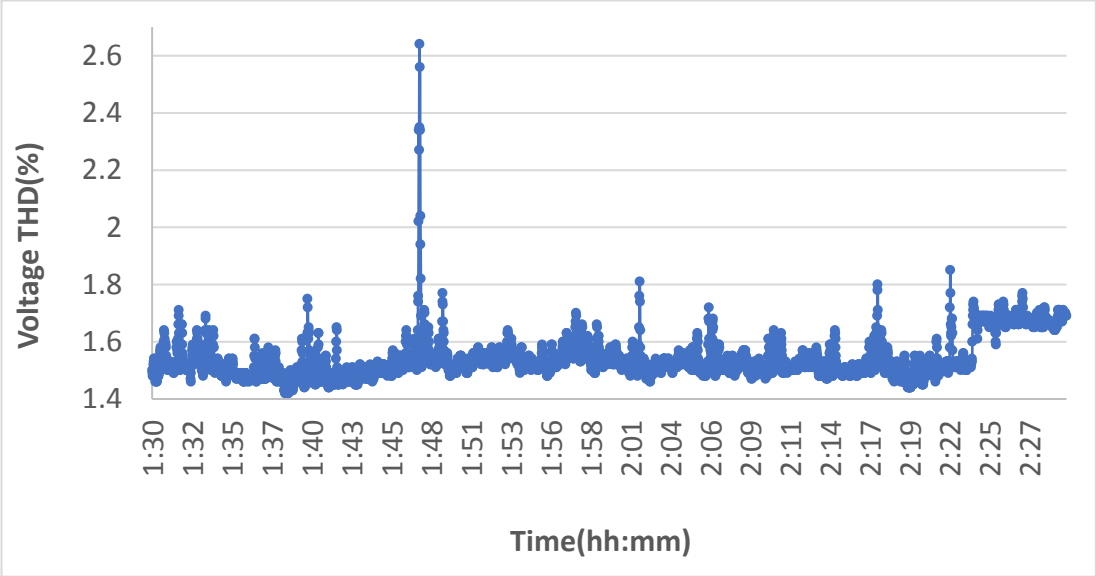

Figure 3.11: Voltage THD of "Inverter No. 2."

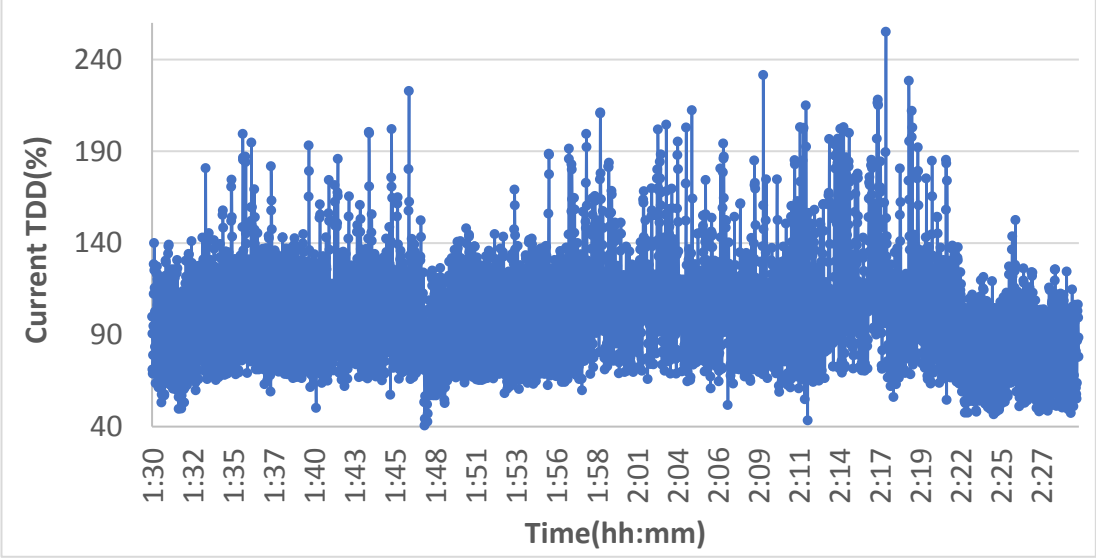

Figure 3.12: Current TDD of "Inverter No. 2

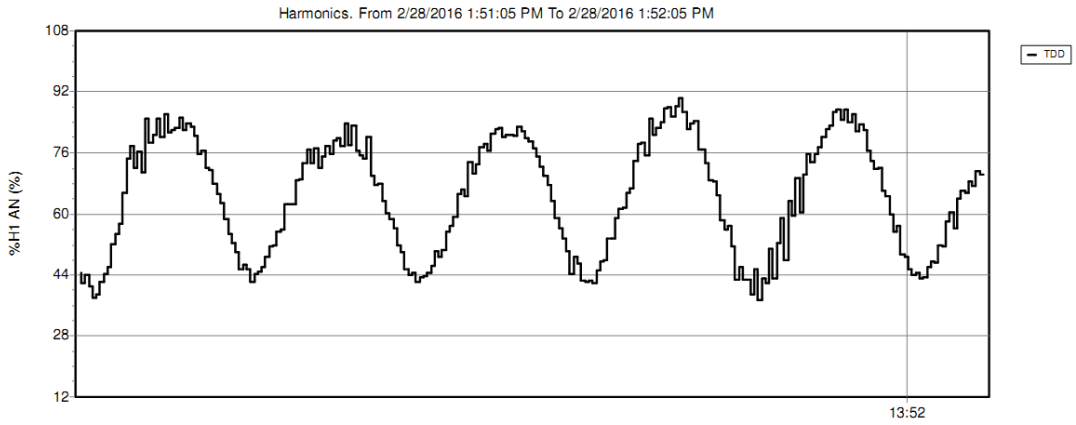

Figure 3.13: Oscillating TDD variation

Upon close inspection of the time evolution of the TDD, an oscillatory variation between 35% and 90% was observed with a frequency of 0.1 Hz. This can be a result of the dominant harmonics being superimposed on the large DC offset present in the current. It could also occur if the injected current is not in proper synchronism with the grid frequency. This variation is shown in Figure 3.13.

The voltage and current harmonic spectrums shown in Figure 3.14 and Figure 3.15 indicate a DC component of about 60% along with high percentages of odd and even harmonics. The presence of the DC component explains the odd harmonics in the current as it shifts the sine waveform and distorts its symmetry around the time axis.

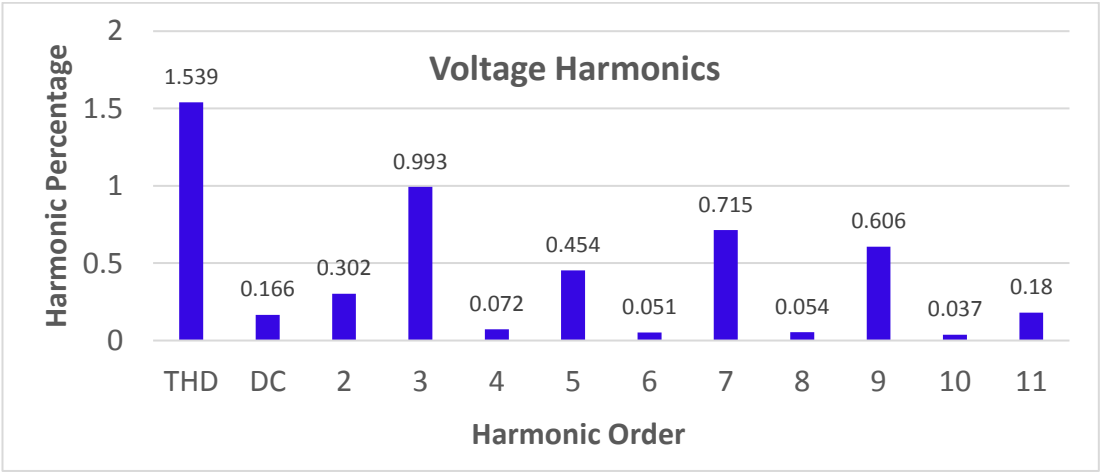

Figure 3.14: Voltage harmonic spectrum for “Inverter 2”

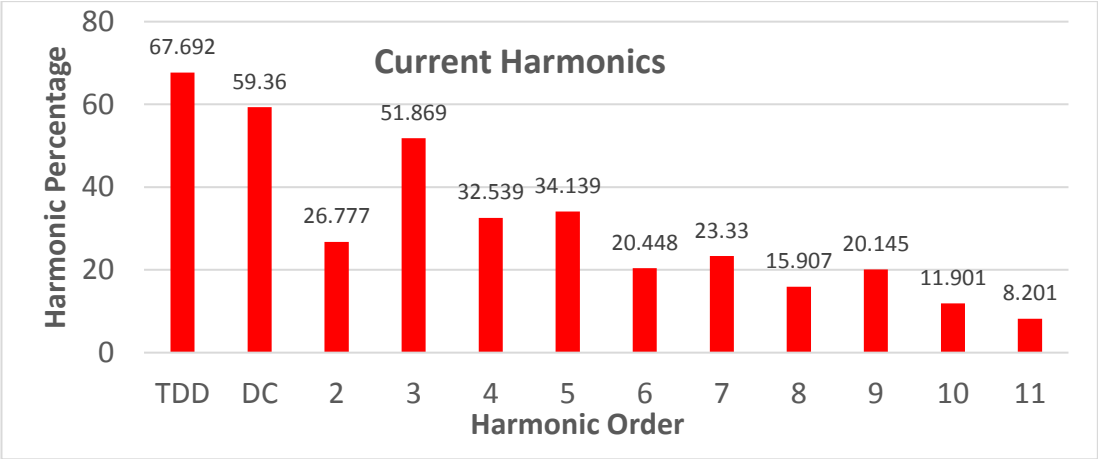

Figure 3.15: Current harmonic spectrum for "Inverter 2"

3.4.3 Inverter No 3

The third inverter used for the measurement was operating in a range of 150 W to 2160 W. This allowed to obtain a good measurement of the overall power output range of the inverter. The measurement plots for voltage and power are shown in Figure 3.16 and Figure 3.17 respectively.

The grid voltage variation throughout the whole period was about 10V, ranging from 236 to 226V. The irradiance variation did not cause any significant voltage sags or dips in the grid voltage.

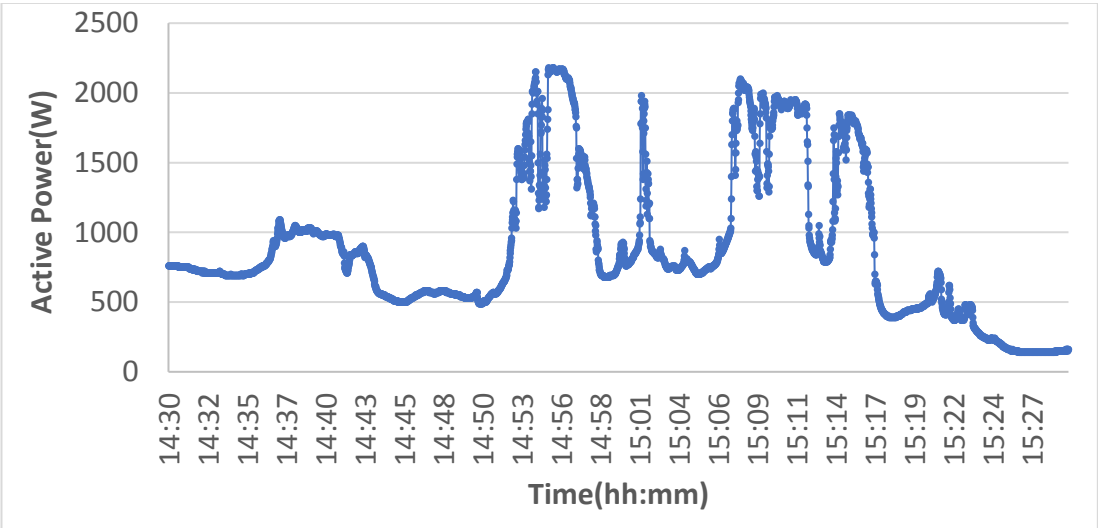

Figure 3.16: Measured active power output of "Inverter No. 3."

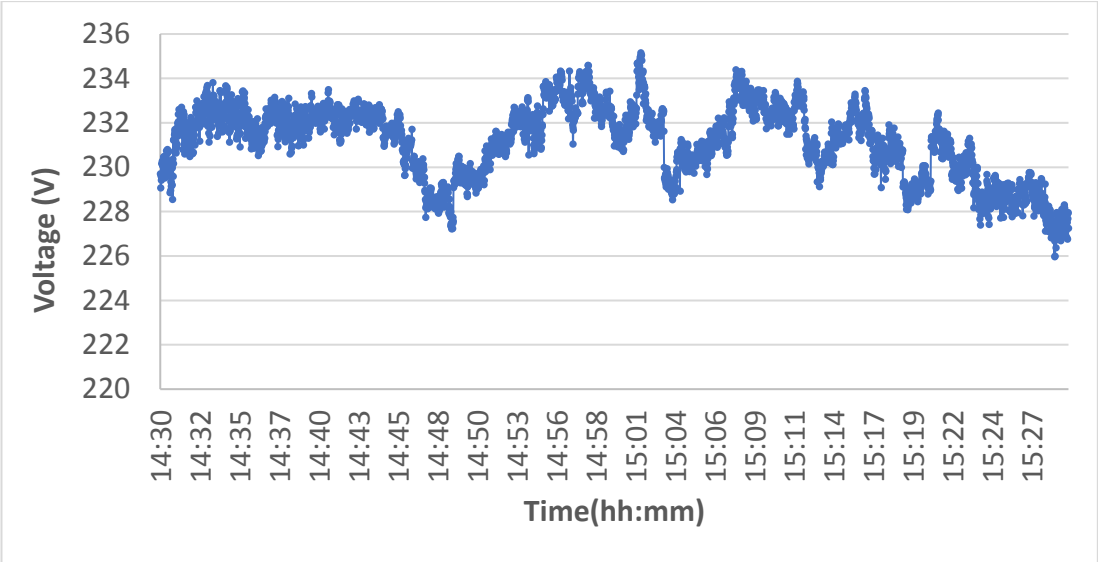

Figure 3.17: Inverter terminal voltage of "Inverter No. 3."

The THD and TDD variations are shown in Figure 3.18 and Figure 3.19. The THD of voltage has stayed around 2.5% while reaching a maximum of 2.68%. However, the TDD of current shows an average of 18.6% which violates the specified standard. An important observation can be noted when comparing the THD, TDD and power variations together. While the TDD of current has increased with the inverter power output, the THD of voltage has shown a slight reduction. It is clearly visible at the third power peak where the power has varied from 750 W to 2100 W at 1506 h, where the TDD has increased by 5% while the THD of voltage has dropped by 0.2%

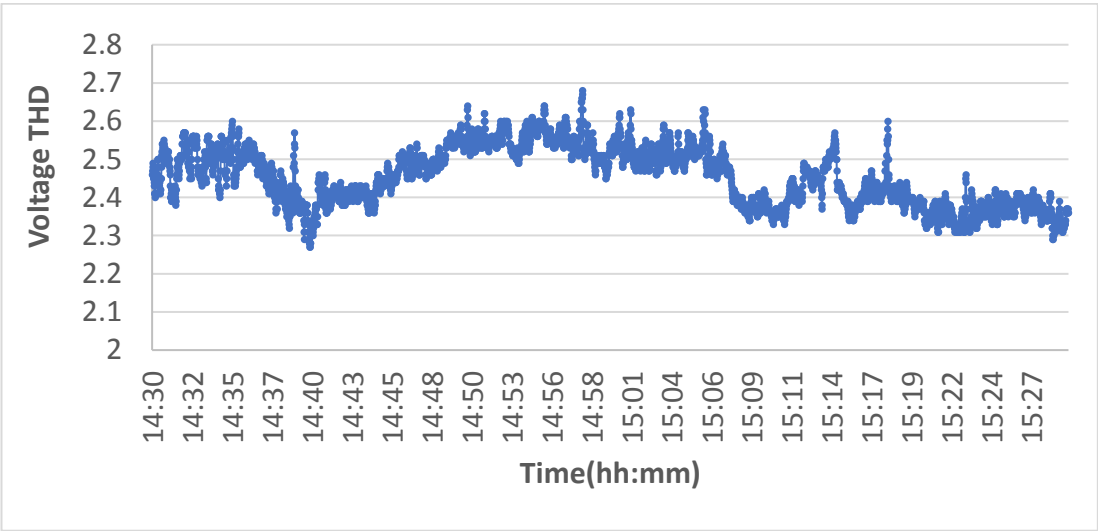

Figure 3.18: Voltage THD of "Inverter No. 2."

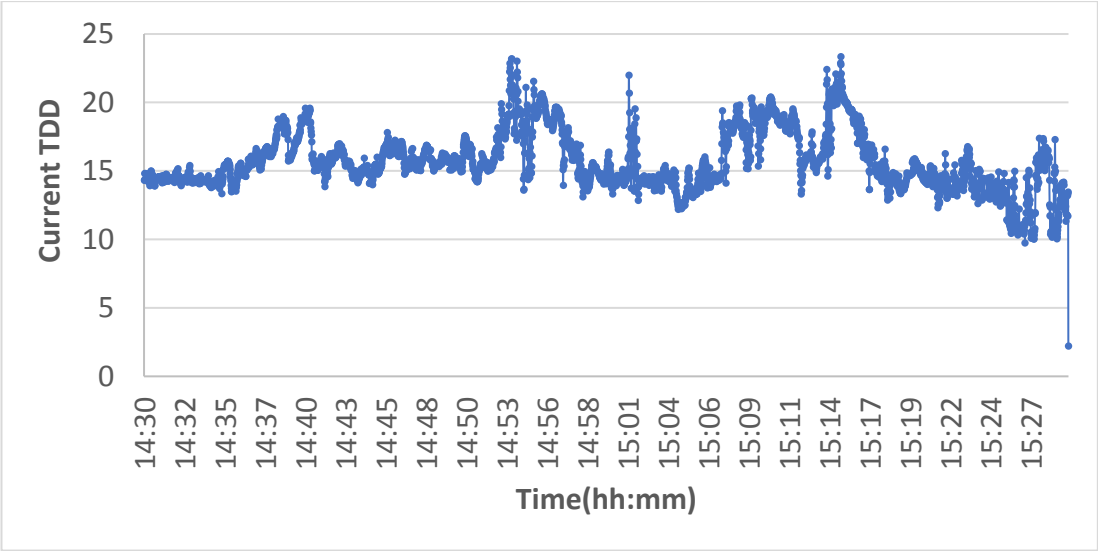

Figure 3.19: Current TDD of "Inverter No. 2."

The harmonic spectrums of the inverter are shown in Figure 3.20 and Figure 3.21. Similar to the previous inverter, the DC component of the current shows a magnitude of 60%. Significant odd harmonics are also present as a result of the DC offset. Harmonics of the 7th 9th and 11th order are more dominant in the spectrum. This could be due to the inverter topology or due to the resonance point of the output filter.

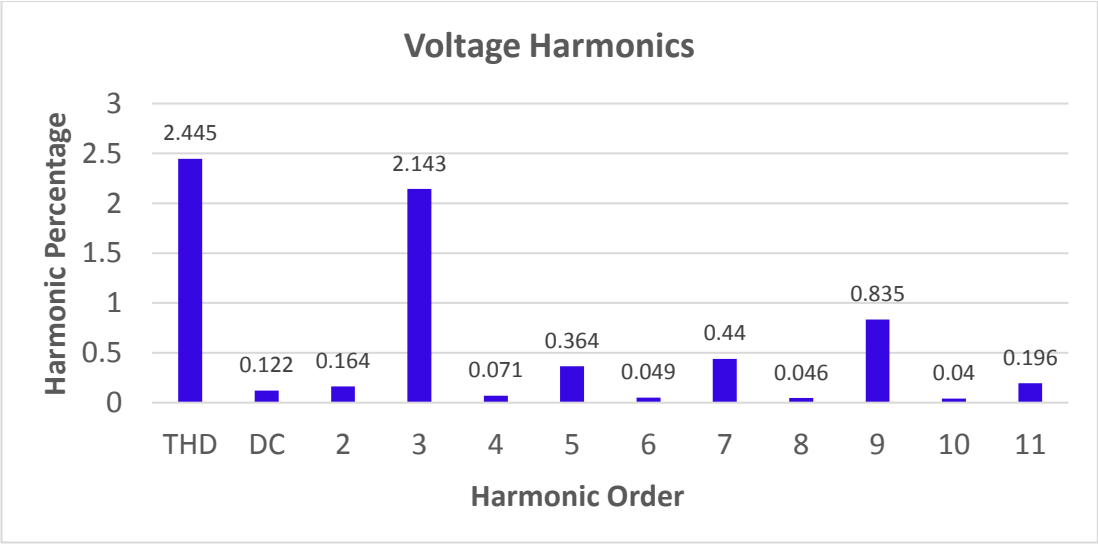

Figure 3.20: Voltage harmonic spectrum for "Inverter 3"

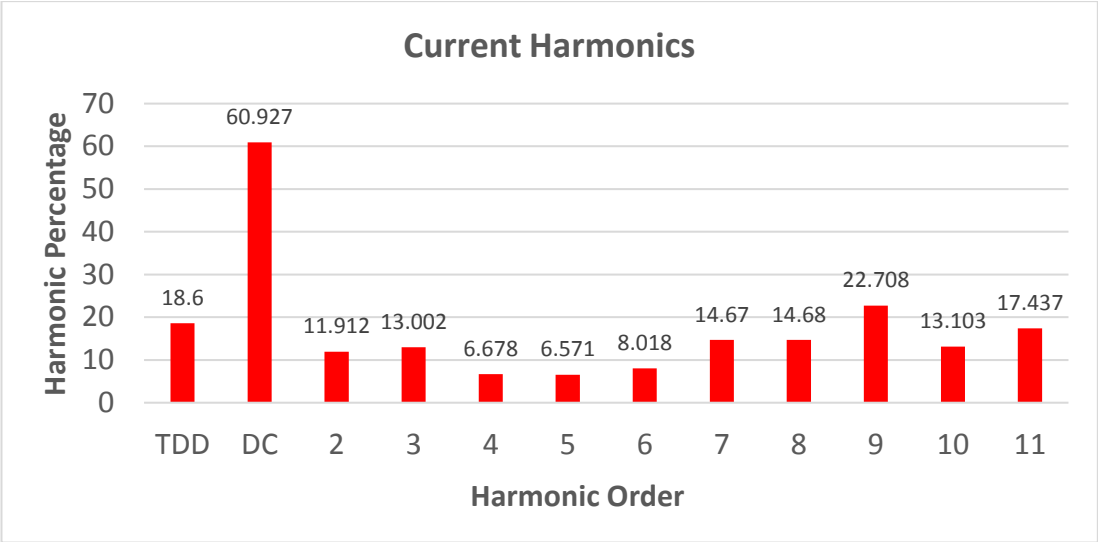

Figure 3.21: Current harmonic spectrum for "Inverter 3"

3.5 Summary

The summary of all three measurements are shown in Table 3.3. The individual harmonics are shown up to the 7th order. The values indicated are the average of each measurement throughout the measurement period.

Table 3.3: Summary of harmonic measurements

Inverter No			Voltage(V)	Current(A)	TDD	THD	Percentage of Fundamental						
							DC Component	2nd order	3rd order	4th order	5th order	6th order	7th order
1	**V-Phase to Neutral**	Avg	234			2.24	0.129	0.16	1.52	0.06	0.54	0.05	0.73
	Current-Phase to Neutral			3.74	4.426		**9.605**	**1.46**	2.42	0.5	1.02	0.39	1.817
2	**V-Phase to Neutral**		234			1.54	0.166	0.3	0.99	0.07	0.45	0.05	0.715
	Current-Phase to Neutral			5.33	**67.692**		**59.36**	**26.8**	**51.9**	**32.5**	**34.1**	**20.4**	**23.55**
3	**V-Phase to Neutral**		230			2.45	0.122	0.16	2.14	0.07	0.36	0.05	0.44
	Current-Phase to Neutral			2.78	**18.58**		**60.927**	**11.9**	**13**	**6.68**	**6.57**	**8.02**	**14.67**

According to the measurement summary, two of the inverters generate current harmonics that violate the IEEE standard [25] . All three are not complying with the standards specified for DC current injection. Two of them inject DC currents larger than half of its fundamental AC output. Out of the individual harmonics measured, the 3rd harmonic is the most dominant in both voltage and current.

The Net metering survey conducted by the research and development branch of CEB shows similar figures of TDD and THD for the measured inverters. Out of the 21 inverters measured, 14 inverters had exceeded the harmonic limits specified in the IEEE standard [25] .

However, the existing grid voltage harmonics and the variations in grid frequency can have an effect on the current harmonics generated by individual inverters based on their control algorithms. For a more accurate harmonic measurement, it is necessary to test each inverter in a laboratory environment.

The voltage variations recorded didn't show flicker levels that violate the specified standards [27] . As each inverter had a capacity of 2 kW, a variation in this capacity would not necessarily cause a significant voltage variation if the grid is sufficiently stiff. Therefore, a more detailed study should be conducted with higher capacity inverters to measure the flicker characteristics.

The presence of the DC component is harmful to the grid as they can shift the operating point of the distribution transformer and lead its core to saturation. It also contributes to the generation of odd harmonics which are present in two out of the three inverters. Similarly, the presence of the 3rd harmonic component in output current is well known to cause neutral conductor overheating in the LV grid.

As two out of the three measured transformerless inverters show a significant degradation of power quality due the presence of current harmonics, it is necessary to develop an inverter based on a topology that reduces the current harmonics generated. A Tri active bridge system that isolates household, PV system and the grid using a high frequency transformer provides a better harmonic spectrum compared to the transformerless system. Furthermore, it provides good isolation from faults and harmonics generated at household.

4 DESIGN OF THE TRANSFORMERLESS INVERTER AND PV SYSTEM COMPONENTS

A typical solar PV system usually consists of a PV array to generate power and a grid tied inverter to convert the generated power to 50Hz AC. The PV array has to be designed to supply the required capacity under varying environmental conditions. The inverter has to be equipped with a controller to maintain synchronism with the grid while exporting energy. It also requires a control algorithm to be in place to extract the maximum power from the PV panels. This control algorithm is responsible for maintaining the output voltage of the PV panel at a specified value. In addition to this, output filters at the grid tie inverter terminals and DC link capacitors at the DC bus have to be designed to filter out the higher order harmonics that are generated due to inverter switching.

In order to compare the improvements of the SST based systems, it is necessary to initially model the existing transformerless inverter. This chapter describes the design of the transformerless inverter and the PV system components.

4.1 PV Panel Selection

Rooftop solar PV arrays consist of individual panel modules that are connected in either series or parallel manner to satisfy the output voltage and power requirement. Each module consists of individual solar cells which are connected in series.

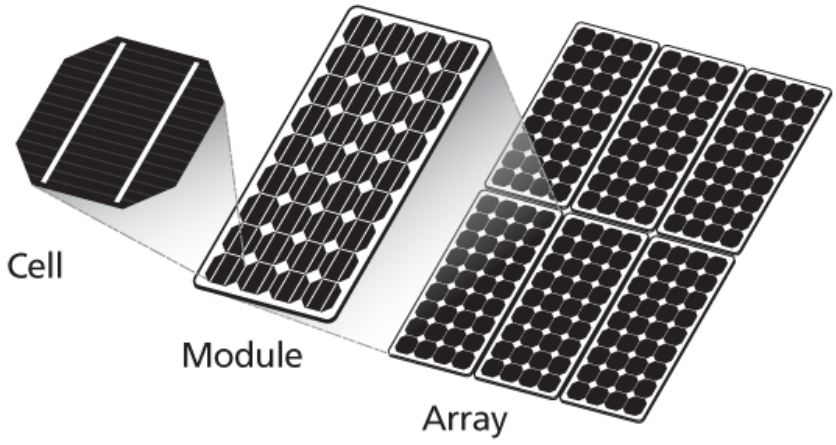

Figure 4.1: Solar PV cell arrangement

Each of these cells generate a voltage of approximately 0.5 V which adds up to an open circuit voltage of the module ranging from 25 V to 50 V based on the construction and the number of cells used. Commercial solar modules usually consist of 60 or 72 series connected cell arrangements. A typical arrangement is shown in Figure 4.1

In order to select a PV panel for this inverter, it was necessary to find the operating limits in terms of voltage and power. MATLAB Simulink has a PV panel model which includes a library of commercially available solar PV panels. It includes the nameplate data and P-V characteristics with respect to irradiance and temperature variations. For this design, it is required to have a PV array that generates a voltage above 325V throughout the whole operating range. This eliminates the requirement of a boost converter as the DC bus voltage can be maintained above the peak value of the grid voltage.

A 3 kW PV array was chosen as it is an optimal capacity for most of the Sri Lankan household customers. The solar module, Yingli Solar YL260p-35b was selected for this design as it is available for purchase in Sri Lanka. Twelve series connected modules were used to obtain a voltage above 325 V. The datasheet of the PV panel is provided in Appendix A. The P-V characteristics are shown in Figure 4.2.

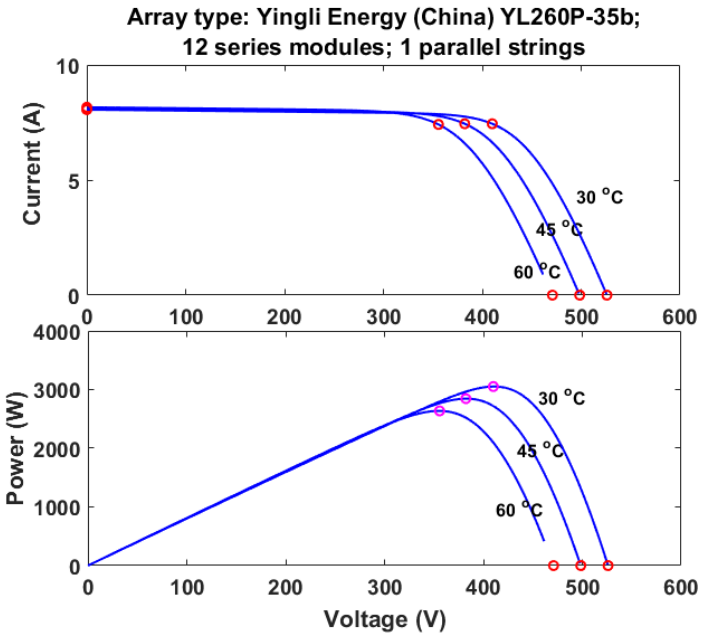

Figure 4.2: MPPT Characteristics

The output maximum power point (MPP) voltage of a PV panel changes with its operating temperature. As per the characteristic, with the increasing temperature the MPP voltage decreases. Therefore, it is necessary to find the upper limit of the operating temperature of a PV panel for Sri Lanka. Figure 4.3 shows the operating temperature and power variation of a 2000 W PV Canadian solar CS6K265P PV array during a sunny day in the month of July. As per the characteristic, on a sunny day even at its maximum power generation, the maximum temperature stays below 60ºC.

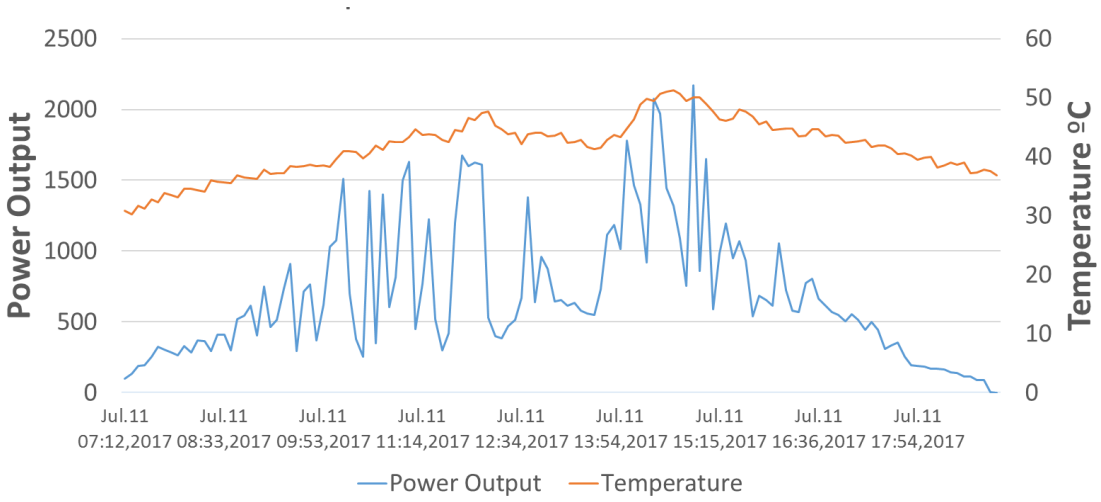

Figure 4.3: Temperature and power variation of a CS6K265P PV array

Therefore, the maximum operating temperature that a PV panel reaches was taken as 60 ºC. According to Figure 4.2, it can be seen that even at 60 ºC, the MPP array voltage does not reach 325 V.

As the lowest operation voltage of the PV array cannot be found in standard datasheets, it was determined by simulating the system with an irradiance of 50 W/m^2 and temperature of 60 ºC. The results in Figure 4.4 show that the MPP algorithm maintained a panel output voltage of 330 V. Therefore, it can be concluded that the output voltage of this panel stays above 325 V during the selected operating conditions.

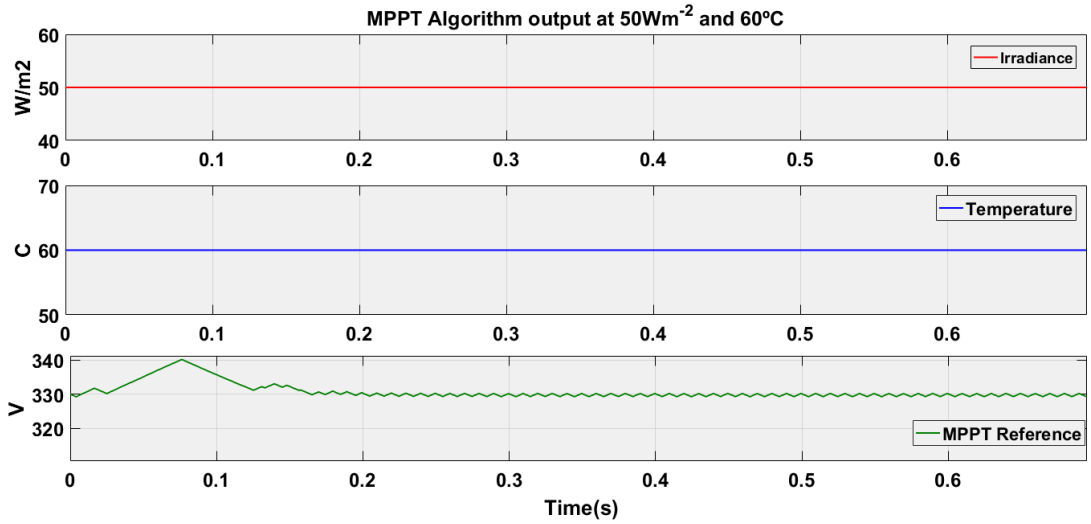

Figure 4.4: Minimum PV array voltage generated by MPPT algorithm

As the minimum operating voltage has been determined, it was necessary to find the maximum voltage the PV array would reach during the MPPT operation. As the MPP voltage increases with decreasing temperature the minimum temperature that a PV panel operates was taken as 25 ºC. A study conducted on the wind and solar assessment on Sri Lanka has shown that the maximum irradiance can reach up to 1000 Wm^{-2} [28]. A plot for MPP voltage with varying irradiance conditions is shown in Figure 4.5. The maximum irradiance was taken as 1,000 Wm^{-2}.

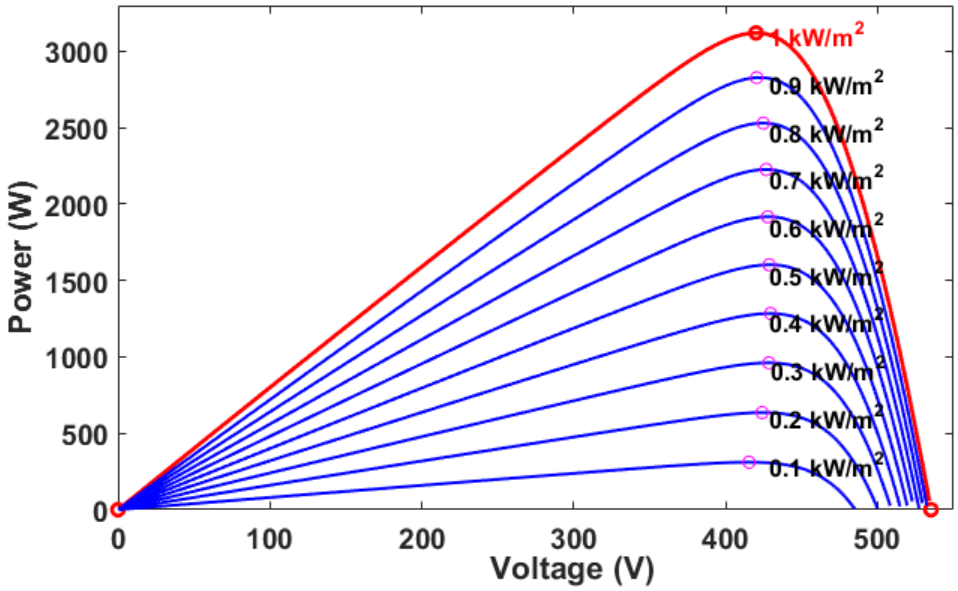

Figure 4.5: MPP voltage variation of PV array with irradiance

According to Figure 4.5 the MPP voltage reaches a maximum value of 430V at an irradiance of 400Wm^{-2}. A value of 450V was taken as the upper limit of voltage to facilitate the instantaneous variations.

Hence the operating limits of this PV array voltage were taken as 330V to 450V for designing the other components.

4.2 MPPT Algorithm Selection.

Among many algorithms discussed in the literature review, only the incremental conductance and perturb and observe algorithms were implemented in this study. Both of the algorithms were simulated and compared to determine which would give the best performance.

4.2.1 Perturb and observe algorithm

The perturb and observe algorithm is the simplest and most commonly used MPPT algorithm. The operational flow chart of the algorithm is shown in Figure 4.6

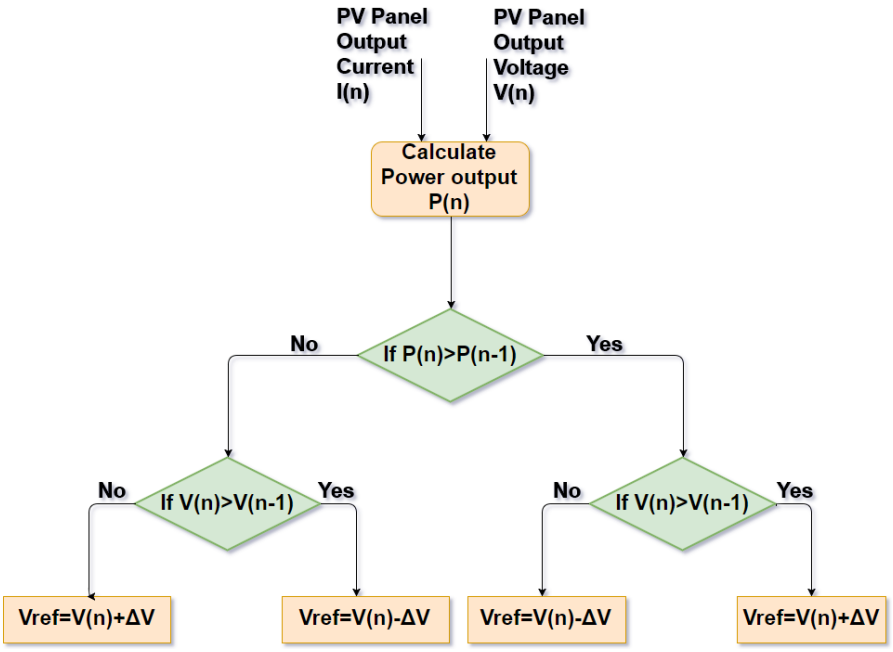

Figure 4.6: Perturb and observe algorithm

The Simulink model of Perturb and observe (P&O) MPPT algorithm was developed using the standard blocks available in Simulink. The voltage and current output was measured directly from the PV panel and multiplied to obtain the power output. The (n-1) condition was achieved using the unit delay block. For the initialization, the initial voltage value of 387.5V was used as it is the midpoint of the nominal operating range. Saturation limiter was used to limit the output of the algorithm in order to prevent erroneous values being fed to controllers at abnormal operating conditions such as DC faults. The developed Simulink model is shown in Figure 4.7.

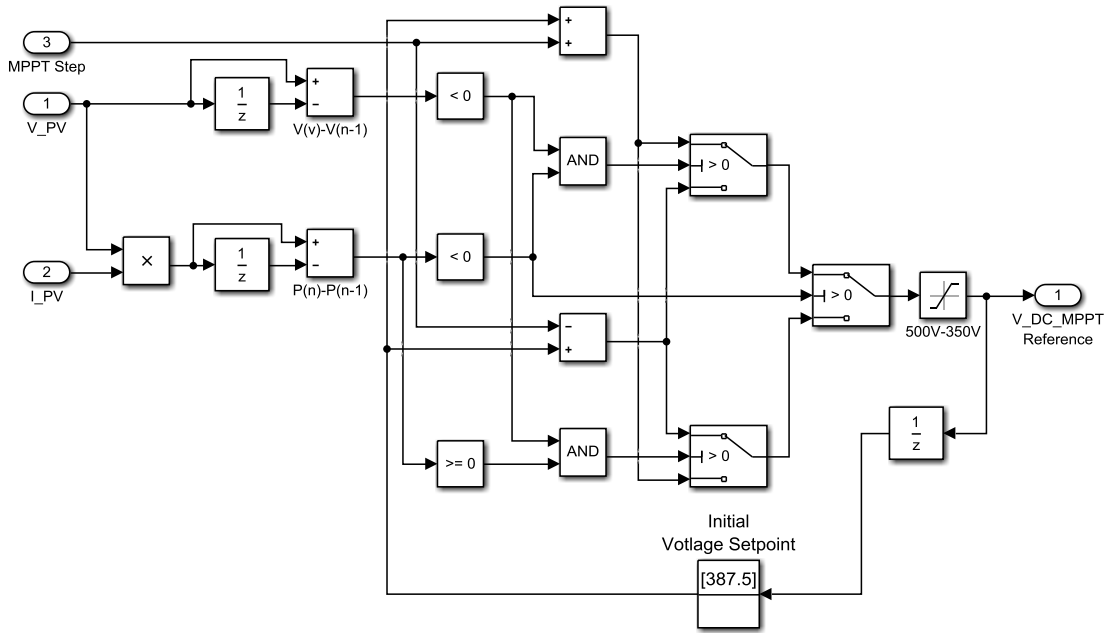

Figure 4.7: Simulink model of perturb and observe algorithm

4.2.2 Incremental conductance algorithm

The incremental conductance algorithm is relatively complex compared the P&O algorithm as it includes derivative terms to measure the rate of change of conductance. However, it is known to provide better performance at rapidly varying irradiance conditions. The flowchart of the algorithm is shown in Figure 4.8.

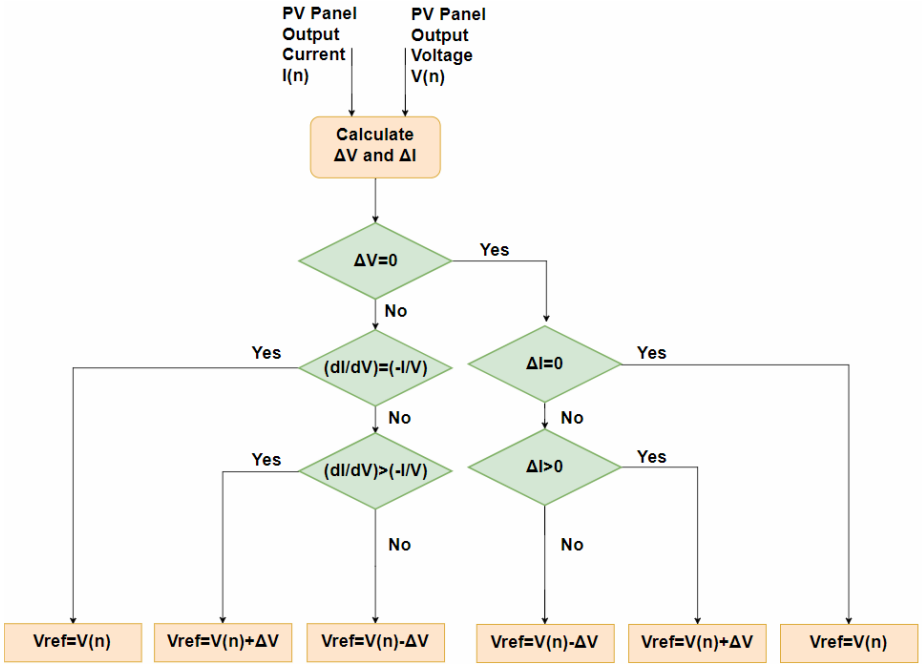

Figure 4.8: Incremental conductance MPPT algorithm

Similar to the P&O algorithm the incremental conductance algorithm was also developed using MATLAB Simulink. The developed system is shown in Figure 4.9.

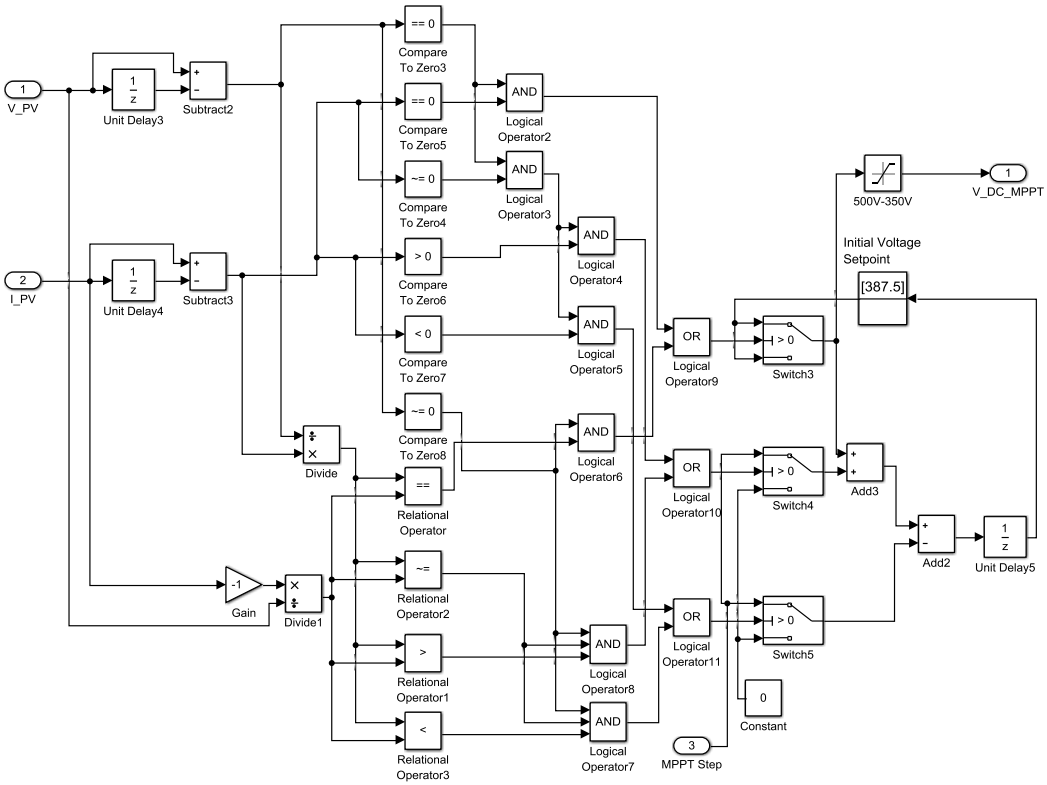

Figure 4.9: Simulink model of incremental conductance algorithm

The MPPT voltage step (MPPT Step) of both these algorithms were set as 0.1mV which is equal to (***Ts***/0.005), where ***Ts*** is the time step of the simulation.

4.2.3 Comparison of P&O and Incremental conductance algorithms

Both of the aforementioned algorithms were compared with varying temperature and irradiance conditions to determine the best algorithm for this design. Both of the algorithms were simulated for a 3 s period. The outputs of both algorithms are shown in Figure 4.10.

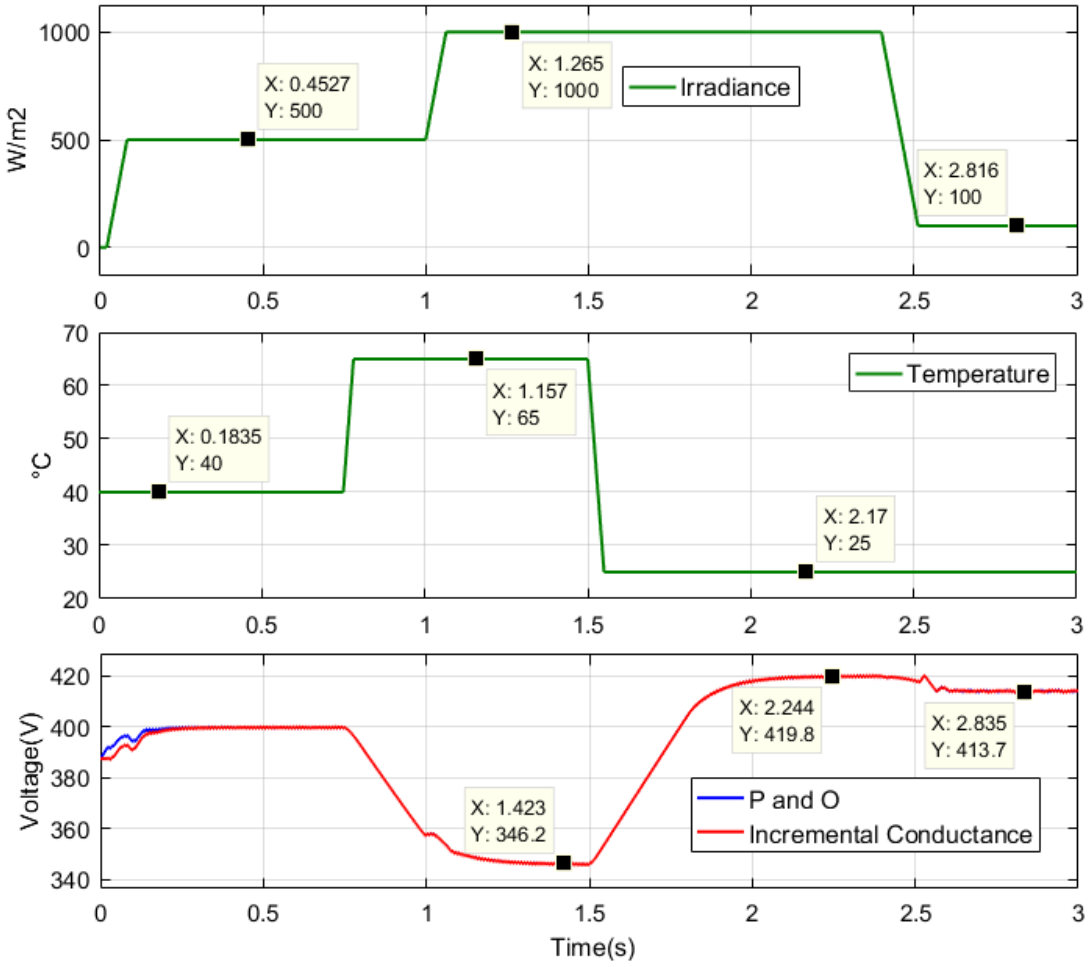

Figure 4.10: Comparison of the two MPPT algorithms

The plots indicate that using both of the MPPT algorithms, the output voltage reaches the desired MPP set point given in the nameplate characteristic. Upon a rapid change in temperature from 65 ºC to 25 ºC, the voltage reaches the desired set point in less

than 1 s. This is an acceptable figure as such rapid variations in temperature may not occur in reality. The other important observation is that the difference between the two algorithms are minimal except for a slight variation at the beginning. As the variation is minimal, it was decided to use the P&O algorithm as it is low in complexity.

4.3 Output Inverter

The output inverter used in this design is a full bridge inverter that consists of two pairs of IGBTs that operate in a complementary manner. The switching pulses for the inverter are generated using the unipolar sinusoidal PWM technique. Unipolar PWM is utilized as it results in better output power quality compared to the bipolar PWM technique [29]. The switching pulses generated by the sinusoidal PWM technique are generated by comparing two 180-degree phase shifted sinusoidal reference waveforms with a triangular carrier of 20 kHz. The reference waveform is generated using a single phase dq transform technique. The developed Simulink model of the output inverter is shown in Figure 4.11 with the output filter.

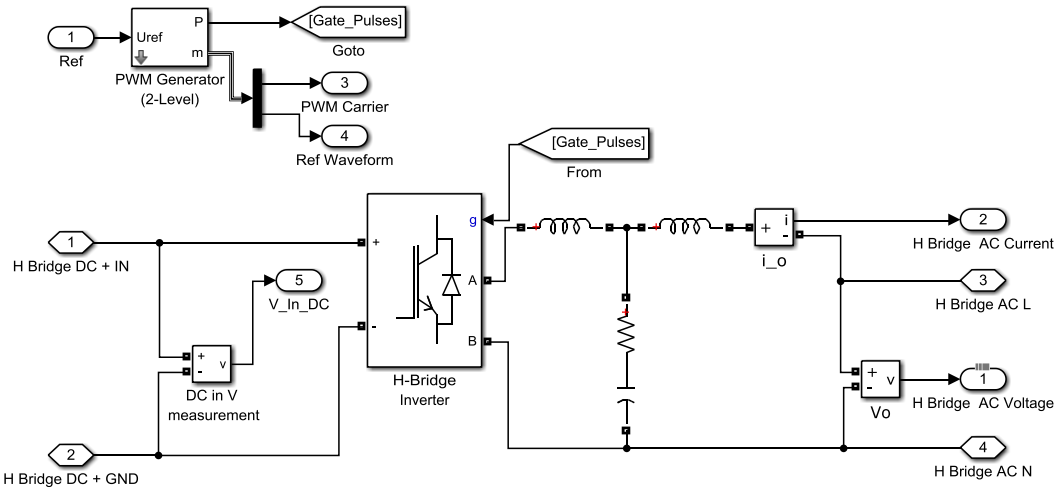

Figure 4.11: Grid tie inverter with output filter and PWM generator

4.3.1 Single phase dq transform

The dq transform is a transformation technique commonly used in three phase systems. Since controlling an oscillating three phase quantity is difficult, the dq

transformation is used to convert the time dependent oscillating components into time independent non-oscillating quantities. This is done by first converting the three phases to the αβ0 rotating reference frame using the Clarke transformation matrix given in equation (4.3.1).

$$\begin{bmatrix} I_\alpha \\ I_\beta \\ I_0 \end{bmatrix} = \begin{bmatrix} \frac{2}{3} & -\frac{1}{3} & -\frac{1}{3} \\ 0 & \frac{1}{\sqrt{3}} & -\frac{1}{\sqrt{3}} \\ \frac{1}{3} & \frac{1}{3} & \frac{1}{3} \end{bmatrix} \begin{bmatrix} I_a \\ I_b \\ I_c \end{bmatrix} \qquad (4.3.1)$$

Given

$$I_a = I\sin(\omega t)\ ,\ I_b = I\sin\left(\omega t - \frac{2\pi}{3}\right)\ and\ \ I_b = I\sin\left(\omega t + \frac{2\pi}{3}\right)$$

I_α, I_β quantities are the two rotating vectors which are 90º shifted in phase.

The I_α, I_β and I_0 parameters are converted to the dq0 reference frame by multiplying with the park transformation matrix shown in equation (4.3.2).

$$\begin{bmatrix} I_d \\ I_q \\ I_0 \end{bmatrix} = \begin{bmatrix} \sin(\omega t) & -\cos(\omega t) & 0 \\ \cos(\omega t) & \sin(\omega t) & 0 \\ 0 & 0 & 0 \end{bmatrix} \begin{bmatrix} I_\alpha \\ I_\beta \\ I_0 \end{bmatrix} \qquad (4.3.2)$$

This converts the three phase rotating quantities into two non-oscillating quantities given as $\boldsymbol{I_d}$ and $\boldsymbol{I_q}$ which are independent from the rotating time dependent $\boldsymbol{\omega t}$ terms of the three-phase system. This is important for controller design as simple PI controllers can be used to manipulate these $\boldsymbol{I_d}$ and $\boldsymbol{I_q}$ quantities to control the output of the inverter. Figure 4.12 describes the three reference frames accurately.

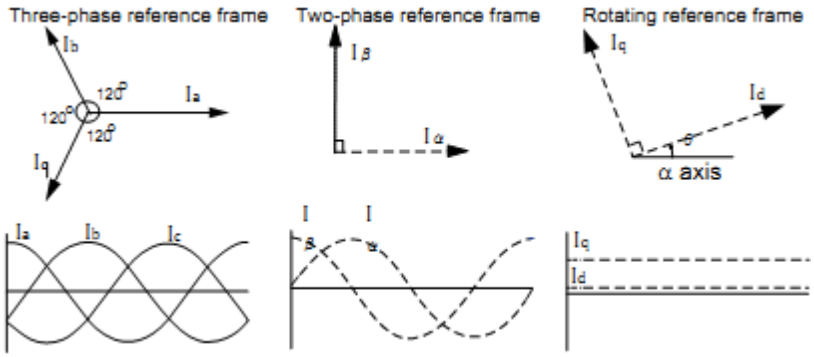

Figure 4.12: dq transform representation

However, in the single-phase system, there is only one oscillating vector. This is taken as $\boldsymbol{I_\alpha}$, and the other orthogonal vector is generated by delaying the phase of this vector by π/2 [30] [31] . This phase delay is achieved by delaying the waveform by (¼$\boldsymbol{T_s}$) seconds, where $\boldsymbol{T_s}$ is the cycle time of the waveform. This delaying generates the $\boldsymbol{I_\beta}$ component, which is 90º behind the measured waveform. The park transformation matrix can now be used to generate the required $\boldsymbol{I_d}$ and $\boldsymbol{I_q}$ quantities similar to the three-phase system.

This method is used to generate the PWM reference waveform of the grid side inverter of this design. The output current of the inverter is measured and filtered for any higher order harmonics and is delayed by 0.05s(1/4$\mathbf{T_s}$) to generate a 90º phase shifted $\boldsymbol{I_\beta}$ while using the measured current as $\boldsymbol{I_\alpha}$.

The two quantities $\boldsymbol{I_\alpha}$ and $\boldsymbol{I_\beta}$ are given by equations (4.3.3) and (4.3.4).

$$I_\alpha = I\sin(\omega t + \phi) \qquad (4.3.3)$$

$$I_\beta = I\sin\left\{(\omega t + \phi) - \frac{\pi}{2}\right\} = -I\cos(\omega t + \phi) \qquad (4.3.4)$$

where

ϕ = angle between the measured output current and voltage

I = peak value of the measured inverter output current

multiplying this with the park transformation matrix gives the $\boldsymbol{I_d}$ and $\boldsymbol{I_q}$ quantities by equations (4.3.5) and (4.3.6)

$$\begin{bmatrix} I_d \\ I_q \\ I_0 \end{bmatrix} = \begin{bmatrix} \sin(\omega t) & -\cos(\omega t) & 0 \\ \cos(\omega t) & \sin(\omega t) & 0 \\ 0 & 0 & 0 \end{bmatrix} \begin{bmatrix} I\sin(\omega t+\phi) \\ -I\cos(\omega t+\phi) \\ I_0 \end{bmatrix}$$

$$\begin{aligned} I_d &= I\left\{\sin(\omega t)\sin(\omega t+\phi)+\cos(\omega t)\cos(\omega t+\phi)\right\} \\ &= I\cos(\phi) \end{aligned} \quad (4.3.5)$$

$$\begin{aligned} I_q &= I\left\{\cos(\omega t)\sin(\omega t+\phi)-\sin(\omega)\cos(\omega t+\phi)\right\} \\ &= -I\sin(\phi) \end{aligned} \quad (4.3.6)$$

The derived $\boldsymbol{I_d}$ and $\boldsymbol{I_q}$ quantities are the active and reactive currents of the inverter output[32][33]. In order to control the active power output of the inverter, the $\boldsymbol{I_d}$ parameter has to be controlled. An $\boldsymbol{I_{d,ref}}$ reference was generated using a separate reference generation system that involves the output of the MPPT algorithm and the DC bus voltage. The $\boldsymbol{I_d}$ component of this measured inverter output current was compared with this $\boldsymbol{I_{d,ref}}$ and given as an input to a PI controller. The PI controller generates an output $\boldsymbol{V_d}$ reference which is transformed into a sinusoidal quantity using the inverse park transformation matrix. Similar to the $\boldsymbol{I_d}$ current, $\boldsymbol{I_q}$ was also given as an input to a PI controller. In this case the $\boldsymbol{I_{q,ref}}$ was maintained at zero as only active power was controlled. The output $\boldsymbol{V_q}$ is also transformed to a sinusoidal quantity. However only the sinusoidal reference $\boldsymbol{V_d}$ was given to the PWM generation circuit and $\boldsymbol{V_q}$ was ignored as it is basically the time delayed version of $\boldsymbol{V_d}$**.** The block diagram of the designed system is shown in Figure 4.13.

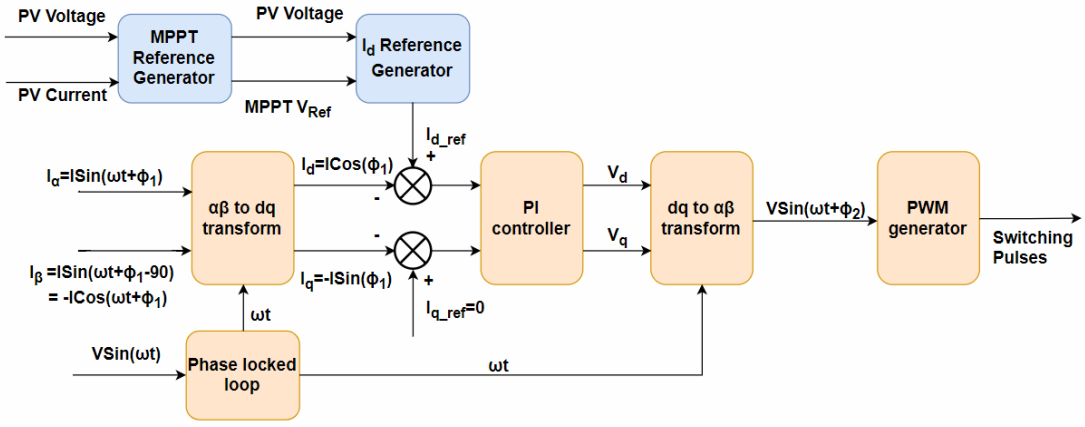

Figure 4.13: Power flow control using dq transform

In addition to this, the voltage reference waveform has to maintain synchronism with the grid voltage. This was achieved using a phase locked loop (PLL). The PLL consists of a phase comparator, low pass filter and a voltage controlled oscillator. The phase comparator compares the phase difference between the input and output waveforms and sends the error to the voltage controlled oscillator through a low pass filter to filter out the higher order frequencies. This voltage controlled oscillator generates an output waveform that matches the phase and frequency of the measured reference. The output of this oscillator was used for the dq transformation that is used to generate the output reference waveform of the inverter. The dq control circuit developed in Simulink is shown in Figure 4.14

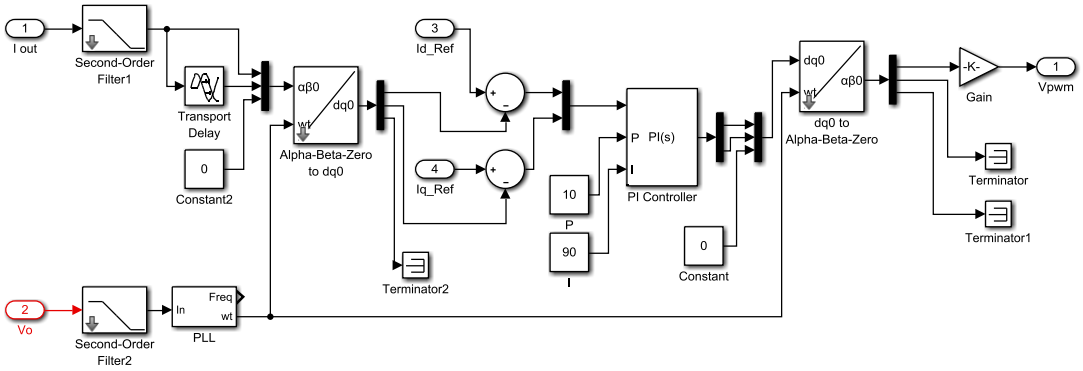

Figure 4.14: Single phase dq controller for active power flow control

4.3.2 I_d reference generation

The I_{d_ref} reference for the dq transformation circuit is required to control the inverter power output. This reference can be generated by comparing the PV panel mean output voltage with the reference generated by the MPPT algorithm. The mean output voltage was taken in order to eliminate the 100 Hz ripple generated by the switching of the full bridge inverter. Instead of obtaining the mean, a band stop filter can also be used to eliminate this ripple. The error between the DC bus voltage and the MPPT reference was given to a PI controller to generate the relevant I_d reference for the output inverter. The Simulink model of the reference generation circuit is shown in Figure 4.15. The ***Vin_DC_Mean*** is the mean voltage measurement of the

output DC bus and the ***V_DC_MPPT*** is the reference generated using the MPPT algorithm.

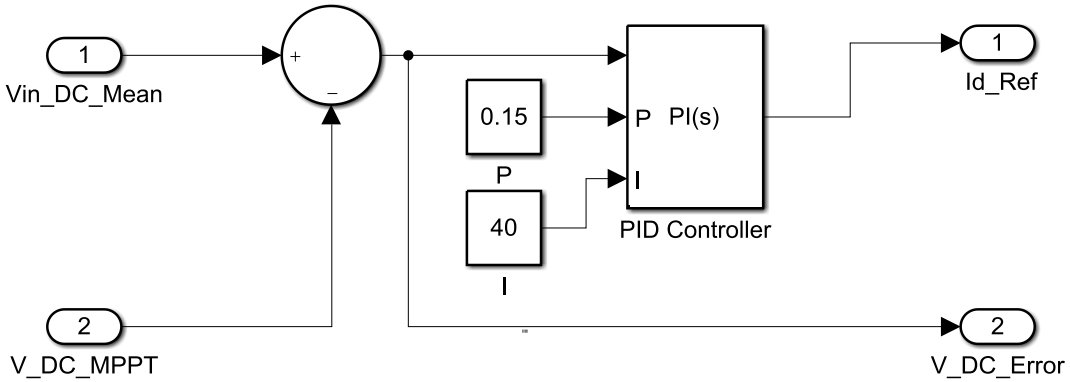

Figure 4.15: I_d reference generation for dq controller

4.4 LV Grid

In order to simulate the designed system accurately, it has to be connected to a LV grid that resemble the actual conditions. A LV grid has to be modeled taking all the applicable parameters into account. The fault level of the 33 kV grid at the Sri Jayewardenepura area was taken to model the medium voltage grid. Parameters of a 160 kVA distribution transformer were obtained from a nameplate and a test report. Resistance and inductance parameters of the LV line were included with the transformer loaded up to 50% of its capacity.

4.4.1 33kV MV grid model

The 33 kV MV grid was represented by a three-phase source in Simulink. The fault level of Sri Jayewardenepura area was taken as 13.1 kA with an angle of -87.9º from the transmission development plan of CEB [34].

Taking the base voltage as 33kV, the fault MVA can be calculated by equation (4.4.1).

$$fault\ kA = \frac{fault\ MVA}{\sqrt{3} \times Base\ Voltage(kV)} \qquad (4.4.1)$$

$$fault\ MVA = fault\ kA \times \sqrt{3} \times Base\ Voltage(kV)$$

$$\therefore\ fault\ MVA = 13.1 \times 33 \times \sqrt{3} = 748.76 MVA$$

Similarly, X/R can be calculated a by Equation 4.4.2

$$\left(\frac{X}{R}\right) = \tan(\phi) \qquad (4.4.2)$$

$$\left(\frac{X}{R}\right) = \tan(-89.7^{o}) = 27.27$$

4.4.2 Distribution transformer model

The details obtained from the nameplate and test sheets of the distribution transformer are shown in Table 4.1.

Table 4.1: Parameters obtained from nameplate and test reports

Impedance Voltage (I_z)	4.46%
Measured No load loss (P_{NL})	442 W
Measured no load current(I_{exc})	0.95%
Measured Load Loss(P_{sc})	2502 W

The leakage impedance of the transformer can be given by [35]

$$Z_{pu} = \frac{I_z\%}{100} = 0.0446\,pu$$

The load loss equivalent resistance of the transformer can be calculated as

$$R_{pu} = \frac{P_{SC}}{MVA_{SCtest} \times 1000} = \frac{2502 \times 10^{-3}}{0.16 \times 1000} = 0.0156\,pu$$

The leakage reactance of the transformer can be given as

$$X_{pu} = \sqrt{Z_{pu}^2 - R_{pu}^2} = \sqrt{0.0446^2 - 0.0156^2} = 0.0418\,pu$$

As the excitation current is, 0.95% the magnetizing branch admittance is given as

$$Y = \frac{\%I_{exc}}{100} = 0.0095\,pu$$

No load loss equivalent conductance is given by

$$G = \frac{P_{NL}}{MVA_{NLTest} \times 1000} = \frac{0.442}{0.160 \times 1000} = 0.00276\,pu$$

Hence the magnetizing branch resistance can be calculated as $\frac{1}{G} = 361\ pu$

The magnetizing susceptance can be given by

$$B = \sqrt{Y^2 - G^2}$$
$$= \sqrt{0.0095^2 - 0.00276^2}$$
$$= 0.00909\ pu$$

Therefore, the magnetizing reactance can be given as $\frac{1}{B} = 110\,pu$

These parameters were used to model the distribution transformer in Simulink

4.4.3 Distribution line conductor

All aluminum conductor (AAC) type was used as the distribution line conductor in the simulation. The length of the line was taken as 500 m. The per km resistance and reactance of an AAC conductor is 0.505 Ω/km^{-1} and 0.293 Ω/km^{-1} respectively.

Hence the parameters of the line for 500 m are

$$R = 0.2525\ \Omega$$
$$L = 0.466\ mH$$

The modeled LV grid for the simulation is shown in Figure 4.16. All three phases of the transformer were equally loaded with three 26 KVA loads operating at 0.85 power factor.

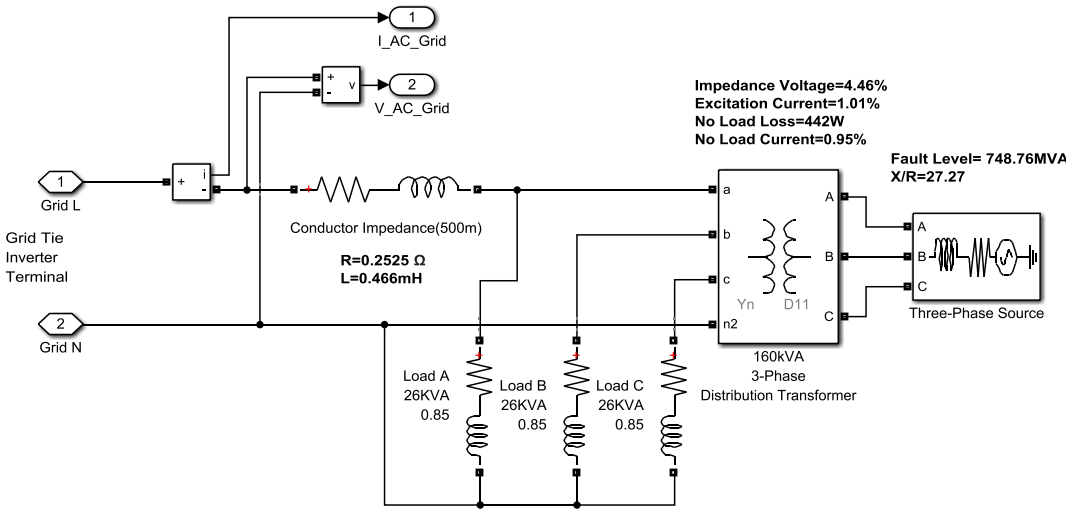

Figure 4.16: Simulink model of the LV grid

4.5 Inverter Output Filter

The output filter plays an important role in reducing the higher order harmonics generated by the PWM switching process. There are three types of passive filters that are commonly used.

The simplest is the first order filter where an inductor is used in series between the LV grid and inverter output terminal. As the impedance of the inductor gradually increases with increasing frequency, this filter provides 20 dB attenuation per decade for the increasing harmonic frequencies. However, eliminating a specific range of harmonics is difficult with this arrangement as it requires the inverter to operate in a higher switching frequency to sufficiently attenuate the harmonics generated around the switching frequency.

The second order filter usually consists of a capacitor connected in parallel between the series connected inductor and the LV grid. With the inductor and capacitor present, a resonance point is created which matches the $\frac{1}{\sqrt{LC}}$ condition. In this arrangement the attenuation stays at 20 dB until the resonance point. From the

resonance point onwards, the attenuation increases up to 60 dB per decade as the higher order harmonics are further filtered through the capacitor. As the reactance of a capacitor decreases with increasing frequency, it provides a shunt path preventing the higher order harmonics reaching the grid.

However, in reality when connecting the inverter to the grid, there are line inductances which would be added ahead of the LC filter. In this case the line inductances become dominant over determining the resonance point of the filter design. This is not a desirable condition as the varying line inductance becomes a parameter that determines the characteristics of the filter. To eliminate this problem, a third inductance is physically added between the capacitance and the grid connection making the design a third order LCL filter. This added inductance is designed to minimize and dominate the effects of the line inductances.

The LCL filter itself wouldn't be sufficient to eliminate all harmonics. As there is a resonance point in the filter configuration, the harmonics at this resonance point get amplified. These harmonics have to be damped in order to get the maximum benefit of the output filter. Multiple methods can be found in literature for damping [36]. The simplest method to achieve damping is using a resistor in series with the capacitive element. Although adding the resistor might cause the attenuation upon the resonance point to decrease, with a higher switching frequency the component values can be tuned to get the optimal harmonic spectrum. The filter configuration with distribution line parameters are shown in Figure 4.17.

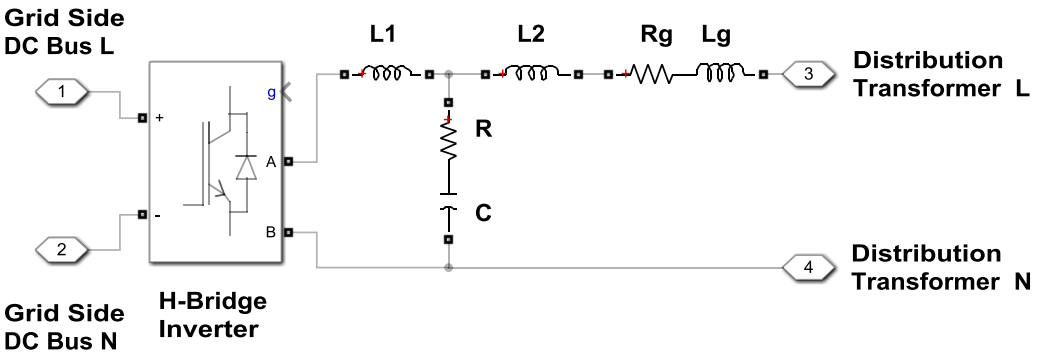

Figure 4.17: Grid tie inverter output filter components with LV line parameters

Considering the output voltage of the inverter as V_{dc} and the grid voltage as V_g the relationship between the output inductor L_1 and the current ripple ΔI_L can be given by equation (4.5.1)

$$V_{dc} - V_g = L\frac{\Delta I_L}{DT_s} \tag{4.5.1}$$

rearranging, the required inductance can be given by equation (4.5.2)

$$L = \frac{(V_{dc} - V_g)}{\Delta I_L}\left(\frac{D}{f_s}\right) \tag{4.5.2}$$

as the magnitude of the current ripple becomes maximum when the duty is 50%, the value of L_1 is calculated considering D=0.5 and V_g=0.5V_{dc}. With this the required inductance for the filter can be calculated by equation (4.5.3)

$$L = \frac{\left(V_{dc} - \frac{V_{dc}}{2}\right)\left(\frac{0.5}{f_s}\right)}{\Delta I_L} = \frac{V_{dc}}{4 f_s \Delta I_L} \tag{4.5.3}$$

As the inverter maximum power output is 3120 W, the maximum output current I_L was taken as 14 A. Allowing only 5% ripple in the inverter output current, the ripple can be calculated as

$$\Delta I_L = 0.05.I_L = 0.7A$$

Substituting ΔI_L to equation (4.5.3), the required inductance can be calculated as

$$L = \frac{350}{4 \times 40000 \times 0.7} = 3.125mH$$

Since the inverter works in unipolar switching mode the switching frequency is double the carrier frequency, f_s was taken as 40 kHz. The ripple of the inductor current is shown in Figure 4.18.

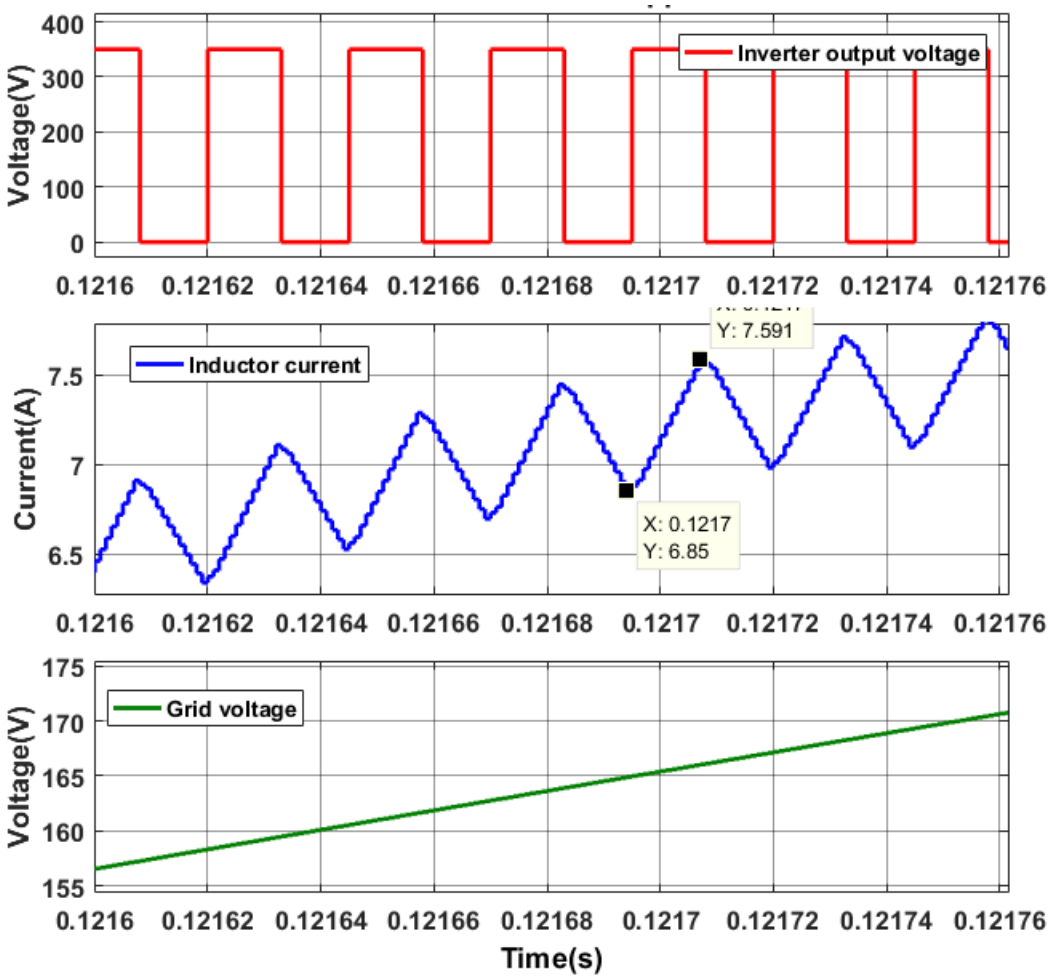

Figure 4.18: Inductor current ripple with grid voltage and inverter output voltage

The filter capacitance is calculated by multiplying the allowed power factor variation of the grid with the base capacitance of the system [37]. The CEB grid code specifies a power factor variation of 0.8 lagging and 0.9 leading for power generating units [26] . Therefore, a power factor variation of 0.1 was taken for this calculation.

The base impedance of the system is calculated by equation (4.5.4).

$$Z_{base} = \frac{V_{grid}^2}{P_n} \qquad (4.5.4)$$

$$= \frac{230^2}{3120} = 17\Omega$$

The base capacitance is calculated by equation (4.5.5)

$$C_{base} = \frac{1}{Z_{base}\omega} \qquad (4.5.5)$$

$$= \frac{1}{17 \times 2\pi \times 50} = 187.24\mu F$$

taking the maximum allowable power factor variation as 0.1, the filter capacitance can be calculated as equation (4.5.6)

$$C_f = 0.1 C_{base} \qquad (4.5.6)$$

$$= 0.1 \times 187.24 = 18.72\mu F$$

The grid side inductance $\boldsymbol{L_2}$ was obtained by plotting the transfer functions of the output filter. The filter functions for the output voltage and current can be derived as shown in equation (4.5.7) and (4.5.8). The resonance frequency can be calculated by 4.5.9. The $\boldsymbol{L_2}$ inductance was obtained by adjusting its value until the effect of the LV conductor inductor becomes negligible. In this case the same value of the $\boldsymbol{L_1}$ was taken for $\boldsymbol{L_2}$ as it provided a desirable result.

$$\frac{V_o}{V_I} = \frac{(sL_g + sL_2 + R_g)(1 + sR_cC)}{s^3L_1C(L_g + L_2) + s^2C(R_gL_1 + R_cL_1 + L_gR_c + L_2R_c) + s(L_1 + L_g + L_2 + R_gR_cC) + R_g} \qquad (4.5.7)$$

$$\frac{I_o}{V_I} = \frac{(1 + sR_cC)}{s^3L_1C(L_g + L_2) + s^2C(R_gL_1 + R_cL_1 + L_gR_c + L_2R_c) + s(L_1 + L_g + L_2 + R_gR_cC) + R_g} \qquad (4.5.8)$$

$$f_{res} = \frac{1}{2\pi}\sqrt{\frac{L_1 + L_2}{L_1L_2C}} \qquad (4.5.9)$$

substituting the $\boldsymbol{L_1}$ and $\boldsymbol{L_2}$ and capacitance parameters give the resonance frequency as

$$f_{res} = \frac{1}{2\pi}\sqrt{\frac{2 \times 3.125 \times 10^{-3}}{3.125 \times 3.125 \times 10^{-6} \times 18.72 \times 10^{-6}}} = 930Hz$$

Selecting the damping resistor value requires a tradeoff between the switching frequency harmonics and the resonant point harmonics. as the size of the resistor increases the attenuation of the frequencies upon the resonance decreases. In this design the damping resistor value was varied until the frequencies near the resonance were effectively damped and until the switching frequency harmonics were eliminated. The calculated parameters for the LCL filter are summarized in Table 4.2.

Table 4.2: Output LCL filter parameters

Component	**Value**
L_1	3.125mH
L_2	3.125mH
C	18.72μF
R	9.14 Ω
L_g	0.466mH
R_g	0.2525 Ω

The resistance and inductance of the LV grid AAC conductor was taken for the $\boldsymbol{L_g}$ and $\boldsymbol{R_g}$ values. With the values substituted the transfer functions and the resonance frequency can be given by equations (4.5.10) and (4.5.11).

$$\frac{V_O}{V_I} = \frac{2924.8(s+70.31)(s+5845)}{(s+37.6)(s^2+5503s+3.197\times10^7)} \qquad (4.5.10)$$

$$\frac{I_O}{V_I} = \frac{8.1448\times10^5(s+5845)}{(s+37.6)(s^2+5503s+3.197\times10^7)} \qquad (4.5.11)$$

The Frequency response plot of the transfer functions are shown in Figure 4.19 and Figure 4.20. They indicate that the damping has significantly reduced the magnitude of the frequencies at the resonance point of 930 Hz. It also shows that the grid conductor impedance has no significant impact on the filter characteristics.

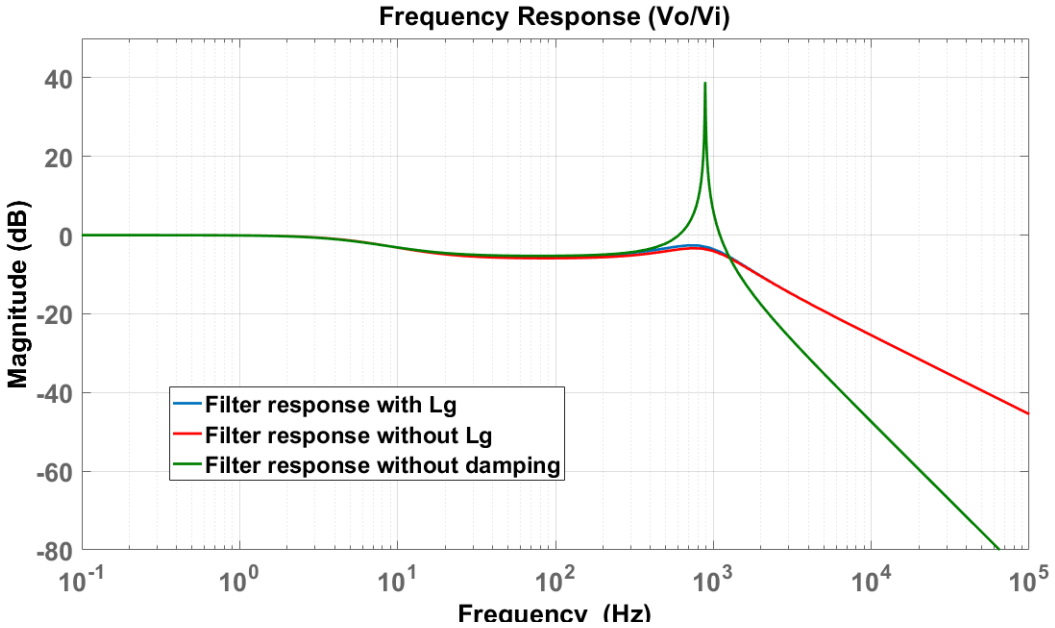

Figure 4.19: Filter response for output voltage

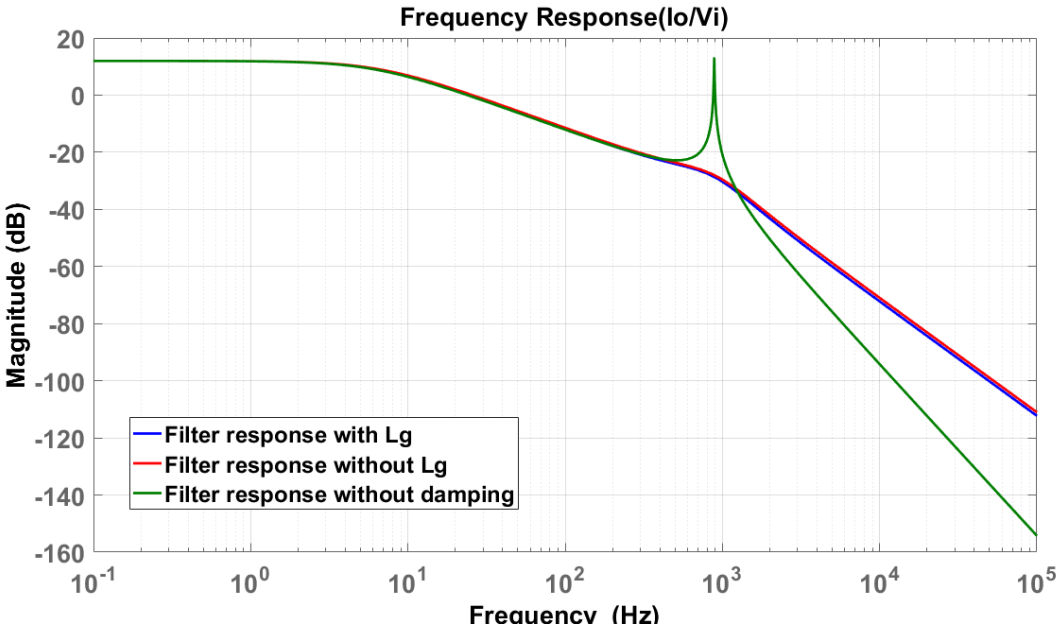

Figure 4.20: Filter response for output current

The designed filter and inverter was simulated with the designed LV grid. The harmonic spectrum of the inverter output voltage and current are shown in Figure 4.21. The harmonic spectrum lies within the limits of the IEEE 519:2014 standard [25] .

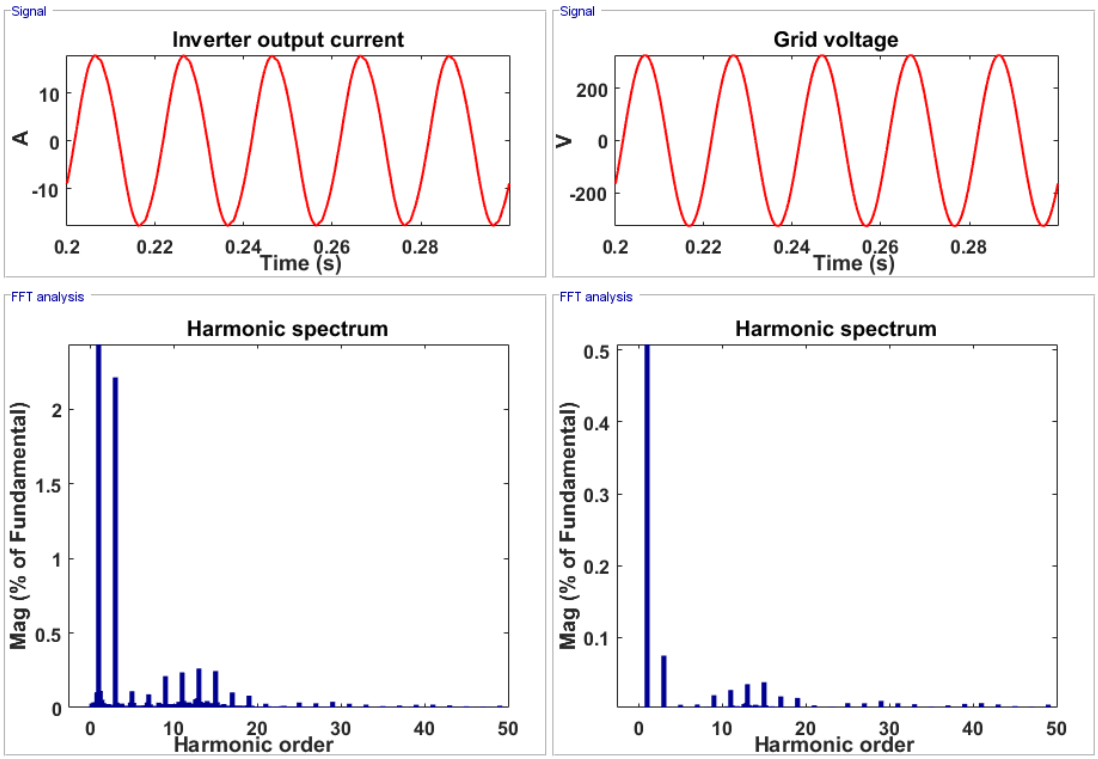

Figure 4.21: Harmonic spectrum for output voltage and current

4.6 DC Link Capacitor

As the power output of the inverter varies sinusoidally, the PV panel does not have the capability to respond to this power variation while maintaining a steady voltage at the DC bus. Therefore, a capacitor is required to act as a buffer to store the energy and minimize the voltage fluctuation. This is known as the DC link capacitor that is connected in shunt between the inverter and the PV panel.

As the inverter in this case is a single phase full bridge with two IGBT pairs, at the beginning of each positive and negative cycle, each leg draws a current from the PV panel side. This current generates a voltage ripple in the DC bus having twice the frequency of the grid frequency. As this ripple is fed back again to the inverter, the inverter generates a third harmonic that is difficult to eliminate using the output filter. The role of the DC capacitor is to minimize this ripple. However, as the size of the capacitor increases, the cost and the bulkiness of the inverter increases making the

design infeasible. Therefore, a good tradeoff is required between the capacitor size and the voltage ripple.

The relationship between the voltage ripple and the output power can be given by equation (4.6.1) [38]. The equivalent series resistance and equivalent series inductance of the capacitor were not taken into account.

If the energy drawn from the capacitor during the first half of the ripple is ***ΔE***, it can be given in terms of the energy stored in the capacitor as

$$\Delta E = \frac{1}{2} C_{dc} V_{dc}^2 - \frac{1}{2} C (V_{dc} - \Delta V_{dc})^2 \qquad (4.6.1)$$

Since this period is 1/8th of the total 50 Hz cycle time (since the ripple is twice the grid frequency) the power output can be given by equation (4.6.2)

$$P_{out} = \frac{\Delta E}{\left(\frac{T_s}{8}\right)} = 8 f_{ac} \Delta E \qquad (4.6.2)$$

$$P_{out} = 4 f_{ac} C_{dc} \left({V_{dc}}^2 - (V_{dc} - \Delta V)^2 \right)$$

By rearranging, the percentage ripple of the DC bus voltage can be given by equation (4.6.3)

$$\Delta V\% = \left\{ V - \left(\sqrt{V^2 - \frac{P_{out}}{4 f_{ac} C_{dc}}} \right) \right\} \times \frac{100}{V} \qquad (4.6.3)$$

Where f_{ac} Is the grid frequency, V_{dc} is the DC bus voltage and C_{dc} is the DC link capacitance. For this design, a DC link capacitor of 1000 μF with a voltage rating of 600 V was selected as this is a commonly available capacitor size and is relatively low in cost. The voltage rating of 600 V was selected as the open circuit voltage of the PV array is 535 V.

The ripple magnitude changes with the power output and DC bus voltage. The surface plot in Figure 4.23 and waveforms in Figure 4.22 show the variation of the percentage ripple with power output and voltage for the selected capacitor. As the

power output is at its maximum and voltage is minimum the ripple shows a maximum value of 5.7%. It also shows a linear decrease with the power output. As the power output and DC bus voltage is continuously varying throughout the operation, the selected capacitor was considered suitable for this design. The harmonic values shown in Figure 4.21 also indicate that they are well within the limits of the specified IEEE 519:2014 standard.

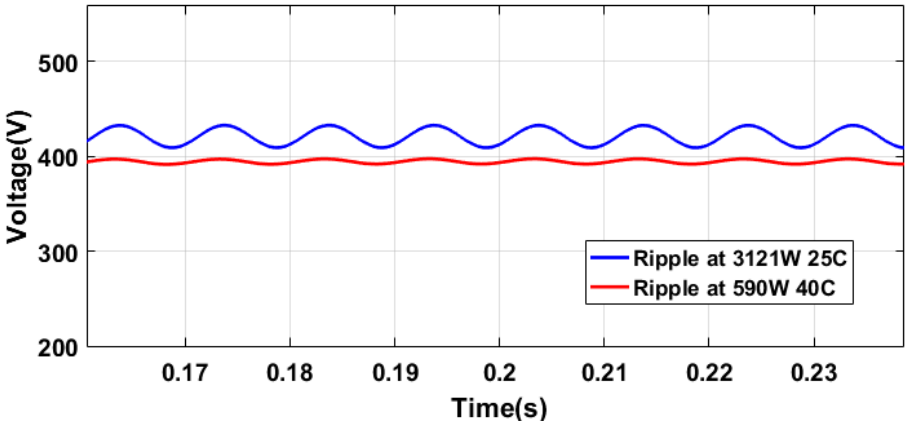

Figure 4.22: DC voltage ripple at different power outputs

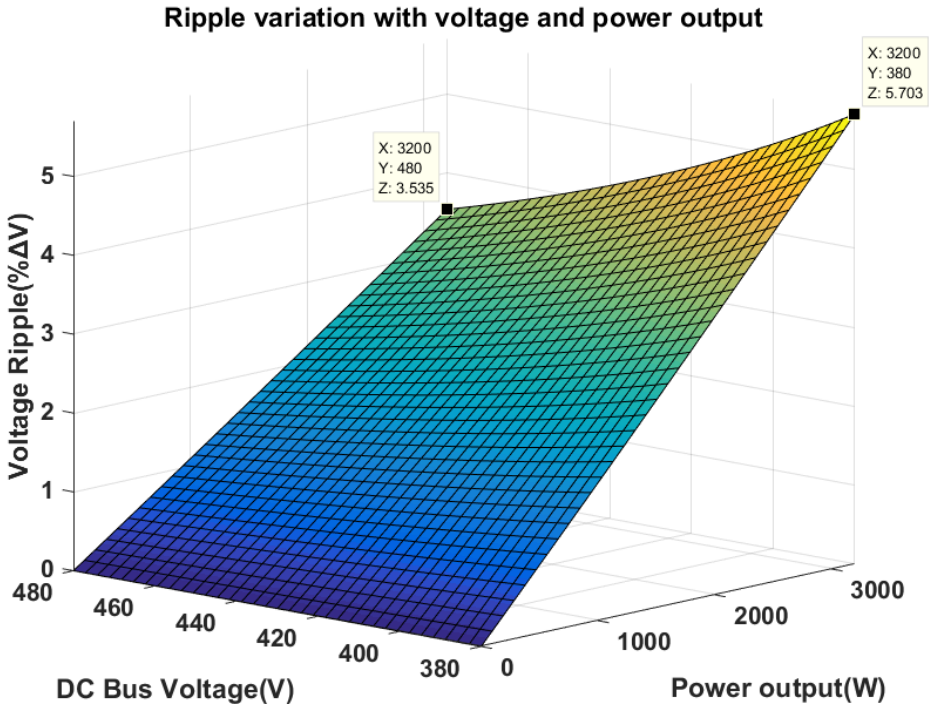

Figure 4.23: Ripple magnitude variation with Voltage and power output

4.7 Transformerless Inverter

The transformerless inverter was developed in the Simulink platform with all the necessary designed components. The block diagram of the designed system is shown in Figure 4.24. The Simulink model developed is shown in Appendix B.

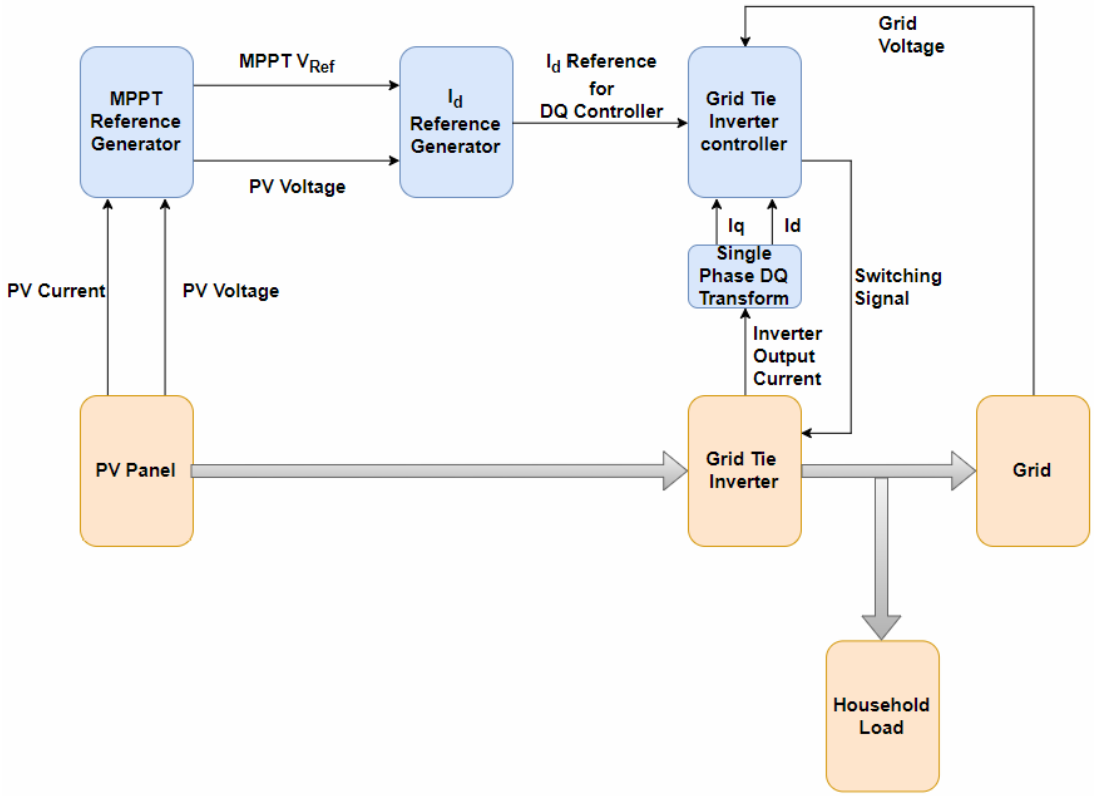

Figure 4.24: Block diagram of transformerless inverter

In the system shown in Figure 4.24 , the MPPT reference generator generates a voltage reference that is required to obtain the maximum power output of the PV array. Based on this reference voltage, the output current reference $\boldsymbol{I_{d\_ref}}$ is generated and given to the grid tie inverter controller. Based on the $\boldsymbol{I_{d\_ref}}$ the required power is injected to the grid by the controller while maintaining synchronism with the grid via the PLL.

Although this system is simple and has a low component count, it has known drawbacks. Therefore, three systems were proposed based on a solid-state transformer topology described in the literature review. The proposed systems and the design of two DAB based systems are described in the next chapter.

5 DUAL ACTIVE BRIDGE BASED PV INVERTER

5.1 Proposed SST Based Grid Tie Inverter Topologies

The dual active bridge (DAB) and the tri active bridge (TAB) topologies used in the solid-state transformer (SST), have many advantages that can be utilized to overcome the drawbacks of the transformerless inverter. The three-stage solid state transformer topology was selected to develop the PV inverter arrangements as it provides most of the benefits. The dual active and tri active bridge configurations of the SST were utilized for the designs. Three systems were developed and compared with the transformerless inverter.

Two inverter configurations were designed and simulated based on the dual active bridge as it facilitates bidirectional power flow. The block diagram of the dual active bridge based inverter is shown in Figure 5.1.

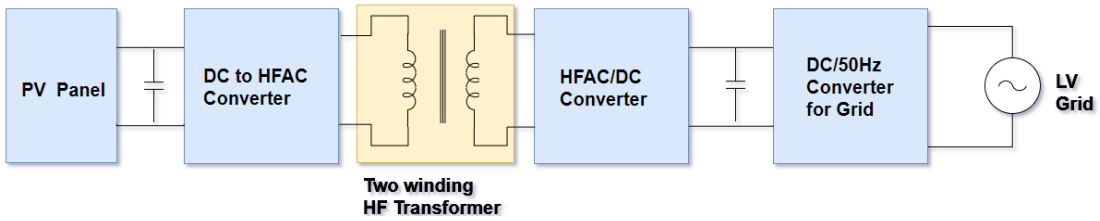

Figure 5.1: Dual active bridge based PV configuration

First configuration is to have the household loads connected at the grid side similar to the transformerless inverter. The second configuration connects the household load directly to PV panel output via an additional DC to 50 Hz inverter while utilizing the dual active bridge to supply power to the grid. This provides galvanic isolation for the PV array and the household loads. The DAB will have to be configured for bidirectional power flow as power will have to be drawn from the grid to facilitate the household loads at night. Additional to the controllers mentioned in the previous chapter for the PV system, more controllers are required to maintain the DC bus voltages of the DAB and the household side inverter.

The third arrangement is obtained by using a triple active bridge that can connect the household, PV panels and Grid with isolation. It is shown in Figure 5.2.

This configuration provides multiple advantages over the existing transformerless inverter. Due to the isolation of the three systems, the harmonic propagation from either side is eliminated. In the occurrence of a fault in either the household or PV panel side, the fault can be isolated with minimal impact to other ports. The presence of an isolated DC bus at the household side provides provisions for distributed resource interconnection. Reactive power compensation and power factor correction can be achieved by the grid tie inverter as good voltage regulation is possible in both household and grid side DC buses.

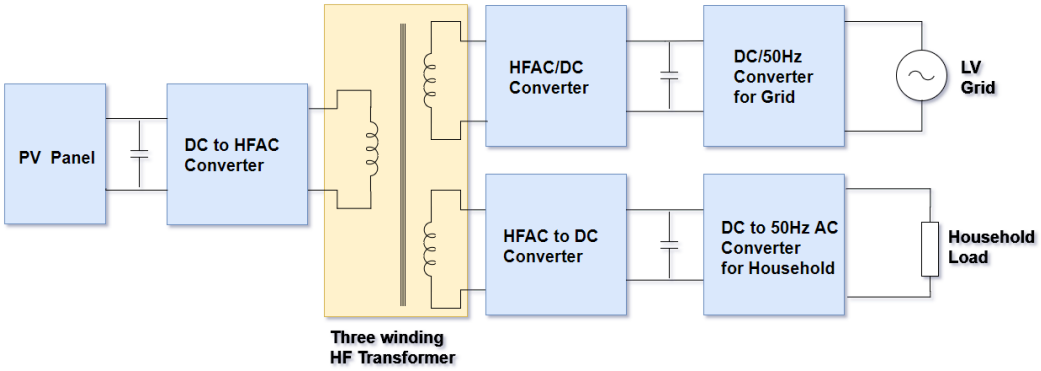

Figure 5.2: Tri active bridge based PV configuration

In comparison with the second DAB system, the TAB based system requires an additional controller for the household side DC bus. The design of the TAB based system and its mathematical derivations are discussed in chapters 6 and 7.

The design of the two DAB based inverter arrangements are presented in this chapter. The DAB consists of two full bridge converters, a high frequency transformer and a controller to maintain the voltage at the grid side DC bus. The determination of the leakage inductance required in the HF transformer and the controller design for the voltage controller are presented. Finally, the Simulink model integrating the Grid side inverter, PV panels and the associated controller arrangement is described.

5.2 Dual Active Bridge

A typical schematic of the dual active bridge (DAB) is shown in a Figure 5.3. Based on the power and switching frequency requirements, IGBT's or MOSFETS can be used for the switching devices. In this case IGBT's are preferred as the power flow capacity of the DAB in this design lies in the kW range with operating voltages around 450V.

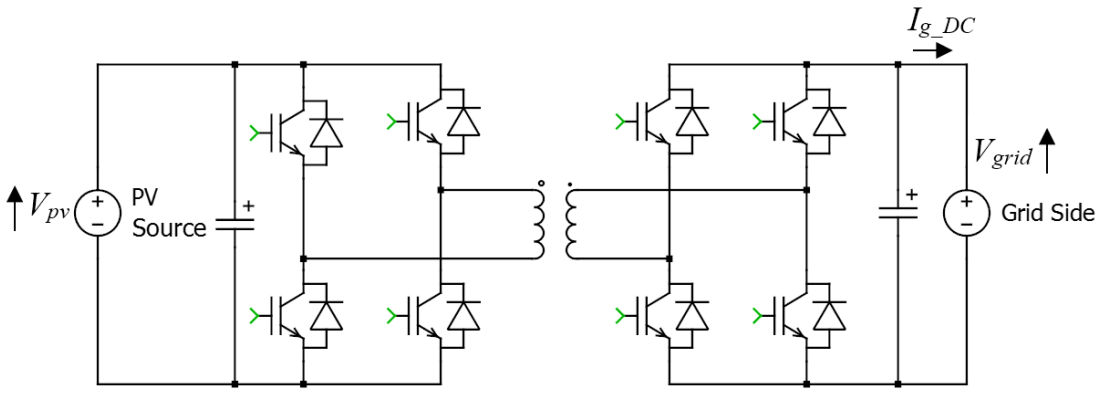

Figure 5.3: Dual active bridge

The dual active bridge operates based on a modulation technique known as phase shift modulation (PSM). In PSM, both the bridges operate with a duty ratio of 50%. The amount of power flown from one bridge to the other is determined by adjusting the phase shift between the waveforms. The power flow, presented by W.A Doneker [12] is shown in equation (5.2.1) which gives the power transfer between the bridges in terms of phase shift, DC voltages, switching frequency and HF transformer leakage inductance.

$$P_{pv,grid} = \frac{V_{pv}V_g}{2\pi fL}\delta_{pv,g}\left(1-\frac{|\delta_{pv,g}|}{\pi}\right) \qquad (5.2.1)$$

Where

$\boldsymbol{V_{pv}}$ = PV panel side DC bus voltage

$\boldsymbol{V_g}$ =Grid side DC bus voltage

$\boldsymbol{\delta_{pv,g}}$=Shift between PV panel side and grid side bridges

$\boldsymbol{f}$=Switching frequency

$\boldsymbol{L}$=Leakage inductance of the HF transformer

The value of $\boldsymbol{\delta_{pv,g}}$ varies between 0 to $\pi/2$ giving a maximum power output at $\pi/2$. Above this value the power output decreases giving multiple solutions for the equation. Therefore, in general the value of $\boldsymbol{\delta_{pv,g}}$ is limited to vary in the range of 0 to $\pi/2$.

Another important parameter of the dual active bridge is that given identical input and output voltages, the bridge facilitates soft switching. This is shown in Figure 5.4 where a voltage ratio (***d***) close to 1 between the input and output maintains soft switching over the overall operating range.

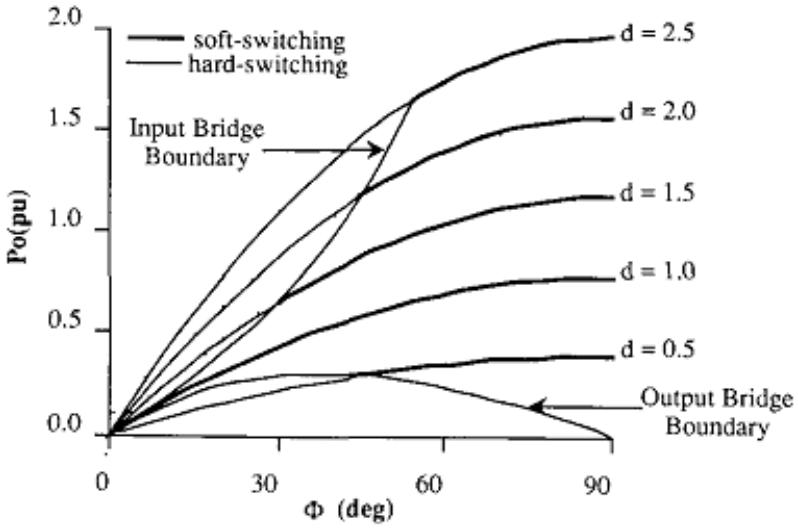

Figure 5.4: Soft switching boundaries of the DAB [12]

Maintaining an exact equivalent voltage ratio of 1 is however not practical in this design as the PV panel output voltage varies with the MPPT operation. However, the ratios are maintained closer to 1 by having identical number of turns at the two windings of the HF transformer. Designing the switching devices and snubber circuits to obtain soft switching are not focused in this thesis and is considered as a future improvement.

5.2.1 Optimal phase shift and leakage inductance

The existing household system is rated to supply a capacity of 7 kW. Therefore, the maximum power flow capacity of the dual active bridge was taken as 7 kW. In order to facilitate this power flow, a suitable leakage inductance parameter has to be

determined to design the HF transformer. The switching frequency for this application was selected as 20 kHz as it provides a good tradeoff between the output filter sizes and switching losses. Since the operating voltage range of the PV array was taken as 330 V to 450 V in the previous chapter, a midpoint of 390 V was taken for the input voltage. Using these parameters, the power output characteristics for different leakage inductances and varying phase shifts were plotted in Figure 5.5 based on equation (5.2.1).

For optimal operation, the maximum phase shift of the dual active bridge should be around 30% of the total operating range [39] . However, reducing the leakage inductance excessively reduces the required phase shift for small power variations making it difficult to control. The smaller the phase shift the more it is affected by the dead time of the switching devices. Furthermore, selecting a higher leakage inductance causes large phase shifts for small load variations, leading the output voltage controller to take large steps and become unstable. Therefore, for optimal operation, a leakage inductance of 50 μH was taken for the simulation as it gives the required maximum power output of 7 kW in 21 º, which is around 30% of the 0 to π/2 operating range.

The phase shift variations for the maximum and minimum voltages of the PV array are shown in Figure 5.5.

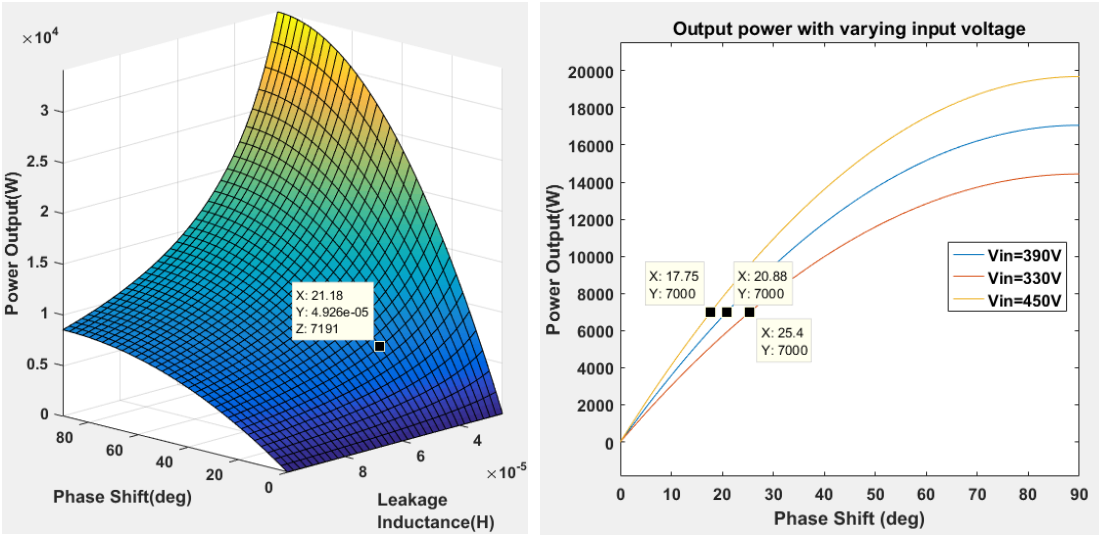

Figure 5.5: Power output variation with phase shift and leakage inductance

Although there is a phase shift variation for the 7 kW power output at different input voltages, this is acceptable as the input voltage is not rapidly varying.

5.3 High Frequency Transformer

The High frequency transformer is the core component of the dual active bridge that provides galvanic isolation. The transformer used in this application is different from the conventional 50 Hz transformer as its operating frequency lies in the kHz range. Low coercively is a main requirement in these transformers due to their high operating frequency. The core construction material is usually powdered ferrite or Nano-crystalline. Shell type, toroidal or coaxial type cores are the most common core shapes. However, a coaxial type transformer is much suitable for this application as it provides good controllability over the leakage inductance in the design [40].

As the operating frequency of the dual active bridge is in the kHz range, the conventional current carrying conductors get subjected to high amounts of losses due to the skin effect. The skin effect causes the current to travel in the outer layers of the conductors reducing the effective area and increasing the effective resistance. The solution for this is to use bundled conductors with multiple insulated strands known as Litz wires. If each strand is designed to have a diameter less than the skin depth of the overall conductor carrying a current in the required frequency, the losses can be significantly reduced.

The main requirements of this design are to have a transformer with a leakage inductance of 50μH and identical transformer ratios. Hence the transformer has to be designed to satisfy these requirements. Similar toroidal and coaxially wound transformer designs with identical ratios have been presented in literature [41] . A 10 kVA toroidal transformer with identical transformer ratios have been presented by S. Inoue [42] for a dual active bridge. Another design for a coaxially wound transformer has been presented by M.H Kheruwala [40] for a triple active bridge. Having identical transformer ratios facilitate soft switching and simplifies the calculations in design.

However, In reality designing a transformer to have a specific leakage inductance can be difficult. In that case the desired inductances and resistances can be

obtained by adding them in series with the transformer windings. A design procedure for designing inductors for a three port solid state transformer is presented by Z.G Abdelmessih [43] . Design of these components are not covered in this thesis. The required parameters for the HF transformer are calculated for the simulations.

5.4 Output Voltage Controller

The output voltage and the current of the dual active bridge varies with the phase shift between the two switching waveforms to provide the required power given by the equation (5.2.1). Therefore, it is required to have a controller to maintain the voltage at the grid side DC bus by changing the phase shift to facilitate the power output from the PV panels. The equation (5.4.1) provides a harmonic model for the relationship between the output voltage of a dual active bridge in terms of phase shift, output current and input voltage [44] .

$$\frac{dV_{grid}(t)}{dt} = -\frac{I_{g\_DC}}{C} + \frac{8}{C\pi^2}\left(\frac{N_p}{N_s}\right)\sum_{n=0}^{N}\frac{1}{\left(2n+1\right)^2}\times\left\{\begin{array}{l}\dfrac{V_{pv}}{\left|Z\left[n\right]\right|}\cos\left\{\left[2n+1\right]\delta_g - \varphi\left[n\right]\right\} \\ -\dfrac{N_p}{N_s}\dfrac{V_{grid}(t)}{\left|Z\left[n\right]\right|}\cos\left\{\varphi\left[n\right]\right\}\end{array}\right\} \quad (5.4.1)$$

Where

$$Z\left[n\right] = \sqrt{R_L^2 + \left(\left[2n+1\right]\omega_s L\right)^2} \quad \textit{and} \quad \varphi\left[n\right] = \tan^{-1}\left(\frac{\left[2n+1\right]\omega_s L}{R_L}\right)$$

where

R_L - transformer winding resistance I_{g_DC} - output current

As this model is nonlinear due to the Fourier summation terms, the Taylor series expansion can be used to linearize this model around a selected operating point. The linearized model is shown in equation (5.4.2). The $\boldsymbol{I_{out}}$ variable was considered fixed during linearization as it varies with the external load and can be considered as an external disturbance.

$$\frac{d\Delta V_g}{dt} = A\Delta V_g + B\Delta\delta_g$$

where

$$A = \left\{ -\frac{8}{C\pi^2}\left(\frac{N_p}{N_s}\right)^2 \sum_{n=0}^{N}\left[\frac{\cos\left(\varphi[n]\right)}{[2n+1]^2\,|Z[n]|}\right]\right\} \qquad (5.4.2)$$

$$B = \left\{ \frac{8V_{pv}}{C\pi^2}\left(\frac{N_p}{N_s}\right)^2 \sum_{n=0}^{N}\left[\frac{\sin\left(\varphi[n]-[2n+1]\delta_0\right)}{[2n+1]|Z[n]|}\right]\right\}$$

Taking the Laplace transform of the equation, the transfer function can be given by equation (5.4.3)

$$sV_g(s) = AV_g(s) + B\delta_g(s)$$

$$\frac{V_g(s)}{\delta_g(s)} = \frac{B}{s-A} \qquad (5.4.3)$$

This shows that the relationship between the output voltage and the phase shift can be given by a single first order transfer function. A simple PI controller can be used to control the voltage output of this plant.

If the plant is $G_p(s) = \frac{V_g(s)}{\delta_g(s)} = \frac{B}{s-A}$, a transfer function of a PI controller can be written as $G_c(s) = K_p\left(1 + K_I\frac{1}{s}\right)$

The open loop transfer function of the plant with the controller can be given by equation (5.4.4).

$$F(s) = G_p(s).G_c(s) = K_p\left(1 + K_I\frac{1}{s}\right)\left(\frac{B}{s-A}\right) \qquad (5.4.4)$$

With the transfer function of the system presented by equation (5.4.4), this system was developed in Simulink and the closed loop transfer function was tuned using the Simulink PID tuner. The parameters used for determining the ***A*** and ***B*** values of the model are shown in Table 5.1.

Table 5.1: Parameters used for tuning the dual active bridge controller

Switching frequency(f)	20kHz
Leakage inductance (L)	50μH (25μH per winding)
Winding resistance(R)	20mΩ (10mΩ per winding)
Transformer Ratio(N_p/N_s)	1:1
Initial phase shift (δ_0)	10.6 º
Number of Fourier terms (N)	10
Output DC link capacitance (C)	1000μF
PV Panel output voltage(V_{pv})	390V

The initial point of $\boldsymbol{\delta_0}$=10.6º was taken as the midpoint of the operating range of 0 to 21.18 º, and $\boldsymbol{V_{pv}}$ was taken as 390 V since it is the midpoint of the operating voltage of the PV array.

Calculating the A and B values with the parameters given in Table 5.1 gives

$\boldsymbol{A}$ = - 0.04165

$\boldsymbol{B}$ = 5.46×10^4

The transfer function can be implemented and tuned using the Simulink PID tuner. The model used for tuning the controller is shown in Figure 5.6.

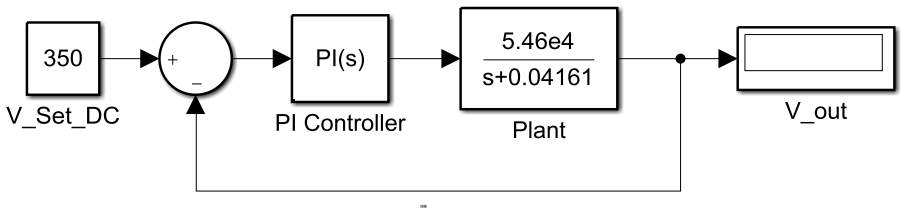

Figure 5.6: Simulink model used for controller tuning

The closed loop plant was tuned to respond within 1.5 ms period for a standard step response. The step response and the tuned controller parameters are shown in Figure 5.7.

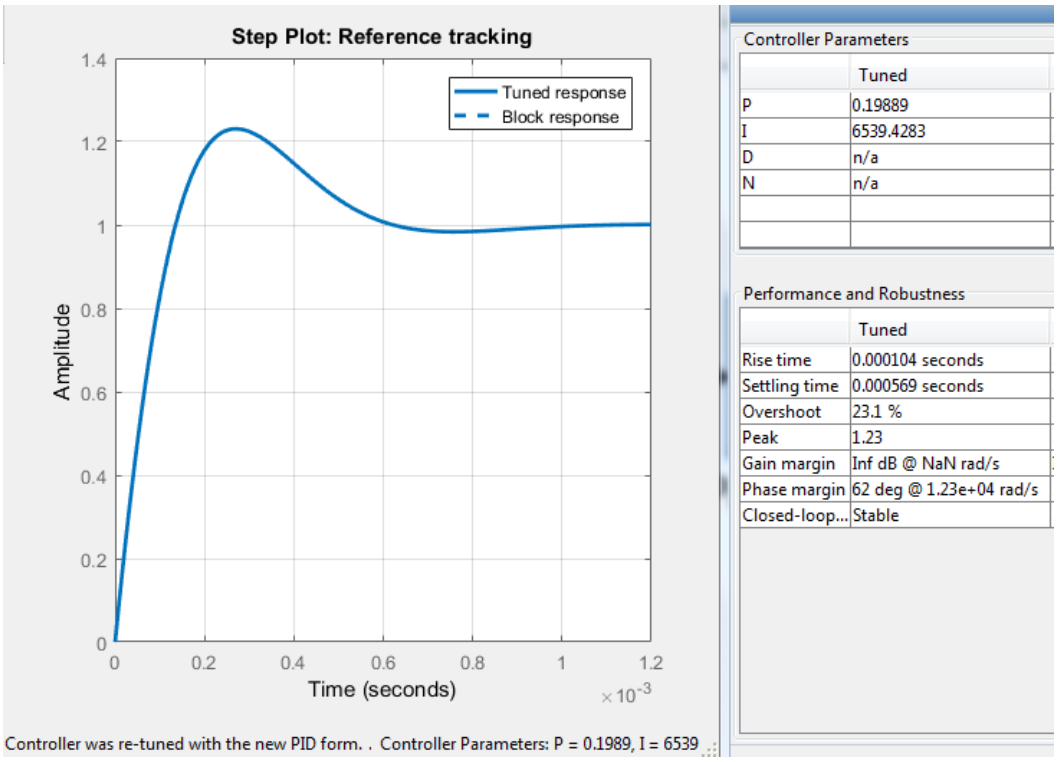

Figure 5.7: Tuned response of output voltage controller

With the tuned controller parameters, the open loop and closed loop transfer functions can be given by equation (5.4.5) and (5.4.6).

$$F(s) = \frac{8039.6(s+6539)}{s(s+0.04165)} \qquad (5.4.5)$$

$$R(s) = \frac{G_p(s)G_c(s)}{1+G_p(s)G_c(s)} = \frac{8039.6(s+6539)}{(s^2+8040s+5.257\times10^7)} \qquad (5.4.6)$$

This controller is tuned for a particular set point in $\boldsymbol{\delta_0}$ and $\boldsymbol{V_{pv}}$. But the parameter $\boldsymbol{B}$ is a function of $\boldsymbol{V_{pv}}$ and $\boldsymbol{\delta_0}$. Both of these parameters vary with operating conditions. As the plant transfer function also varies with these values, it is necessary to verify how the controller responds for the maximum and minimum limits of $\boldsymbol{B}$. The surface plot in Figure 5.8 shows the variation of the parameter $\boldsymbol{B}$ with the $\boldsymbol{\delta}$ and $\boldsymbol{V_{in}}$.

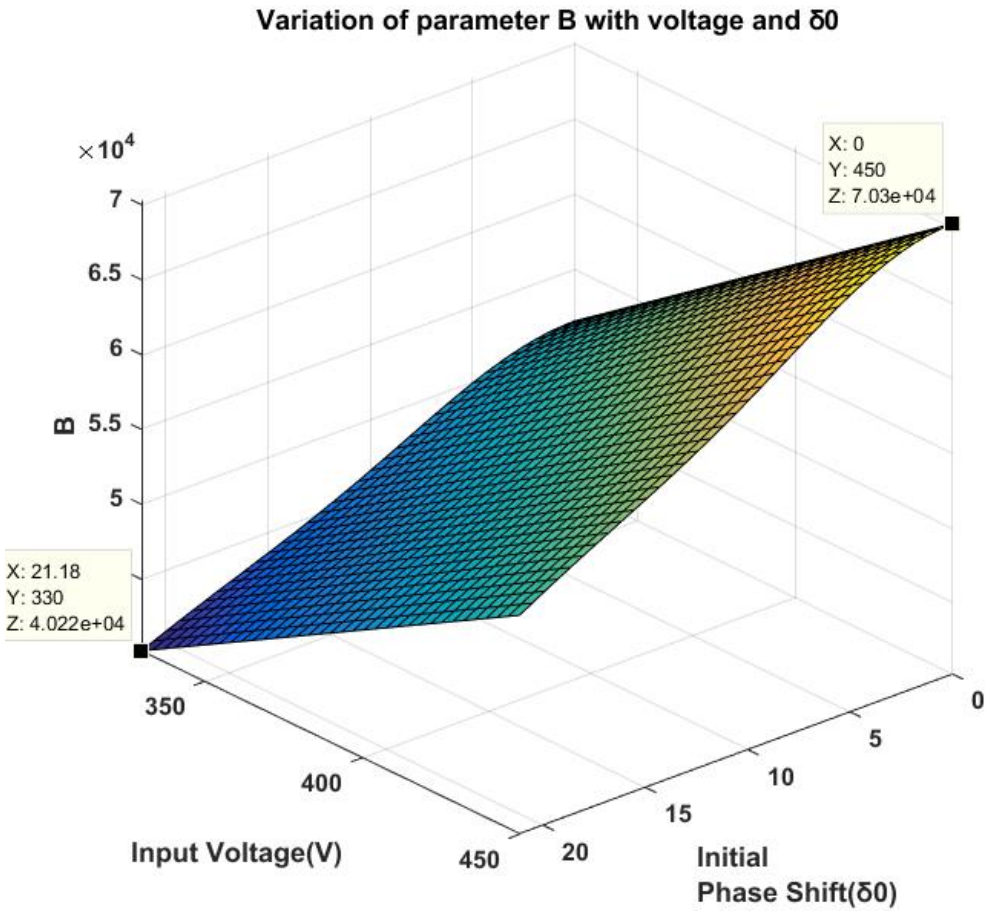

Figure 5.8: Variation of B with input voltage and phase shift

According to Figure 5.8, the minimum value of $\boldsymbol{B}$=4.022x10^4 was observed at lowest voltage of 330 V and maximum phase shift of 21.18º. The maximum value of $\boldsymbol{B}$=7.03x10^4 was observed at a maximum voltage of 450 V and minimum phase shift of 0 º. The plant transfer functions can be derived for these upper and lower limits of $\boldsymbol{B}$. Hence the step responses and the pole zero plots of the closed loop transfer function were plotted using MATLAB. The plotted responses are shown in Figure 5.8. Both the step responses and pole zero plots show that the system stays stable at the maximum and minimum limits with only variations in response time.

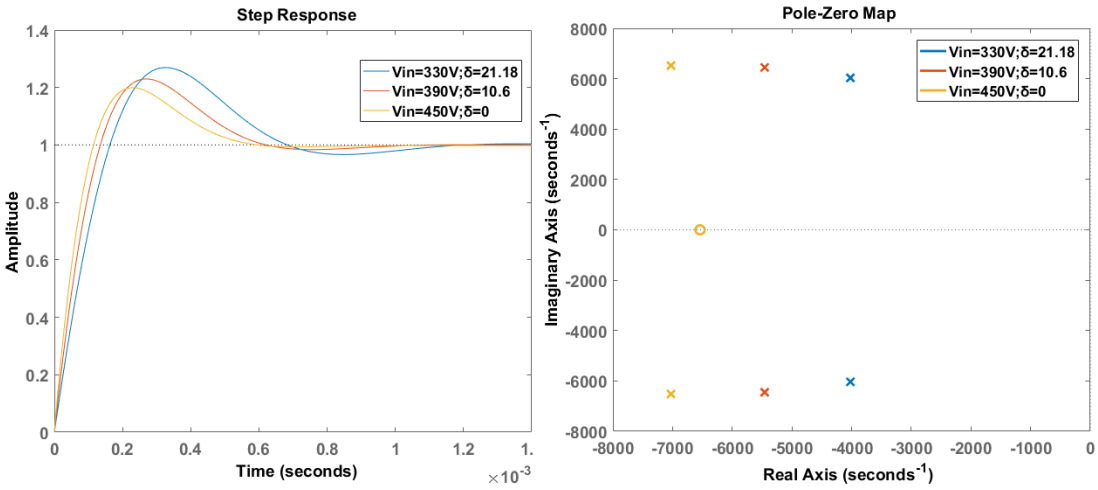

Figure 5.9: Step responses and pole zero plots with varying B

The response of the output voltage for a load step of 7 kW is shown in Figure 5.10. The response of the DC bus voltage for the step load is as expected, and the voltage reaches the set point in about 1.5 ms which is acceptable. The magnitude of the ripple in the voltage has increased after the load step was applied. This is within limits and is expected as the ripple magnitude increases with the increasing load.

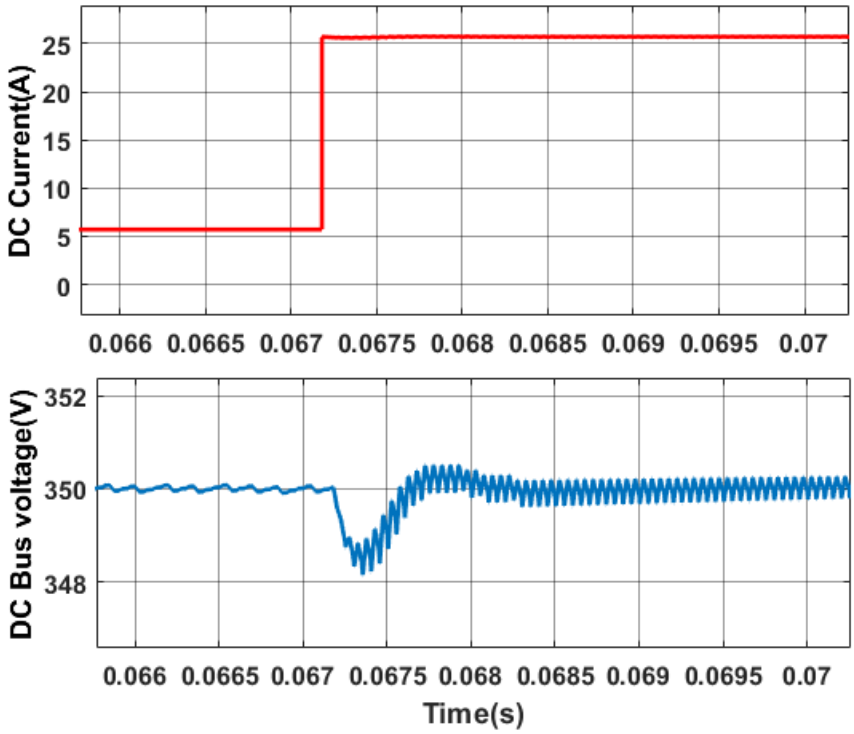

Figure 5.10: Output voltage variation for a load step of 7kW

Since the plant used to tune the controller is based on a small signal model, the tuned parameters are valid only for small variations around the selected set point. Even through the selected controller configuration is valid for load steps up to the maximum load of 7 kW, the voltage of the DC bus might deviate in large steps during a Fault condition. Therefore, the controller should have the ability to restore back to normal operation if the fault is cleared instantaneously. Therefore, a different set of PI gain values were tuned using the Ziegler–Nichols method to respond for large voltage variations. These PI gain values gradually bring the voltage up to the required set point of 350 V. Once the DC bus voltage reaches the set point of 350 V, the PI controller is switched to the derived PI gain values. The controller configuration and the adaptive switching mechanism are shown in Figure 5.11.

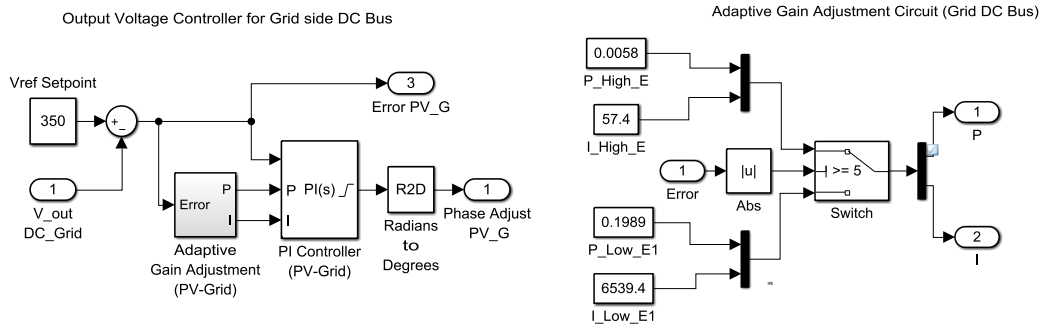

Figure 5.11: Simulink models of output voltage controller

5.4 Gate Pulse Generation

In order to provide the phase shift to the switching devices, a gate pulse generation scheme was designed. The developed gate pulse generation scheme is shown in Figure 5.12. The phase shift generated was converted to a time delay, and a zero-order hold of $5x10^{-5}$ s was used to give the time delay only at the start of every switching cycle. A square wave of 20 kHz was generated and the phase shift was given to this waveform in a form of a variable time delay. When there is a no load condition, the phase shift generated by the controller oscillates around zero. This generates negative phase shift values. As negative time delays cannot be generated, a time delay relevant with the magnitude of the negative phase shift was given to the PV panel side bridge. The positive phase shifts generated was given to the grid side bridge while the negative phase shifts were given to the PV panel side bridge. The “compare to zero

block" was used to determine the polarity of the phase shift and give the absolute value of time delay to the necessary bridge. An upper limit was set in the variable time delay block to limit the phase shift above π/2. As the two series connected switching devices of each bridge are operated in a complementary manner, the NOT gate was used to generate the complement of the output signal.

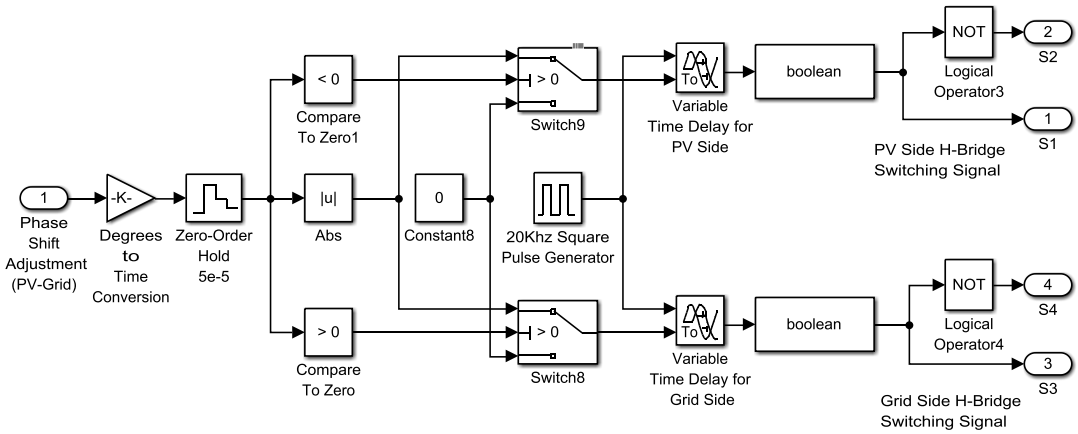

Figure 5.12: Simulink model for gate pulse generation circuit

5.5 DAB with PV System

This dual active bridge was placed between the PV panel and the grid tie inverter of the transformerless inverter. The DAB controller response for load variations is quite fast compared to the other controllers. Therefore, this acts as a steady DC bus with a fixed output voltage of 350 V at the grid tie inverter side. As a result, the grid tie inverter voltage input is not subjected to a varying voltage as the transformerless inverter.

The designed parameters and systems used in the transformerless inverter were used with the DAB integrated in the DC bus. The load current drawn at the grid tie inverter side is sinusoidal and is not a step change as shown in Figure 5.10. This causes the voltage variations at the DC bus to become minimal. With the DAB connected between the grid tie inverter and the PV array, two connection arrangements for the household load were implemented.

5.5.1 Household load at grid side

This is similar to the existing arrangement of the transformerless inverter. The I_{d_ref} generated by the I_d reference generator controls the power output through the grid tie inverter. The DAB voltage controller maintains the DC voltage at the grid side DC bus providing a good voltage regulation. The control loop of the DAB is independent from the I_{d_ref} reference generator and the grid tie inverter. The block diagram of this arrangement is shown in Figure 5.13.

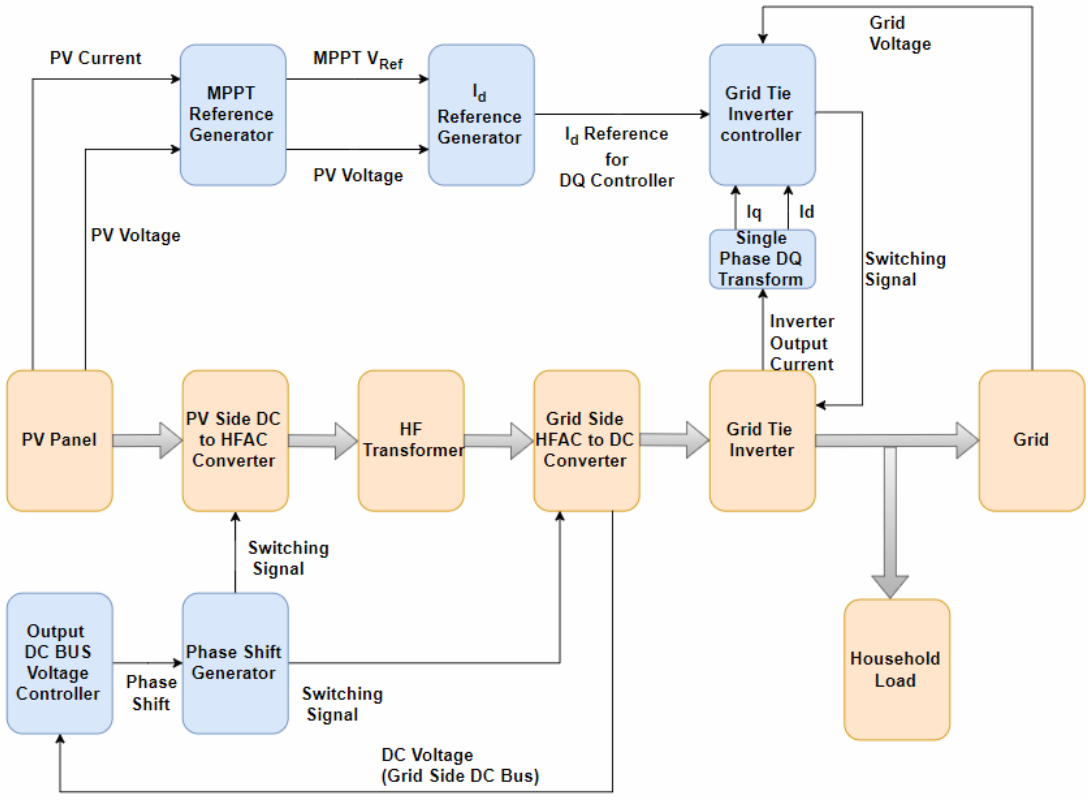

Figure 5.13: Block diagram for DAB inverter with load at grid side

The disadvantage of this system is that as the household load is connected to the grid side, the harmonic generating loads at the household side draw harmonic currents from the grid similar to the transformerless inverter. Furthermore, the faults at the household side are not isolated or limited as they are directly connected to the grid.

5.5.2 Household load at PV panel side

The drawbacks of the above system were eliminated by connecting the household loads at the PV panel side. This isolates the household side and the PV panels from the grid, providing an advantage to the grid over load side harmonics and fault currents. However, an additional inverter was needed to convert the DC into 50 Hz AC and provide it to the household. An H-Bridge inverter similar to the grid tie inverter was used with the same filter arrangement. The controller for the inverter is shown in Figure 5.14.

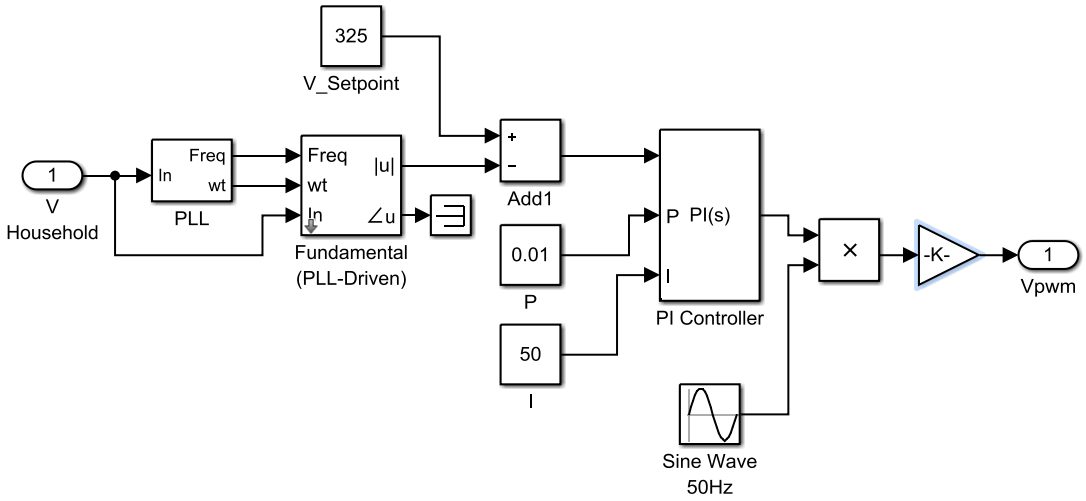

Figure 5.14: Voltage controller for household inverter

As the household is connected to the PV array DC bus, this setup requires the DAB to maintain bidirectional power flow. When the household loads are not available, the I_{d_ref} reference generator feeds the PV generated power to the grid while maintaining the MPP voltage at the DC bus, operating similar to the previous configuration. Once the household load is turned on, the voltage at the PV panel side DC bus drops as power is drawn to the household. The I_d reference generator senses this drop and changes the I_{d_ref} reference of the grid tie inverter to maintain the MPP voltage at the PV panel side DC bus.

If the household power requirement becomes higher than the power generated by the PV panel, the I_d reference generator makes the I_{d_ref} reference negative as there isn't sufficient power to maintain the required voltage at the PV panel side DC bus. This negative I_{d_ref} reference causes the grid tie inverter to operate as a converter and

draws power from the grid to the grid side DC bus causing its voltage to rise. The DAB voltage controller senses this voltage increase and reverses the power to flow in the other direction facilitating the power requirement at the PV panel side while maintaining the grid side DC bus voltage at 350 V. The block diagram of the system is shown in Figure 5.15

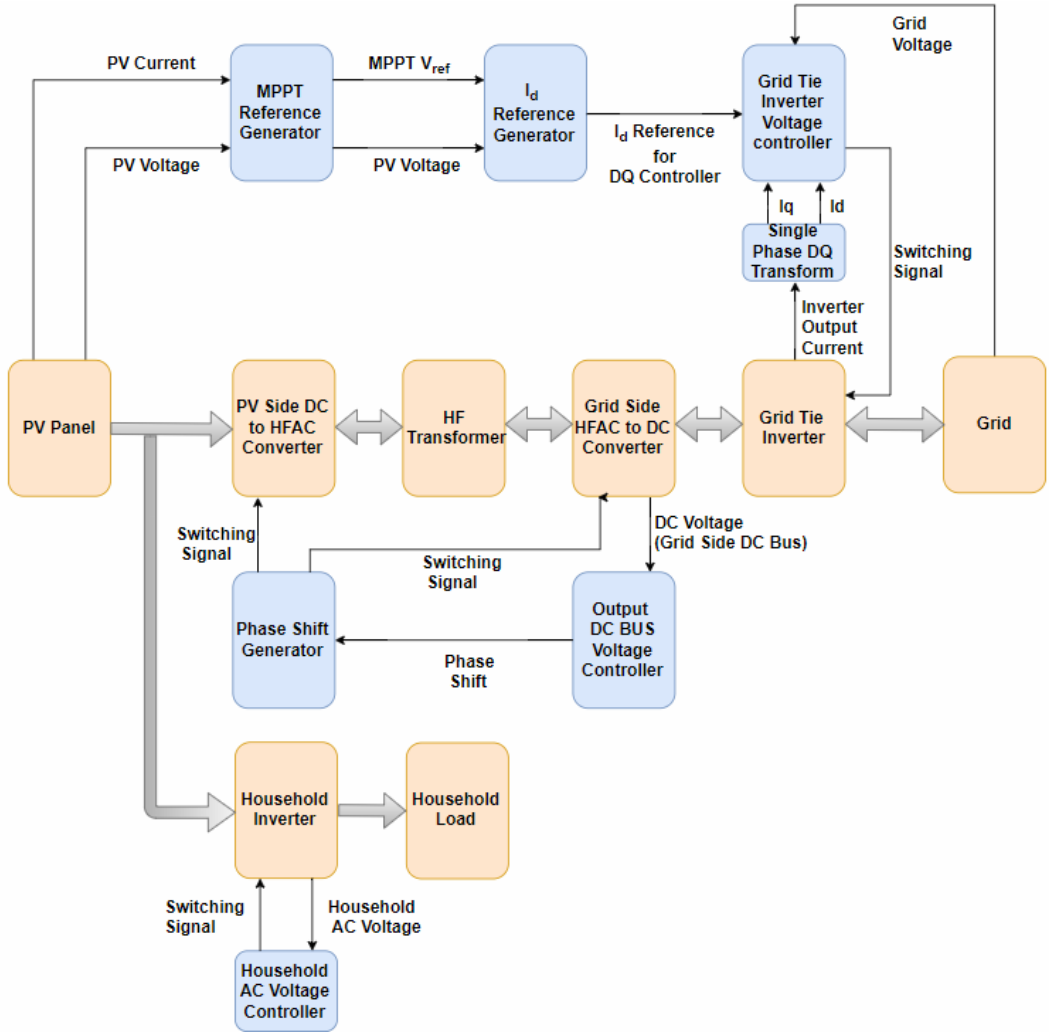

Figure 5.15: Block diagram for DAB inverter with load at PV array side

Even though this inverter does provide fault current limiting and harmonic isolation, the household side voltage gets subjected to variations as the PV panel output voltage varies with the irradiance.

The Simulink models for the two configurations are shown in Appendix C and D.

6 MATHEMATICAL MODELING OF THE TRI ACTIVE BRIDGE

The tri active bridge (TAB) is an expansion of the dual active bridge (DAB) arrangement. It consists of three H-Bridge converters linked with each other using a three winding HF Transformer. Similar to the DAB, the series connected switching devices of the H bridge operate in a complementary manner under phase shift modulation to generate a bipolar square waveform. A TAB converter is shown in Figure 6.1 with the associated currents and voltages.

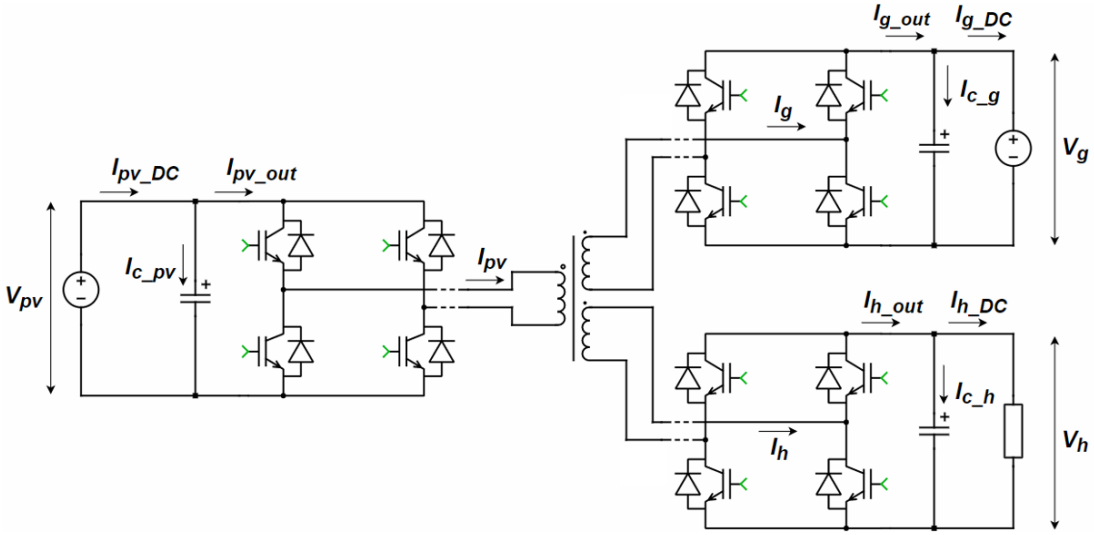

Figure 6.1: Tri active bridge

The TAB used in this design has one bidirectional power flow port at the grid side and have two unidirectional power flow ports at the household and the PV panel side. The PV panel supplies power to both the grid and the household during daytime, and once the household load increases above the output of the PV array, power is drawn from the grid in the inward direction.

A mathematical model is required to accurately understand the behavior of the TAB. It is required to accurately model the controllers to facilitate smooth power flow and maintain steady DC voltages. A detailed mathematical derivation of a harmonic model for the dual active bridge with a two winding transformer can be found in literature [45] .The methods used in the derivation for the DAB are adopted in this mathematical derivation of the TAB. This chapter consists of the derivation of the

mathematical model for the output currents and voltages of the TAB. The derived mathematical model is compared with a simulated model for justification.

6.1 Tri Winding Transformer Equivalent Circuit

Similar to the DAB, the TAB used in this application utilizes a high frequency transformer with three identical turn ratios. Therefore, the transformer ratios were taken as 1:1:1 similar to the transformer used in the dual active bridge. The tri winding transformer equivalent circuit is shown in Figure 6.2 with the magnetizing branch, leakage inductances and resistances.

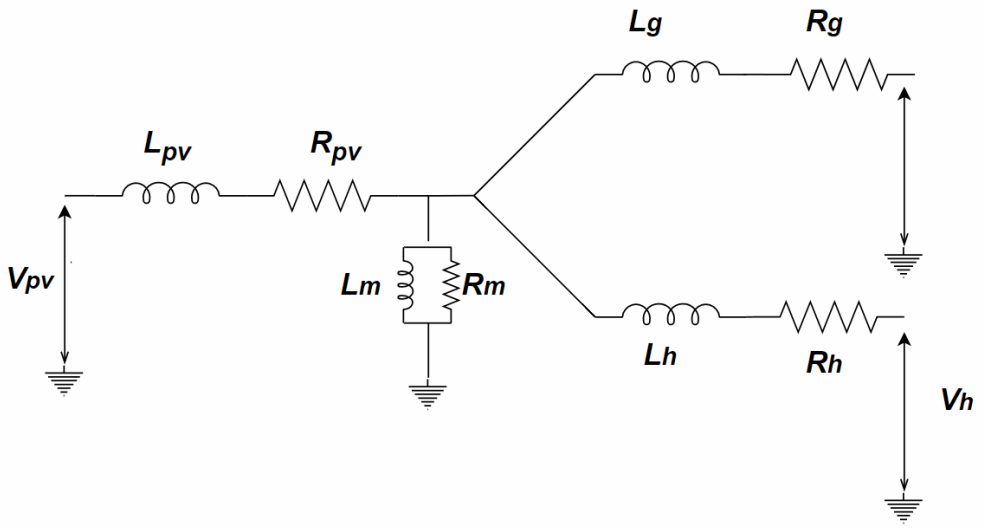

Figure 6.2: Three winding transformer equivalent circuit

The magnetization parameters of the HF transformer are significantly higher than the leakage inductance and the resistance of the windings. Hence the magnetization branch was considered open circuit and was not considered for this derivation.

6.1.1 Calculations of the equivalent circuit parameters

The leakage inductance of a three-winding transformer is measured between two windings at a time. While the measurement is carried out at the first winding, the second winding is kept short circuited and the third winding is kept open circuited.

When considering the leakage inductance between the PV panel side and the grid side, the measurement is obtained by short circuiting the grid side winding and making the household side winding open circuit. Similarly, the leakage inductance of between other windings can also be measured. Taking the measured leakage inductances as

$\boldsymbol{L_{pv\text{-}g}}$ =measured inductance between PV side and Grid side
$\boldsymbol{L_{pv\text{-}h}}$=measured inductance between PV side and Household side
$\boldsymbol{L_{g\text{-}h}}$=measured inductance between Grid side and Household side

The leakage inductance values required for the equivalent circuit given in Figure 6.2 can be calculated by equations (6.1.1) to (6.1.3) [35]

$$L_{pv} = \frac{1}{2}\left(L_{pv-g} + L_{pv-h} - L_{g-h}\right) \qquad (6.1.1)$$

$$L_{g} = \frac{1}{2}\left(L_{pv-g} + L_{g-h} - L_{pv-h}\right) \qquad (6.1.2)$$

$$L_{h} = \frac{1}{2}\left(L_{pv-h} + L_{g-h} - L_{pv-g}\right) \qquad (6.1.3)$$

The resistance parameters required for the equivalent circuit can be easily measured using a DC resistance meter.

6.1.2 Conversion from T model to Π model

In order to develop a mathematical model for the HF transformer, Kirchhoff's current law (KCL) and Kirchhoff's voltage law laws (KVL) were used to derive the currents associated with the HF transformer. Once the magnetization parameters were ignored from the equivalent circuit shown in Figure 6.2, the impedances can be represented in a T model. As applying KVL and KCL for the T model is complex, the T model was converted to a Π model equivalent circuit. The Π model representation is given in Figure 6.3.

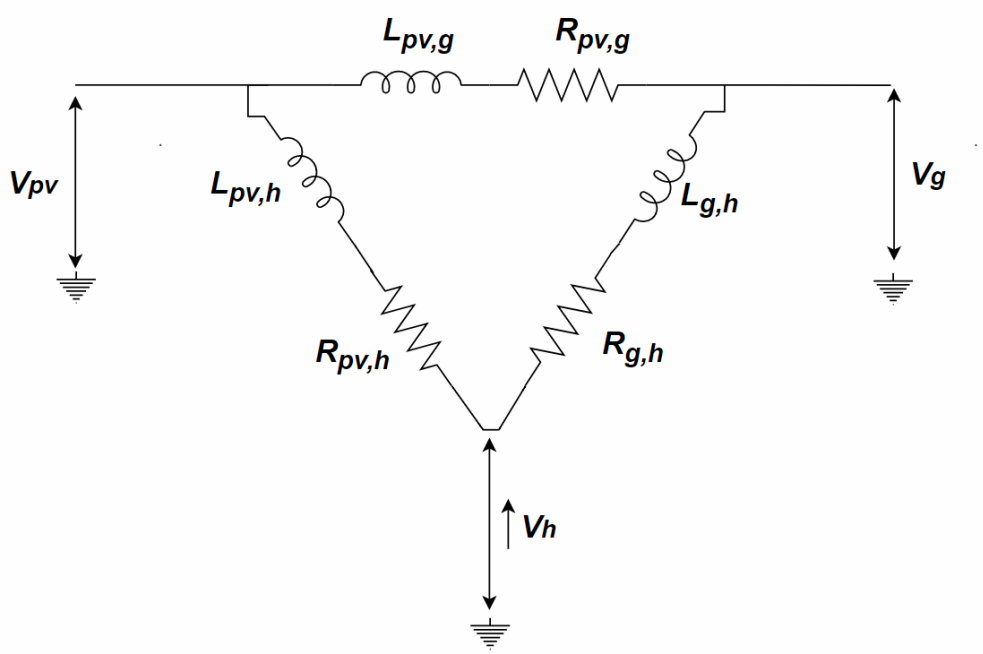

Figure 6.3: Π equivalent circuit of the three-winding transformer

Considering the PV panel side and the grid side. The relevant impedances in the Π model can be derived by equation (6.1.4)

$$Z_{pv,g} = \frac{Z_{pv}.Z_g + Z_{pv}.Z_h + Z_h.Z_g}{Z_h} \qquad (6.1.4)$$

If the impedance is given by Z, the relationship between the leakage inductance and the resistance can be given by equation (6.1.5)

$$Z = R + j\omega L \qquad (6.1.5)$$

substituting Z from equation (6.1.5) to equation (6.1.4) gives

$$R_{pv,g} + j\omega L_{pv,g}$$

$$= \frac{(R_{pv} + j\omega L_{pv}).(R_g + j\omega L_g) + (R_{pv} + j\omega L_{pv}).(R_h + j\omega L_h) + (R_h + j\omega L_h).(R_g + j\omega L_g)}{(R_h + j\omega L_h)}$$

By simplifying and separating the real and imaginary components, the inductance and resistance can be given by equations (6.1.6) and (6.1.7)

$$R_{pv,g} = \frac{(R_{pv}R_g + R_{pv}R_h + R_{pv}R_g).R_h - R_h\omega^2(L_{pv}L_g + L_{pv}L_h + L_hL_{pv})}{(R_h^2 + \omega^2 L_h^2)}$$
$$+\frac{\omega L_h(R_{pv}L_g + R_gL_{pv} + R_{pv}L_h + R_hL_{pv} + R_hL_g + R_gL_h)}{(R_h^2 + \omega^2 L_h^2)} \quad (6.1.6)$$

$$L_{pv,g} = \frac{-L_h(R_{pv}R_g + R_{pv}R_h + R_{pv}R_g) + L_h\omega^2(L_{pv}L_g + L_{pv}L_h + L_hL_{pv})}{(R_h^2 + \omega^2 L_h^2)}$$
$$+\frac{R_h(R_{pv}L_g + R_gL_{pv} + R_{pv}L_h + R_hL_{pv} + R_hL_g + R_gL_h)}{(R_h^2 + \omega^2 L_h^2)} \quad (6.1.7)$$

Similarly $\boldsymbol{L_{pv,h}}$, $\boldsymbol{R_{pv,h}}$ $\boldsymbol{L_{g,h}}$, and $\boldsymbol{R_{g,h}}$ can also be calculated.

Each port of the high frequency transformer is connected to a full bridge converter. Therefore, each port was represented with a voltage source in order to apply Kirchhoff's voltage law (KVL).

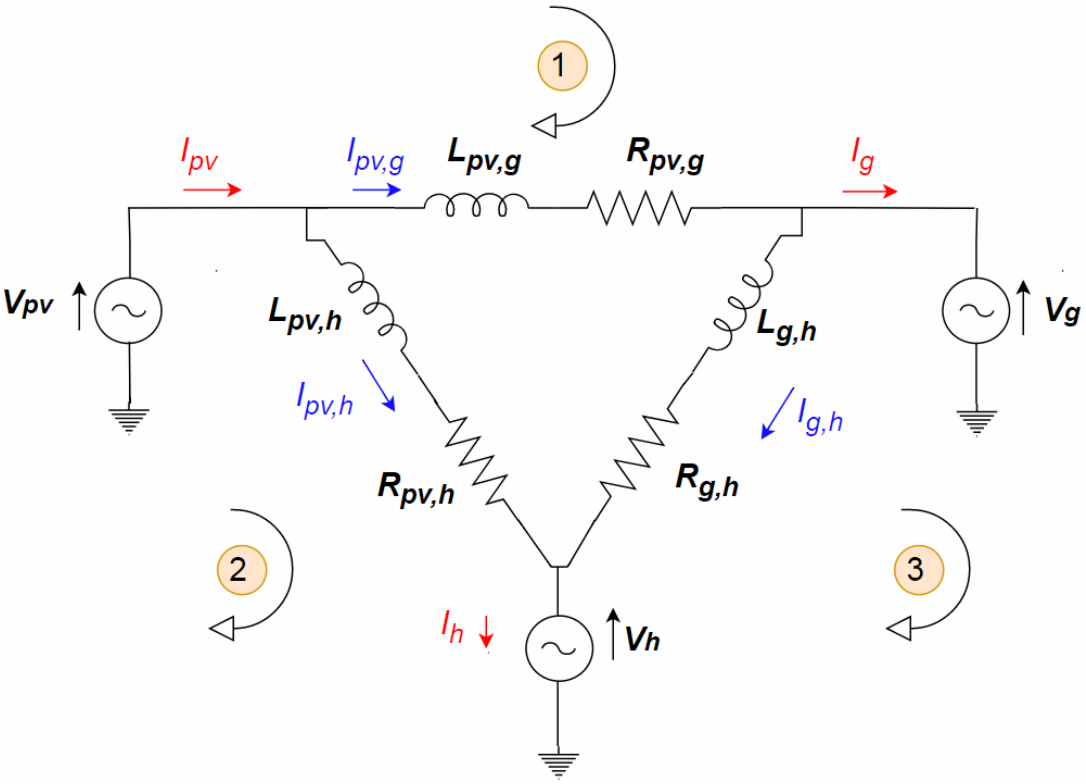

Figure 6.4: Π model currents and voltages

The resultant Π model is shown in Figure 6.4 with the relevant voltage sources and currents. KVL was used to determine the currents through the Π model.

Using KVL to loop 1,

$$V_g(t) - V_{pv}(t) + I_{pv,g}R_{pv,g} + L_{pv,g}\frac{dI_{pv,g}}{dt} = 0$$

$$V_{pv}(t) - V_g(t) = I_{pv,g}R_{pv,g} + L_{pv,g}\frac{dI_{pv,g}}{dt} \qquad (6.1.8)$$

For loop 2

$$V_{pv}(t) - V_h(t) - I_{pv,h}R_{pv,h} - L_{pv,h}\frac{dI_{pv,h}}{dt} = 0$$

$$V_{pv}(t) - V_h(t) = I_{pv,h}R_{pv,h} + L_{pv,h}\frac{dI_{pv,h}}{dt} \qquad (6.1.9)$$

For loop 3

$$V_h(t) - V_g(t) + I_{g,h}R_{g,h} + L_{g,h}\frac{dI_{g,h}}{dt} = 0$$

$$V_g(t) - V_h(t) = I_{g,h}R_{g,h} + L_{g,h}\frac{dI_{g,h}}{dt} \qquad (6.1.10)$$

The equations (6.1.8) to (6.1.10) give the relationship between the currents and the voltages of the three-winding high frequency transformer Π model.

6.2 Switching Function

The four switching devices of the bridge generate a bipolar square wave with a duty ratio of 50%. The phase shift between the complementary pair is maintained at 180º to generate the bipolar square waveform. The discrete function of this square waveform can be written by equation (6.2.1)

$$S(t)=\begin{Bmatrix}1 & 0\le t<\pi\\ -1 & \pi\le t<2\pi\end{Bmatrix} \qquad (6.2.1)$$

This shows that ***S(t)*** is a periodic square wave function with a period of 2π. In order to represent this discrete function in terms of continuous sinusoidal terms, ***S(t)*** can be approximated using a Fourier series shown in equation (6.2.2).

$$S(t)=\frac{a_0}{2}+\sum_{n=1}^{\infty}a_n\cos\left(\frac{2\pi nt}{T}\right)+\sum_{n=1}^{\infty}b_n\sin\left(\frac{2\pi nt}{T}\right) \qquad (6.2.2)$$

where

$$a_n=\frac{2}{T}\int_0^T S(t)\cos\left(\frac{2\pi nt}{T}\right)dt$$

$$b_n=\frac{2}{T}\int_0^T S(t)\sin\left(\frac{2\pi nt}{T}\right)dt$$

As the period ***T*** taken is ***2π***, substituting the ***S(t)*** function makes a_0 and a_n terms equals to zero, giving

$$b_n=\frac{1}{\pi}\int_0^{\pi}\sin(nt)\,dt-\frac{1}{\pi}\int_0^{\pi}\sin(nt)\,dt$$

$$=\frac{2}{n\pi}\left(1-\cos(n\pi)\right)$$

$$=\frac{4}{n\pi}\ \ (for\ n=1,3,5....)$$

In order to satisfy the function for all values of ***n***, ***S(t)*** can be written as shown in equation (6.2.3)

$$S(t) = \frac{4}{\pi}\sum_{n=0}^{N}\frac{1}{(2n+1)}\sin\left[(2n+1)\omega t\right] \qquad (6.2.3)$$

$$where \quad \omega = \frac{2\pi}{T}$$

where $\boldsymbol{\omega}$ is the frequency of the cyclic waveform, and $\boldsymbol{N}$ is the number of the Fourier terms considered and $\boldsymbol{T}$ is the period. As $\boldsymbol{n}$ approaches infinity the waveform in equation (6.2.3) resembles an ideal square waveform as shown in Figure 6.5.

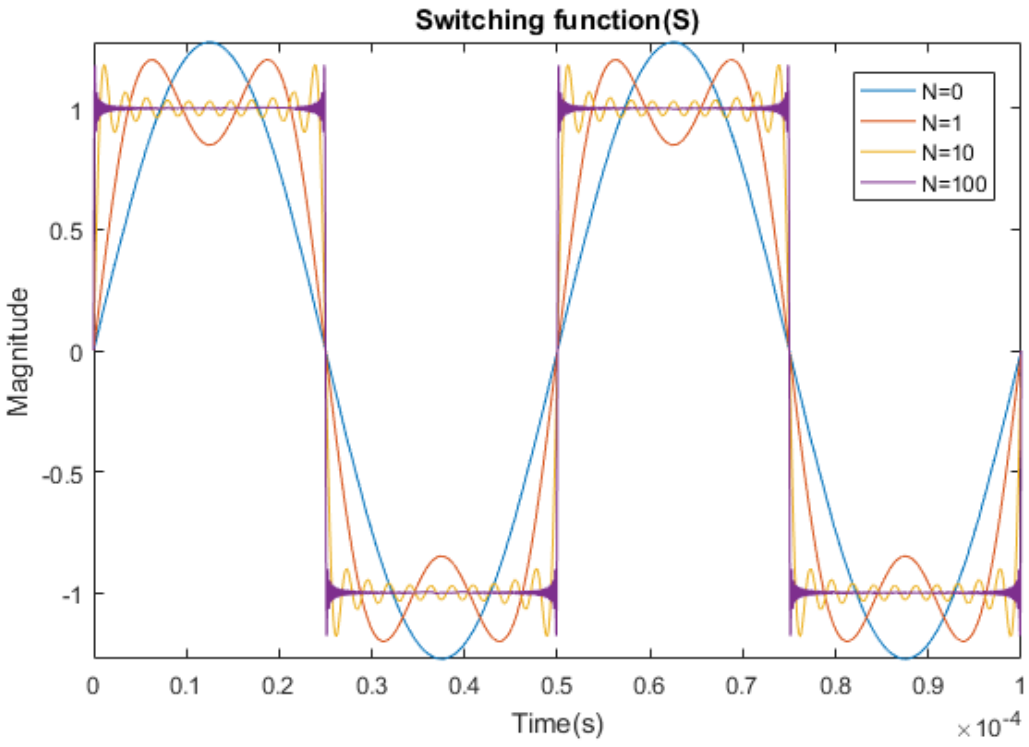

Figure 6.5: Fourier series representation of square wave as N increases

If the waveform is to be delayed by an angle of $\boldsymbol{\delta}$, the new switching function can be given by equation (6.2.4)

$$S_1(t) = \frac{4}{\pi}\sum_{n=0}^{N}\frac{1}{(2n+1)}\sin\left[(2n+1)(\omega t-\delta)\right] \qquad (6.2.4)$$

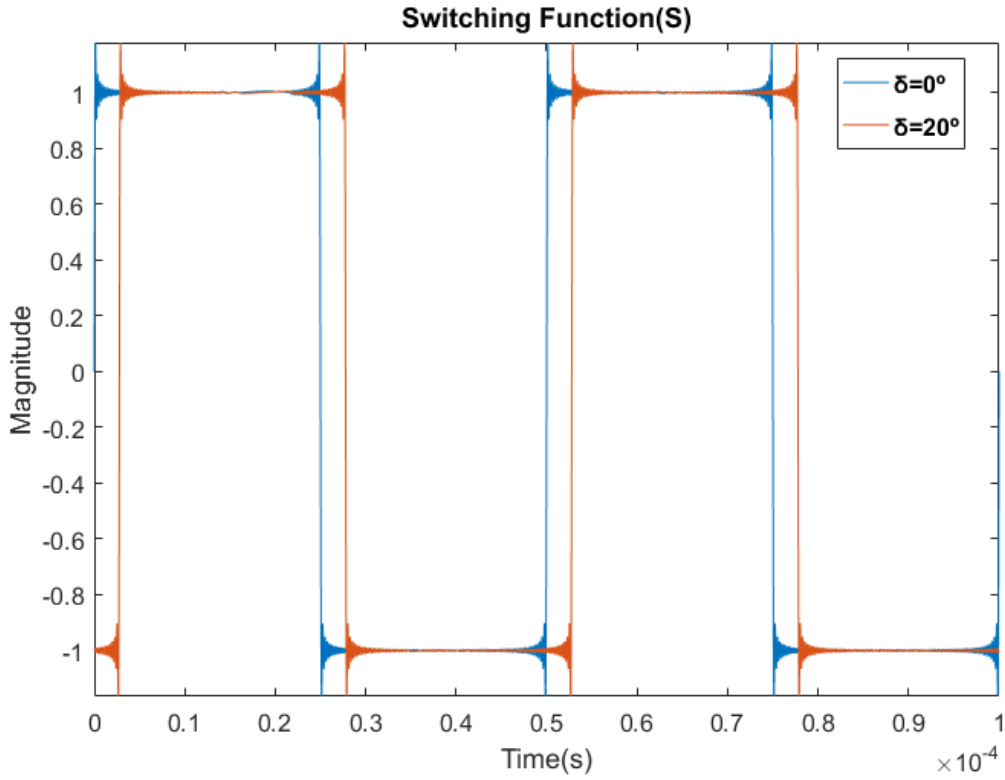

Figure 6.6: Delayed square waveform

The Figure 6.6 shows the shift of the waveform with an angle of 20 °. The switching functions of the converter at the three ports can be given by equations (6.2.5) to (6.2.7).

$$S_{pv}(t) = \frac{4}{\pi}\sum_{n=0}^{N}\frac{1}{(2n+1)}\sin\left[(2n+1)(\omega t - \delta_{pv})\right] \qquad (6.2.5)$$

$$S_{g}(t) = \frac{4}{\pi}\sum_{n=0}^{N}\frac{1}{(2n+1)}\sin\left[(2n+1)(\omega t - \delta_{g})\right] \qquad (6.2.6)$$

$$S_{h}(t) = \frac{4}{\pi}\sum_{n=0}^{N}\frac{1}{(2n+1)}\sin\left[(2n+1)(\omega t - \delta_{h})\right] \qquad (6.2.7)$$

Where $\boldsymbol{S_h}$, $\boldsymbol{S_{pv}}$ and $\boldsymbol{S_g}$ represent the switching functions and $\boldsymbol{\delta_h}$, $\boldsymbol{\delta_{pv}}$, $\boldsymbol{\delta_g}$ represent the phase shift of each bridge at the household, PV panel and the grid side converters.

6.3 HF Transformer Current Modelling

The DC voltage at the input of each converter is subjected to the switching function. The time varying voltage waveform of each converter can be given by equations (6.3.1) to (6.3.3).

$$V_{pv}(t) = V_{pv} S_{pv}(t) = \frac{4}{\pi} \sum_{n=0}^{N} \frac{V_{pv}}{(2n+1)} \sin\left[(2n+1)(\omega t - \delta_{pv})\right] \qquad (6.3.1)$$

$$V_{g}(t) = V_{g} S_{g}(t) = \frac{4}{\pi} \sum_{n=0}^{N} \frac{V_{g}}{(2n+1)} \sin\left[(2n+1)(\omega t - \delta_{g})\right] \qquad (6.3.2)$$

$$V_{h}(t) = V_{h} S_{h}(t) = \frac{4}{\pi} \sum_{n=0}^{N} \frac{V_{h}}{(2n+1)} \sin\left[(2n+1)(\omega t - \delta_{h})\right] \qquad (6.3.3)$$

By substituting $\boldsymbol{V_{pv}(t)}$ and $\boldsymbol{V_{g}(t)}$ to the equation (6.1.8) derived from KVL loop 1

$$I_{pv,g} R_{pv,g} + L_{pv,g} \frac{dI_{pv,g}}{dt} =$$
$$\frac{4}{\pi} \sum_{n=0}^{N} \frac{V_{pv}}{(2n+1)} \sin\left[(2n+1)(\omega t - \delta_{pv})\right] - \frac{4}{\pi} \sum_{n=0}^{N} \frac{V_{g}}{(2n+1)} \sin\left[(2n+1)(\omega t - \delta_{g})\right]$$

In order to simplify the expression for $\boldsymbol{I_{pv,g}}$, a single term of the Fourier series was considered.

$$I_{pv,g[2n+1]} R_{pv,g} + L_{pv,g} \frac{dI_{pv,g[2n+1]}}{dt}$$
$$= \frac{4}{\pi} \frac{1}{(2n+1)} \left\{ V_{pv} \sin\left[(2n+1)(\omega t - \delta_{pv})\right] - V_{g} \sin\left[(2n+1)(\omega t - \delta_{g})\right] \right\}$$

As the terms indicated are periodic sinusoidal terms, the derivative term can be represented using $\boldsymbol{j\omega}$ terms and the sinusoidal terms can be represented in phasor quantities.

$$I_{pv,g[2n+1]} R_{pv,g} + j[2n+1]\omega L_{pv,g} I_{pv,g[2n+1]}$$
$$= \frac{4}{\pi} \frac{1}{(2n+1)} \left\{ V_{pv} \angle -(2n+1)(\delta_{pv}) - V_{g} \angle -(2n+1)(\delta_{g}) \right\}$$

$$I_{pv,g[2n+1]} = \frac{\frac{4}{\pi}\frac{1}{(2n+1)}\left\{V_{pv}\angle -(2n+1)(\delta_{pv}) - V_g\angle -(2n+1)(\delta_g)\right\}}{R_{pv,g} + j[2n+1]\omega L_{pv,g}}$$

$$= \frac{\frac{4}{\pi}\frac{1}{(2n+1)}\left\{V_{pv}\angle -(2n+1)(\delta_{pv}) - V_g\angle -(2n+1)(\delta_g)\right\}}{\sqrt{(R_{pv,g})^2 + ([2n+1]\omega L_{pv,g})^2}\angle \tan^{-1}\left(\frac{[2n+1]\omega L_{pv,g}}{R_{pv,g}}\right)}$$

$$= \frac{4}{\pi}\frac{1}{(2n+1)}\left\{\frac{V_{pv}}{\left|Z_{pv,g}[n]\right|}\angle -(2n+1)(\delta_{pv}) - \phi_{pv,g}[n] - V_g\angle -(2n+1)(\delta_g) - \phi_{pv,g}[n]\right\}$$

Where

$$Z_{pv,g}[n] = \sqrt{(R_{pv,g})^2 + ([2n+1]\omega L_{pv,g})^2} \quad \textit{and} \quad \phi_{pv,g}[n] = \tan^{-1}\left(\frac{[2n+1]\omega L_{pv,g}}{R_{pv,g}}\right)$$

Summing the all terms of the Fourier series and converting back to the time domain gives $\boldsymbol{I_{pv,g}(t)}$ by equation (6.3.4)

$$I_{pv,g}(t) = \frac{4}{\pi}\sum_{n=0}^{N}\frac{1}{(2n+1)\left|Z_{pv,g}[n]\right|}\begin{Bmatrix} V_{pv}\sin\left[(2n+1)(\omega t - \delta_{pv}) - \phi_{pv,g}[n]\right] - \\ V_g\sin\left[(2n+1)(\omega t - \delta_g) - \phi_{pv,g}[n]\right] \end{Bmatrix} \qquad (6.3.4)$$

Similarly $\boldsymbol{I_{pv,h}}$ and $\boldsymbol{I_{g,h}}$ can be derived as shown by equations (6.3.5) and (6.3.6)

$$I_{pv,h}(t) = \sum_{n=0}^{N}\frac{4}{\pi}\frac{1}{(2n+1)\left|Z_{pv,h}[n]\right|}\begin{Bmatrix} V_{pv}\sin\left[(2n+1)(\omega t - \delta_{pv}) - \phi_{pv,h}[n]\right] - \\ V_h\sin\left[(2n+1)(\omega t - \delta_h) - \phi_{pv,h}[n]\right] \end{Bmatrix} \qquad (6.3.5)$$

$$I_{g,h}(t) = \frac{4}{\pi}\sum_{n=0}^{N}\frac{1}{(2n+1)\left|Z_{g,h}[n]\right|}\begin{Bmatrix} V_g\sin\left[(2n+1)(\omega t - \delta_g) - \phi_{g,h}[n]\right] - \\ V_h\sin\left[(2n+1)(\omega t - \delta_h) - \phi_{g,h}[n]\right] \end{Bmatrix} \qquad (6.3.6)$$

Applying the Kirchhoff's current law to the nodes in Figure 6.4 , the currents at the HF transformer ports at PV source, grid and household can be given by equations (6.3.7) to (6.3.9)

$$I_{pv} = -\left(I_{pv,g} + I_{pv,h}\right) \quad (6.3.7)$$

$$I_g = \left(I_{pv,g} - I_{g,h}\right) \quad (6.3.8)$$

$$I_h = \left(I_{pv,h} + I_{g,h}\right) \quad (6.3.9)$$

A MATLAB Simulink model was developed to validate the mathematical model discussed above. The developed Simulink model is shown in Figure 6.7.

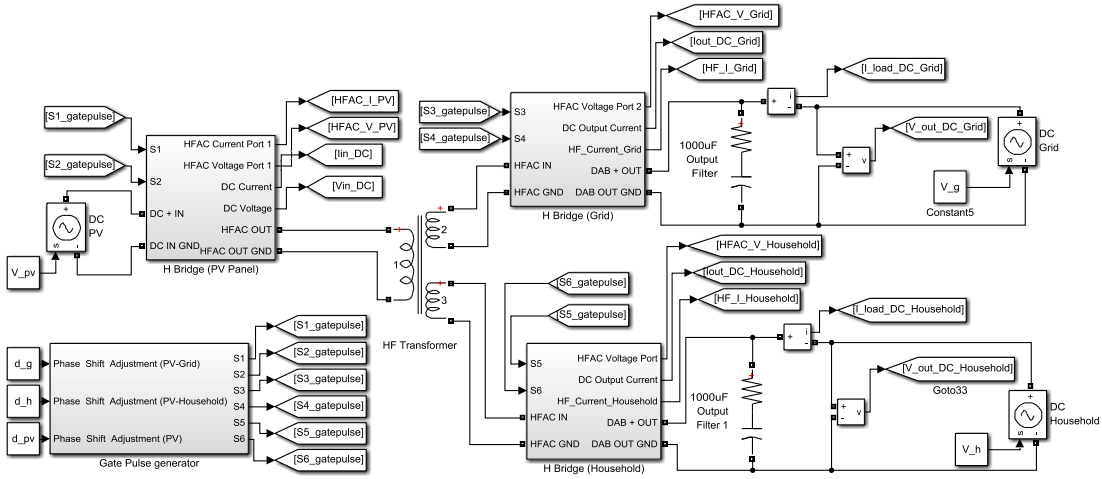

Figure 6.7: Simulink model of the TAB

The simulated currents and the mathematically modelled currents at the ports of the high frequency transformer are shown in Figure 6.8. The parameters used for the model and the simulation are shown in Table 6.1.

Table 6.1: Parameters used for comparing mathematical model with simulation

V_{pv} (PV array Voltage)	420 V
V_g (Grid side DC Voltage)	350 V
V_h (Household side DC Voltage)	350 V
Turns Ratios (N_{pv}:N_g:N_h)	1:1:1
L (Leakage inductance at each winding)	25 μH
R (Winding resistance of each winding)	10 mΩ
δ_{pv} (Phase shift at PV side bridge)	30º
δ_g (Phase shift at grid side bridge)	60º
δ_h (Phase shift at household side bridge)	70º
F (Switching Frequency)	20kHz
N (No of Fourier terms considered)	30

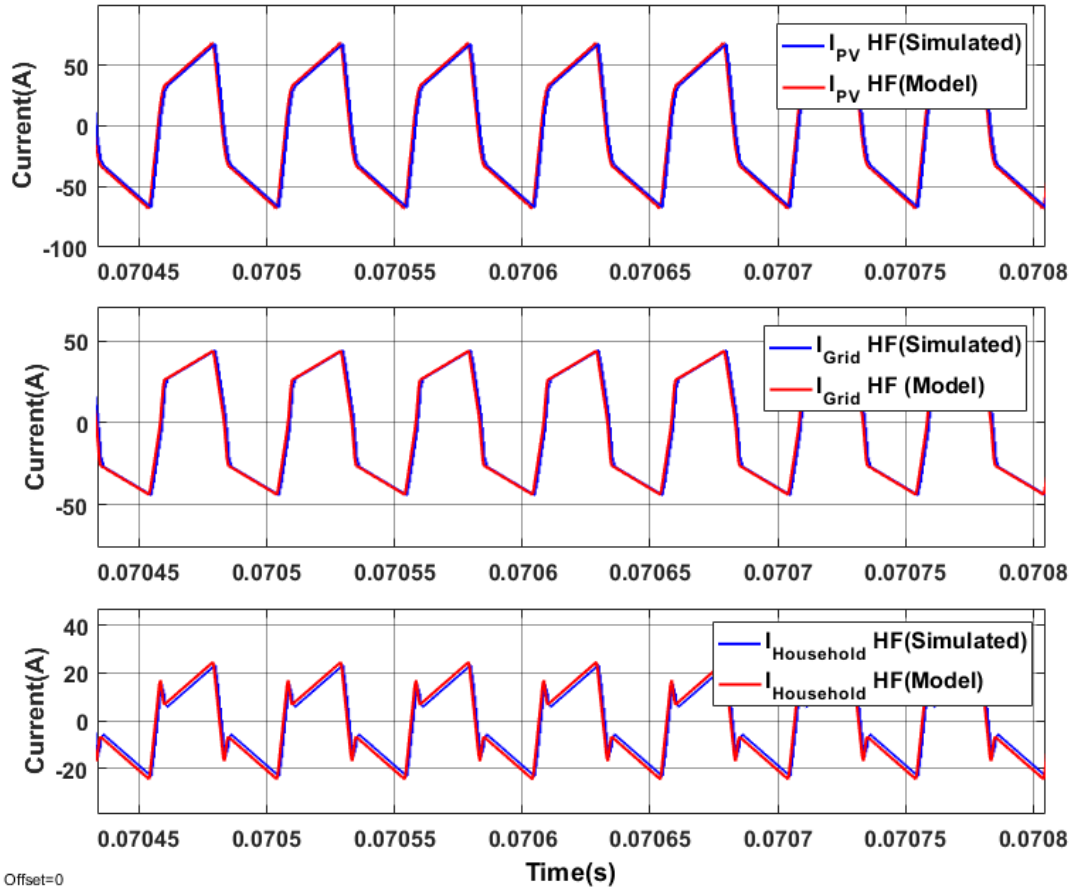

Figure 6.8: Mathematical model validation of transformer currents

Figure 6.8 indicate that the mathematical model accurately matches the steady state behavior of the currents at each port of the high frequency transformer.

6.4 Converter Output Current Modelling

The output current of the HF transformer is subjected the switching function of the converter. Multiplying HF transformer current with the switching function at household side gives the output current at the household side bridge by equation (6.4.1)

$$I_{h\_out} = I_h S_h \qquad (6.4.1)$$

where $\boldsymbol{S_h}$ is the switching function of the converter at the household side given by equation (6.2.7). Substituting $\boldsymbol{I_h}$ and $\boldsymbol{S_h}$ to equation (6.4.1) gives the converter output current by equation (6.4.2).

$$I_{h\_out} = \left\{ \frac{4}{\pi} \sum_{n=0}^{N} \frac{1}{(2n+1)} \left\{ \begin{array}{l} \frac{1}{|Z_{pv,h}[n]|} \left\{ \begin{array}{l} V_{pv} \sin\left[(2n+1)(\omega t - \delta_{pv}) - \phi_{pv,h}[n]\right] - \\ V_h \sin\left[(2n+1)(\omega t - \delta_h) - \phi_{pv,h}[n]\right] \end{array} \right\} \\ + \frac{1}{|Z_{g,h}[n]|} \left\{ \begin{array}{l} V_g \sin\left[(2n+1)(\omega t - \delta_g) - \phi_{g,h}[n]\right] - \\ V_h \sin\left[(2n+1)(\omega t - \delta_h) - \phi_{g,h}[n]\right] \end{array} \right\} \end{array} \right\} \times \right.$$

$$\left. \frac{4}{\pi} \sum_{m=0}^{M} \frac{1}{(2m+1)} \sin\left[(2m+1)(\omega t - \delta_h)\right] \right\} \tag{6.4.2}$$

M and ***m*** are the number of the Fourier terms considered in the household side converter switching function S_h. Similar to equation (6.4.2), the currents at the PV panel side and the household side converters can also be modeled. The simulated results and the modeled results are compared in Figure 6.9

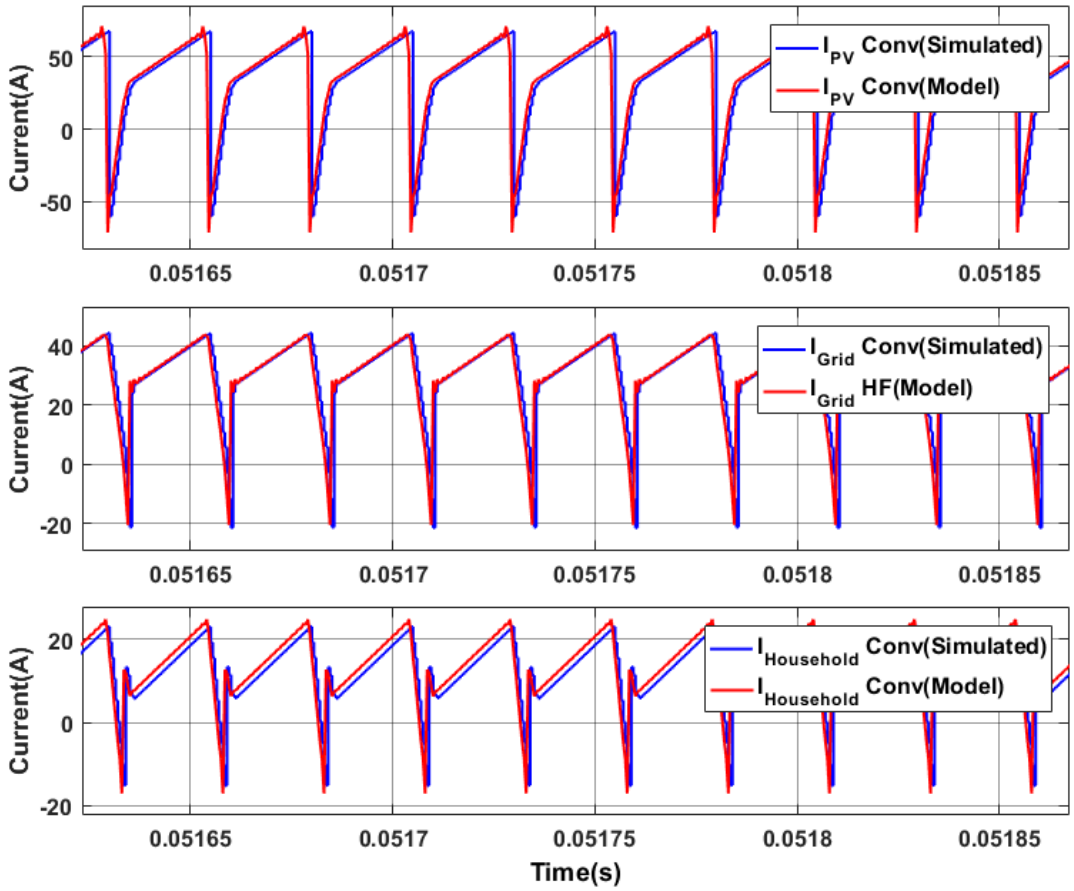

Figure 6.9: Mathematical model validation of converter output currents

6.5 Converter Output Voltage Modeling

The output current from the converter consists of two components as shown in Figure 6.1. They include the DC filter capacitor current and the DC bus current. Considering the household side connection, the relationship between the currents can be given by equation (6.5.1)

$$I_{h\_out} = I_C + I_{h\_DC} \tag{6.5.1}$$

A relationship between the capacitor current and the output voltage can be given by equation (6.5.2)

$$I_C = C_h \frac{dV_h}{dt} \tag{6.5.2}$$

Hence by substituting $\boldsymbol{I_c}$ to equation (6.5.1) gives $\boldsymbol{I_{h\_out}}$ by equation (6.5.3)

$$I_{h\_out} = C_h \frac{dV_h}{dt} + I_{h\_DC}$$

$$C_h \frac{dV_h}{dt} = I_{h\_out} - I_{h\_DC} \tag{6.5.3}$$

By substituting to $\boldsymbol{I_{h\_out}}$ a from equation (6.4.2), a relationship for the voltage across the capacitor can be given by equation (6.5.4)

$$\frac{dV_h}{dt} =$$

$$\left\{ \begin{array}{l} \dfrac{4}{C_h \pi} \displaystyle\sum_{n=0}^{N} \dfrac{1}{(2n+1)} \left\{ \begin{array}{l} \dfrac{1}{\left|Z_{pv,h}[n]\right|} \left\{ \begin{array}{l} V_{pv} \sin\left[(2n+1)(\omega t - \delta_{pv}) - \phi_{pv,h}[n]\right] - \\ \quad V_h \sin\left[(2n+1)(\omega t - \delta_h) - \phi_{pv,h}[n]\right] \end{array} \right\} \\ + \dfrac{1}{\left|Z_{g,h}[n]\right|} \left\{ \begin{array}{l} V_g \sin\left[(2n+1)(\omega t - \delta_g) - \phi_{g,h}[n]\right] - \\ \quad V_h \sin\left[(2n+1)(\omega t - \delta_h) - \phi_{g,h}[n]\right] \end{array} \right\} \end{array} \right\} \times \\ \qquad \dfrac{4}{\pi} \displaystyle\sum_{m=0}^{M} \dfrac{1}{(2m+1)} \sin\left[(2m+1)(\omega t - \delta_h)\right] \end{array} \right\} - I_{h\_DC} \tag{6.5.4}$$

The simulated and the modeled household side voltage waveforms are shown in Figure 6.10. The household side voltage source in Figure 6.7 was replaced with a load of 10Ω.

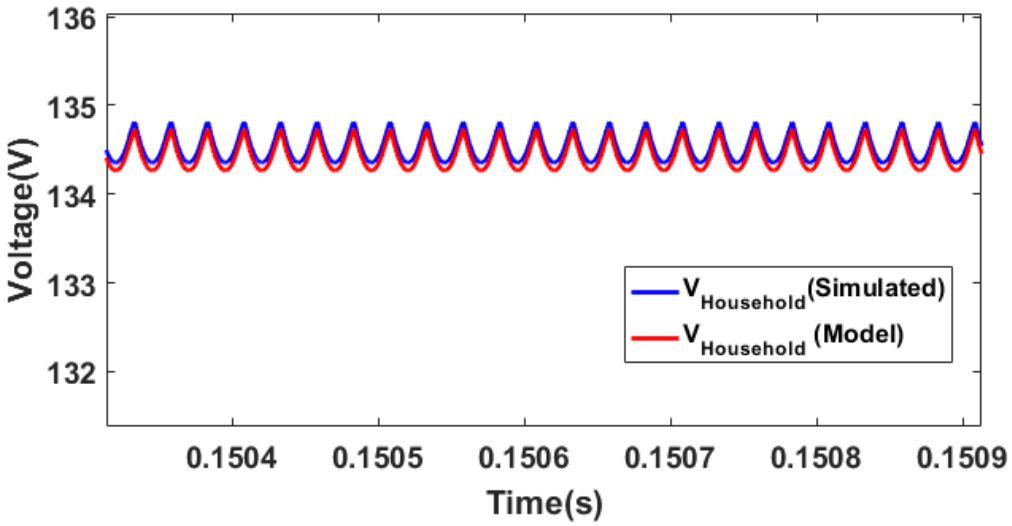

Figure 6.10: Mathematical model validation of DC bus voltage

The equation (6.5.4) contains multiplication of two Fourier series summation functions. The result shown in Figure 6.10 was computed using an ODE solver in MATLAB. However, it is difficult to arrange this equation in an analytical form with two series multiplication terms present. Therefore, by considering only the terms where ***n*=*m*** the higher order series multiplication terms were eliminated.

$$\frac{dV_h}{dt} =$$

$$\frac{4}{C_h \pi}\sum_{n=0}^{N}\frac{1}{(2n+1)^2}\left\{\begin{array}{l}\dfrac{1}{|Z_{pv,h}[n]|}\left\{\begin{array}{l}V_{pv}\sin\left[(2n+1)(\omega t-\delta_{pv})-\phi_{pv,h}[n]\right]\sin\left[(2n+1)(\omega t-\delta_h)\right]-\\ V_h\sin\left[(2n+1)(\omega t-\delta_h)-\phi_{pv,h}[n]\right]\sin\left[(2n+1)(\omega t-\delta_h)\right]\end{array}\right\}\\ +\dfrac{1}{|Z_{g,h}[n]|}\left\{\begin{array}{l}V_g\sin\left[(2n+1)(\omega t-\delta_g)-\phi_{g,h}[n]\right]\sin\left[(2n+1)(\omega t-\delta_h)\right]-\\ V_h\sin\left[(2n+1)(\omega t-\delta_h)-\phi_{g,h}[n]\right]\sin\left[(2n+1)(\omega t-\delta_h)\right]\end{array}\right\}\end{array}\right\}$$

$$-I_{h\_DC}$$

(6.5.5)

Using the trigonometric simplification of $2\sin A.\sin B = \cos(A-B) - \cos(A+B)$ the model can be re arranged as shown by equation (6.5.6)

$$\frac{dV_h}{dt} =$$

$$\left\{ \frac{4}{C_h \pi} \sum_{n=0}^{N} \frac{1}{(2n+1)} \left\{ \begin{array}{l} \dfrac{V_{pv}}{\left|Z_{pv,h}[n]\right|} \left\{ \begin{array}{l} \cos\left[(2n+1)(\delta_h - \delta_{pv}) - \phi_{pv,h}[n]\right] \\ -\cos\left[(2n+1)(2\omega t - \delta_h - \delta_{pv}) - \phi_{pv,h}[n]\right] \end{array} \right\} \\ -\dfrac{V_h}{\left|Z_{pv,h}[n]\right|} \left\{ \begin{array}{l} \cos\left[\phi_{pv,h}[n]\right] \\ -\cos\left[2(2n+1)(\omega t - \delta_h) - \phi_{pv,h}[n]\right] \end{array} \right\} \\ +\dfrac{V_g}{\left|Z_{g,h}[n]\right|} \left\{ \begin{array}{l} \cos\left[(2n+1)(\delta_h - \delta_g) - \phi_{g,h}[n]\right] \\ -\cos\left[(2n+1)(2\omega t - \delta_g - \delta_h) - \phi_{g,h}[n]\right] \end{array} \right\} \\ -\dfrac{V_h}{\left|Z_{g,h}[n]\right|} \left\{ \begin{array}{l} \cos\left[\phi_{g,h}[n]\right] \\ -\cos\left[2.(2n+1)(\omega t - \delta_h) - \phi_{g,h}[n]\right] \end{array} \right\} \end{array} \right\} \times \right\} - I_{h\_DC}$$

(6.5.6)

The solution of the equation (6.5.6) is a steady DC voltage. The time varying sinusoidal terms that include ***ωt*** terms of the equations are the components that contribute to the ripple of the output voltage. The only terms that contribute to the long-term DC output voltage are the time invariant sinusoidal terms. By eliminating the time varying sinusoidal terms, the equation can be simplified further in order to obtain an averaged simplified DC output waveform given by equation (6.5.7).

$$\frac{dV_h}{dt} = -\frac{I_{h\_DC}}{C_h}$$

$$\frac{8}{C_h \pi^2} \sum_{n=0}^{N} \frac{1}{(2n+1)^2} \left\{ \begin{array}{l} \dfrac{1}{\left|Z_{pv,h}[n]\right|} \left\{ V_{pv} \cos\left[(2n+1)(\delta_h - \delta_{pv}) - \phi_{pv,h}[n]\right] - V_h \cos\left[\phi_{pv,h}[n]\right] \right\} \\ -\dfrac{1}{\left|Z_{g,h}[n]\right|} \left\{ V_h \cos\left[\phi_{g,h}[n]\right] + V_g \cos\left[(2n+1)(\delta_h - \delta_g) - \phi_{g,h}[n]\right] \right\} \end{array} \right\}$$

(6.5.7)

By simplifying and rearranging equation (6.5.7), the output voltage at the household side can be given by equation (6.5.8)

$$\frac{dV_h}{dt} = -\frac{I_{h\_DC}}{C_h} + \frac{8}{C_h\pi^2}\sum_{n=0}^{N}\frac{1}{(2n+1)^2}\left\{\begin{array}{l} -V_h\left\{\dfrac{\cos\left[\phi_{g,h}[n]\right]}{\left|Z_{g,h}[n]\right|} + \dfrac{\cos\left[\phi_{pv,h}[n]\right]}{\left|Z_{pv,h}[n]\right|}\right\} \\ +V_g\left\{\dfrac{\cos\left[(2n+1)(\delta_h-\delta_g)-\phi_{g,h}[n]\right]}{\left|Z_{g,h}[n]\right|}\right\} \\ +V_{pv}\left\{\dfrac{\cos\left[(2n+1)(\delta_h-\delta_{pv})-\phi_{pv,h}[n]\right]}{\left|Z_{pv,h}[n]\right|}\right\} \end{array}\right\} \tag{6.5.8}$$

Similarly, following the same sequence from equation (6.5.1), the output voltage at the grid side can be derived and given by equation (6.5.9).

$$\frac{dV_g}{dt} = -\frac{I_{g\_DC}}{C_g} + \frac{8}{C_g\pi^2}\sum_{n=0}^{N}\frac{1}{(2n+1)^2}\left\{\begin{array}{l} -V_g\left\{\dfrac{\cos\left[\phi_{g,h}[n]\right]}{\left|Z_{g,h}[n]\right|} + \dfrac{\cos\left[\phi_{pv,g}[n]\right]}{\left|Z_{pv,g}[n]\right|}\right\} \\ +V_h\left\{\dfrac{\cos\left[(2n+1)(\delta_g-\delta_h)-\phi_{g,h}[n]\right]}{\left|Z_{g,h}[n]\right|}\right\} \\ +V_{pv}\left\{\dfrac{\cos\left[(2n+1)(\delta_g-\delta_{pv})-\phi_{pv,g}[n]\right]}{\left|Z_{pv,g}[n]\right|}\right\} \end{array}\right\} \tag{6.5.9}$$

In order to validate the above simplification, this simplified model was compared with the detailed model given by equation (6.5.4) in MATLAB. The Figure 6.11 shows the variation of the household side output voltage when the phase shift $\boldsymbol{\delta_h}$ was varied by of 5 º. It shows that the simplified model accurately follows the detailed model without a deviation.

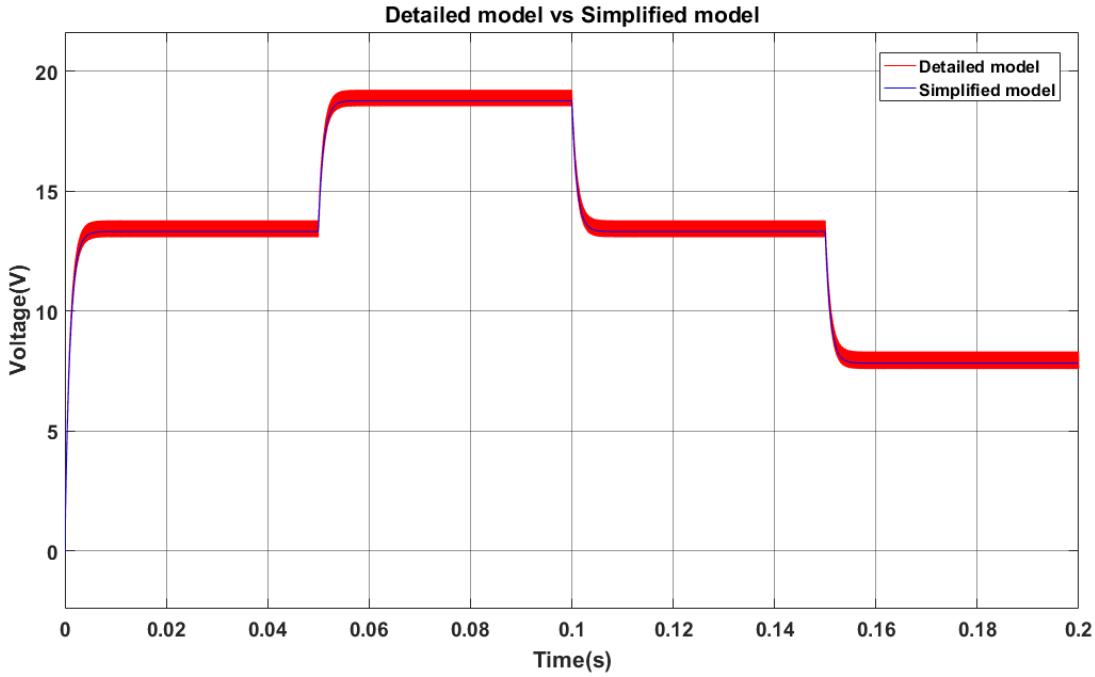

Figure 6.11: Comparison of detailed and simplified model for output voltage

6.6 Output Voltage Transfer Functions

The plot in Figure 6.11 shows that the output voltage varies with the phase shift. A transfer function that gives the relationship between the voltage and the phase shift is required derive a controller to maintain the output voltage while adjusting the phase shift to deliver the required amount of power.

6.6.1 Linearization

The models mentioned in equation (6.5.8) and (6.5.9) consist of multiple sinusoidal terms of the Fourier series that include the phase shift. Deriving a controller configuration for this is complex and impractical. Therefore, it was simplified by linearizing the equation around a given set point. This was done using the Taylor series expansion.

A derivative function $f(x,y)$ can be linearized around a steady state operating point x_s,y_s using the Taylor series expansion shown in equation (6.6.1). The resulting higher order terms above the first derivative term can be neglected.

$$\frac{d\left(f(x,y)-f(x_s,y_s)\right)}{dt}=(x-x_s)\frac{\partial f}{\partial x}\bigg|_{x_s,y_s}+(y-y_s)\frac{\partial f}{\partial y}\bigg|_{x_s,y_s}+.....$$

$$\frac{d\left(\Delta f\right)}{dt}=(\Delta x)\frac{\partial f}{\partial x}\bigg|_{x_s,y_s}+(\Delta y)\frac{\partial f}{\partial y}\bigg|_{x_s,y_s}+..... \qquad (6.6.1)$$

This expansion was used on the models shown in equation (6.5.8) and (6.5.9), to obtain a linearized model for the output voltage. Since the only controllable variables are the output voltage and the phase shift for the relevant bridge, the other variables were fixed in order to obtain the linearized model. The linearized models for the grid voltage and household voltage are given by equations (6.6.2) and (6.6.3)

$$\frac{d\Delta V_h}{dt}=f(V_h,\delta_h)$$

$$=\frac{8}{C_h\pi^2}\sum_{n=0}^{N}\frac{1}{(2n+1)^2}\left\{\begin{array}{l}-\left\{\dfrac{\cos\left[\phi_{g,h}[n]\right]}{\left|Z_{g,h}[n]\right|}+\dfrac{\cos\left[\phi_{pv,h}[n]\right]}{\left|Z_{pv,h}[n]\right|}\right\}\Delta V_h \\ -\left\{(2n+1)\left\{\begin{array}{l}V_{g0}\dfrac{\sin\left[(2n+1)(\delta_{h0}-\delta_{g0})-\phi_{g,h}[n]\right]}{\left|Z_{g,h}[n]\right|}+ \\ V_{pv}\dfrac{\sin\left[(2n+1)(\delta_{h0}-\delta_{pv0})-\phi_{pv,h}[n]\right]}{\left|Z_{pv,h}[n]\right|}\end{array}\right\}\Delta\delta_h\right\}\end{array}\right\} \qquad (6.6.2)$$

$$\frac{d\Delta V_g}{dt}=f(V_g,\delta_g)$$

$$=\frac{8}{C_g\pi^2}\sum_{n=0}^{N}\frac{1}{(2n+1)^2}\left\{\begin{array}{l}-\left\{\dfrac{\cos\left[\phi_{g,h}[n]\right]}{\left|Z_{g,h}[n]\right|}+\dfrac{\cos\left[\phi_{pv,h}[n]\right]}{\left|Z_{pv,h}[n]\right|}\right\}\Delta V_g \\ -\left\{(2n+1)\left\{\begin{array}{l}V_{h0}\dfrac{\sin\left[(2n+1)(\delta_{g0}-\delta_{h0})-\phi_{g,h}[n]\right]}{\left|Z_{g,h}[n]\right|}+ \\ V_{pv}\dfrac{\sin\left[(2n+1)(\delta_{g0}-\delta_{pv0})-\phi_{pv,h}[n]\right]}{\left|Z_{pv,h}[n]\right|}\end{array}\right\}\Delta\delta_g\right\}\end{array}\right\} \qquad (6.6.3)$$

6.6.2 Transfer functions for DC bus output voltages

In order to derive a controller configuration, the equations (6.6.2) and (6.6.3) needs to be converted to Laplace domain to obtain their respective transfer functions. The equations (6.6.4) and (6.6.5) show the transfer functions for the grid side and household side DC bus voltages.

For the grid side DC bus, the transfer function can be given by equation (6.6.4)

$$s\Delta V(s) = A_g \Delta V(s) + B_g \Delta\delta(s) \tag{6.6.4}$$

$$\frac{\Delta V(s)}{\Delta\delta(s)} = \frac{B_g}{s - A_g}$$

where

$$A_g = -\frac{8}{C_g \pi^2} \sum_{n=0}^{N} \frac{1}{(2n+1)^2} \left\{ \frac{\cos\left[\phi_{g,h}[n]\right]}{\left|Z_{g,h}[n]\right|} + \frac{\cos\left[\phi_{pv,h}[n]\right]}{\left|Z_{pv,h}[n]\right|} \right\}$$

$$B_g = -\frac{8}{C_g \pi^2} \sum_{n=0}^{N} \frac{1}{(2n+1)} \left\{ \begin{array}{l} V_{h0} \dfrac{\sin\left[(2n+1)(\delta_{g0} - \delta_{h0}) - \phi_{g,h}[n]\right]}{\left|Z_{g,h}[n]\right|} + \\ V_{pv} \dfrac{\sin\left[(2n+1)(\delta_{g0} - \delta_{pv0}) - \phi_{pv,h}[n]\right]}{\left|Z_{pv,h}[n]\right|} \end{array} \right\}$$

Similarly, for the Household side DC bus, the transfer function for the voltage can be given by equation (6.6.5)

$$s\Delta V(s) = A_h \Delta V(s) + B_h \Delta\delta(s) \tag{6.6.5}$$

$$\frac{\Delta V(s)}{\Delta\delta(s)} = \frac{B_h}{s - A_h}$$

where

$$A_h = -\frac{8}{C_h \pi^2} \sum_{n=0}^{N} \frac{1}{(2n+1)^2} \left\{ \frac{\cos\left[\phi_{g,h}[n]\right]}{\left|Z_{g,h}[n]\right|} + \frac{\cos\left[\phi_{pv,h}[n]\right]}{\left|Z_{pv,h}[n]\right|} \right\}$$

$$B_h = -\frac{8}{C_h \pi^2} \sum_{n=0}^{N} \frac{1}{(2n+1)} \left\{ \begin{array}{l} V_{g0} \dfrac{\sin\left[(2n+1)(\delta_{h0} - \delta_{g0}) - \phi_{g,h}[n]\right]}{\left|Z_{g,h}[n]\right|} + \\ V_{pv} \dfrac{\sin\left[(2n+1)(\delta_{h0} - \delta_{pv0}) - \phi_{pv,h}[n]\right]}{\left|Z_{pv,h}[n]\right|} \end{array} \right\}$$

Both of the transfer functions shown are first order transfer functions similar to the output voltage transfer functions of the dual active bridge described in chapter 5. A PI controller configuration can be derived for these two transfer functions. The controller tuning and the parameter selection for the tri active bridge are presented in the next chapter. The MATLAB codes developed for validating the mathematical models in this chapter are given in Appendix E

7 TRI ACTIVE BRIDGE BASED PV INVERTER

This chapter includes the controller configuration and the gate pulse generation circuit of the TAB based on the mathematical models derived in chapter 6.

7.1 Power Flow

The TAB in this application operates in three main power flow scenarios

(i) The first is where the PV array generates the power and feeds to the grid when there is no load at the household.

(ii) The second scenario occurs when the household load is active. The power output to the grid reduces, redirecting the power from the PV array to the household.

(iii) Third scenario occurs as the household load increases above the generated PV output. The grid side inverter draws the abundant power from the grid through the HF transformer to facilitate the household load. The maximum power flow from the PV port does not exceed 3 kW while the power flow from Grid side converter to the Household side reaches up to 7 kW.

In all cases, the maximum power flow out of each port remains below 7 kW. The power flow scenarios are shown in Figure 7.1.

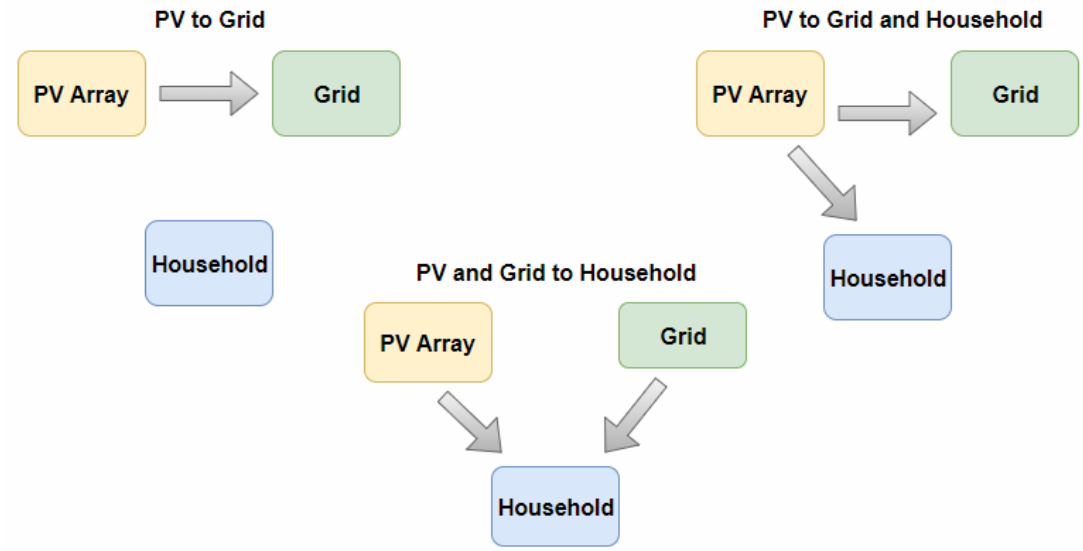

Figure 7.1: Power flow scenarios of the Tri active bridge

The power flow between PV and grid side ports of the TAB can be given by the equation 7.1.1, which is similar to the power flow equation of the DAB. The leakage inductance considered is the sum of the leakage inductances of the two respective windings concerned [46] . The equation is similar for the power flow between other ports.

$$P_{pv,g} = \frac{V_g V_{pv}}{2\pi f (L_{pv} + L_g)} \delta_{pv,g} \left(1 - \frac{|\delta_{pv,g}|}{\pi} \right) \qquad (7.1.1)$$

Where

$\boldsymbol{V_{pv}}$ = PV Panel side DC voltage

$\boldsymbol{V_g}$ =Grid Side DC voltage

$\boldsymbol{\delta_{pv,g}}$ =Phase shift between PV panel side and grid side bridges

$\boldsymbol{f}$=Switching frequency

$\boldsymbol{L_{pv}}$= PV side winding leakage inductance

$\boldsymbol{L_g}$= Grid side winding leakage inductance

7.2 Controller Configuration

Since the HF transformer used for this design has equal number of turns in each winding, the leakage inductance and resistance at each port can be considered equal as shown in equation (7.2.1) and (7.2.2).

$$L \approx L_g \approx L_h \approx L_{pv} \qquad (7.2.1)$$

$$R \approx R_g \approx R_h \approx R_{pv} \qquad (7.2.2)$$

Using the equations (6.1.6) and (6.1.7) in chapter 6, the leakage inductance and resistance becomes 3 times the leakage inductance and resistance of each winding as given by equations (7.2.3) and (7.2.4).

$$L_{\Pi} = 3L \qquad (7.2.3)$$

$$R_{\Pi} = 3R \qquad (7.2.4)$$

In order to have a power flow of 7 kW, the optimal leakage inductance was taken as 50 μH in chapter 5 for the dual active bridge. As the power flow equation is the same, the leakage inductance at each winding of the three winding HF transformer in this application was taken as 25 μH.

This gives the Π equivalent leakage inductance as 75 μH. Similarly, the Π equivalent winding resistances can be calculated as 30 mΩ. The impedance and the impedance angle parameters of the transfer functions can be taken as equal as shown by equation (7.2.5) and (7.2.6)

$$Z_{g,h} \approx Z_{pv,h} \approx Z_{pv,g} \qquad (7.2.5)$$

and

$$\phi_{g,h} \approx \phi_{pv,h} \approx \phi_{pv,g} \qquad (7.2.6)$$

The parameters used to calculate the plant transfer functions for the grid and household side voltage converters are given in Table 7.1.

Table 7.1: Parameters used for tuning the TAB Voltage controllers

Switching frequency (f)	20kHz
Π equivalent leakage inductance ($L_{pv,g}$=$L_{pv,h}$=$L_{g,h}$)	75μH
Π equivalent winding resistance ($R_{pv,g}$ =$R_{pv,h}$ =$R_{g,h}$)	30mΩ
Transformer Ratios (N_{pv}:N_g:N_h)	1:1:1
Initial points (δ_g, δ_g)	10.6 º
PV Panel side phase shift (δ_{pv})	0 º
Number of Fourier terms (N)	10
Output DC link capacitance (C_g)	1000μF
PV Panel output voltage (V_{pv})	390V
Grid and Household side DC Voltages (V_g, V_h)	350V

Substituting these parameters to equation (6.6.4), the grid side voltage transfer function can be given by equation (7.2.7).

$$\frac{\Delta V(s)}{\Delta \delta(s)} = \frac{B_g}{s - A_g} = \frac{6.906 \times 10^4}{s + 0.556} \qquad (7.2.7)$$

Similar to the DAB in chapter 5, the PI gain values were tuned using the Simulink PID tuner.

$K_p = 0.1594$

$K_I = 6629$

The open loop and closed loop transfer functions can be given by equations (7.2.8) and (7.2.9)

$$F_g(s) = \frac{9584.7(s+6629)}{s(s+0.556)} \tag{7.2.8}$$

$$R_g(s) = \frac{G_p(s)G_c(s)}{1+G_p(s)G_c(s)} = \frac{9584.7(s+6629)}{(s^2+9585s+6.354\times10^7)} \tag{7.2.9}$$

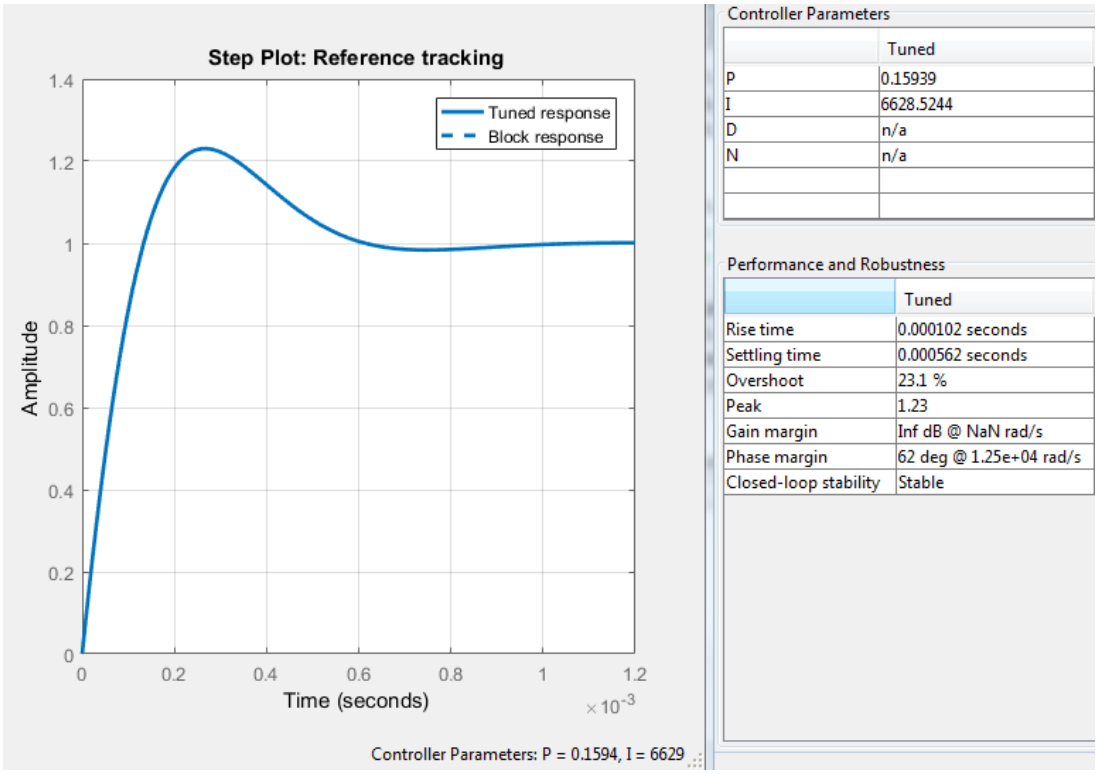

Figure 7.2: Controller tuning of the TAB

The controller was tuned using Simulink PID tuner to have the same response as the dual active bridge, with similar characteristics on overshoot, rise time and settling time. The tuned step response is shown in Figure 7.2

The response of the dual active bridge voltage controller with varying input voltage conditions were shown in chapter 5. It showed that the input voltage variation had a no significant impact on the stability of the system. In this model however, there is a phase shift parameter that varies with the power output at the household side bridge. The variation of the parameter $\boldsymbol{B_g}$ with the initial phase shift at the household side and grid side is shown in Figure 7.3.

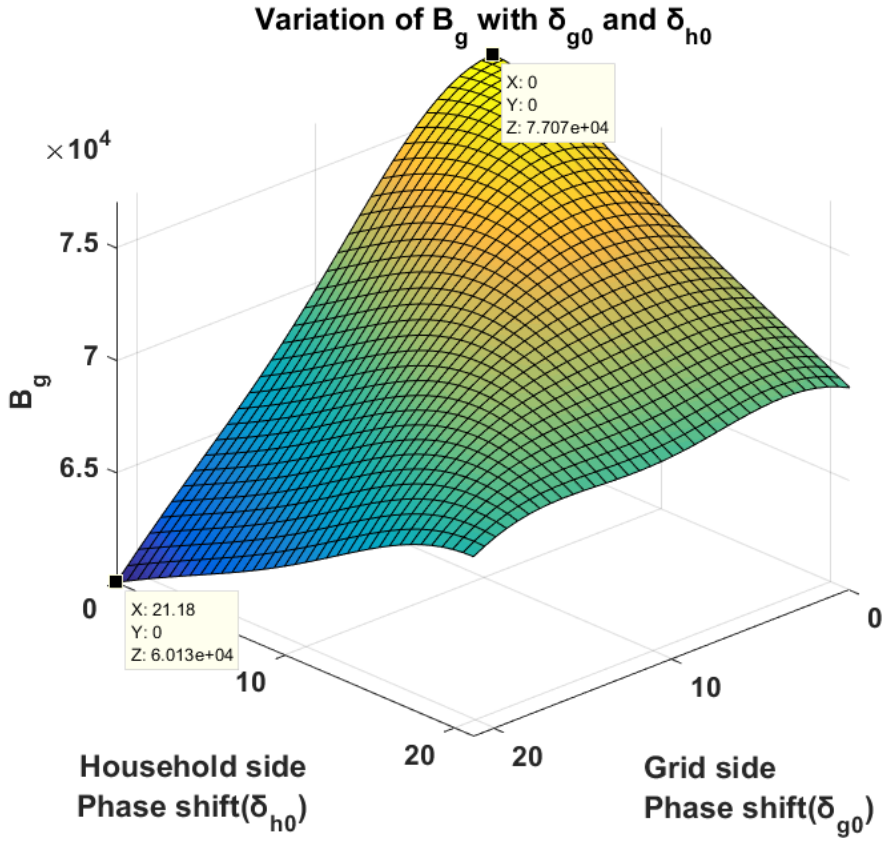

Figure 7.3: Surface plot of $\boldsymbol{B_g}$ for the TAB

The surface plot shows that the maximum value of $\boldsymbol{B_g}$ is present when both the initial phase shifts are set to zero, and the minimum occurs when the grid side phase shift is set to maximum and the household side phase shift is set to minimum. With the maximum and minimum values of $\boldsymbol{B_g}$, as 6.013×10^4 and 7.707×10^4 the step of the responses and the pole zero plot of the grid side controller are shown in Figure 7.4. The plots indicate that the variation of the response is minimal and that the controller is still stable irrespective of the initial phase shift at the household and grid sides.

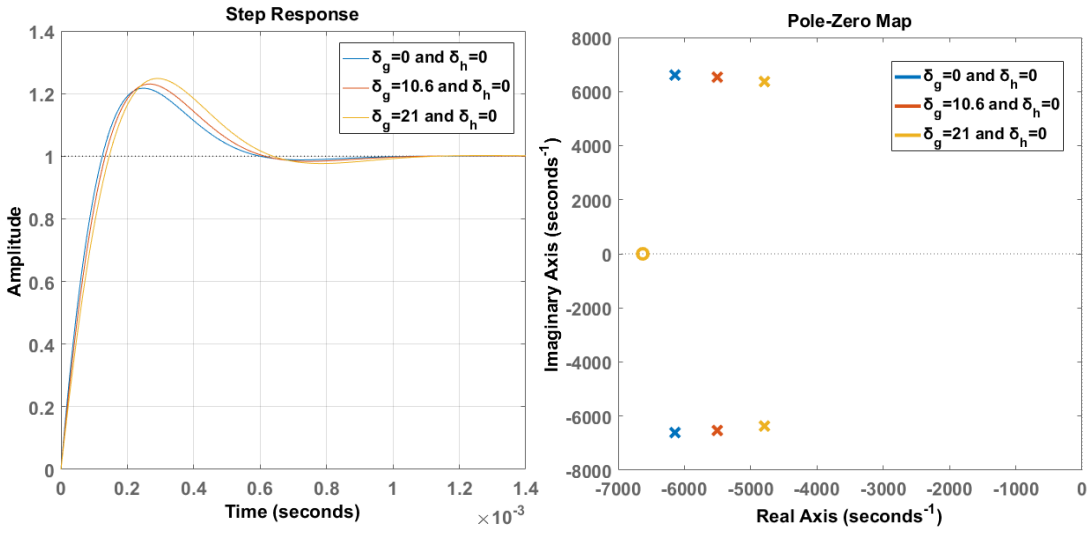

Figure 7.4: Pole zero plots and step responses for varying $\boldsymbol{B_g}$

Since the impedance parameters are equal, the transfer functions for both the grid and household side become equivalent. Therefore, the same controller configuration can be used for both household and the grid side converters. Similar to the DAB controller, this controller configuration requires a different set of PI gain values to control the voltage for large voltage variations at the DC bus. The controller configurations are shown in Figure 7.5.

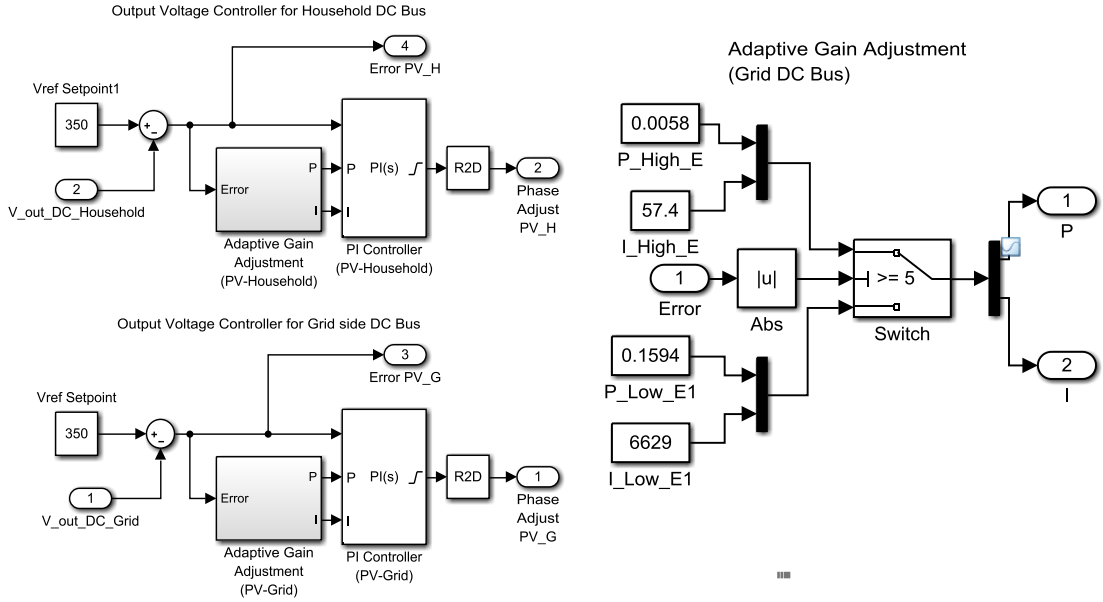

Figure 7.5: Output voltage controllers for the TAB

The controller outputs were set to have a saturation limiter to operate in the range of $\left(-\frac{\pi}{2},\frac{\pi}{2}\right)$ as values above this range provides multiple set points for the controller.

7.3 Response at Startup

If the state of the household side DC link capacitor is discharged during startup, the controller senses a large voltage difference. The adaptive PI gain arrangement shown in Figure 7.5 switches the PI gain values until the capacitor is charged to 350 V. The voltage variations of the household side bridge at startup is shown in Figure 7.6. Voltage variations with no load and a full load of 7 kW are shown to demonstrate the response of the controller.

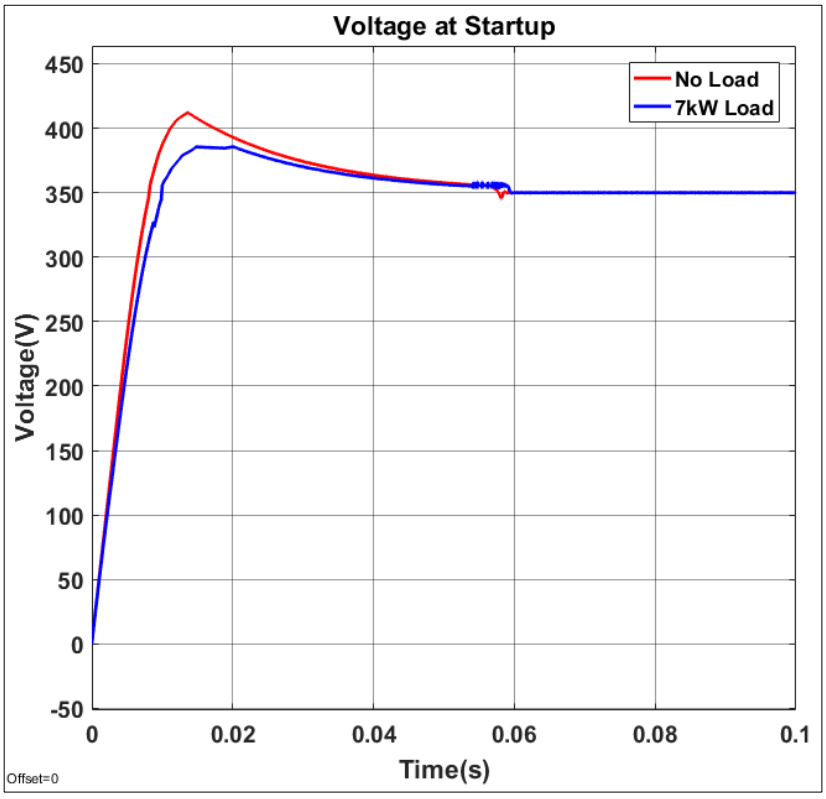

Figure 7.6: Voltage variation of the household side DC bus during startup

The response variation between full load and no load has a slight variation in overshoot. The damping is expected with the increase of the load. In both cases the PI gains switch around 60 ms which is about 3 cycles of the AC waveform.

7.4 Response During a Fault

During a fault, the DC bus voltage is driven to zero with a high current being drawn from the source. As the voltage at the DC bus does not recover, the controller output saturates at 1.57 rad ($\pi/2$). As the fault continues, the integral component accumulates this error continuously until the fault is cleared. Once the fault is cleared the accumulated error results in a high overshoot at the controller output before reaching steady state. This is known as integral windup. There are two methods known as back calculation and clamping to eliminate integral windup. In this application the clamping method is used. In clamping, a control logic is used to limit the integral action during the saturation period. The response of the controller during a fault condition is shown in Figure 7.7. The behavior with and without clamping is shown for comparison. With the fault being cleared at 200 ms the voltage overshoots up to 1500 V without clamping. With anti-windup clamping, the controller behaves as expected without overshooting.

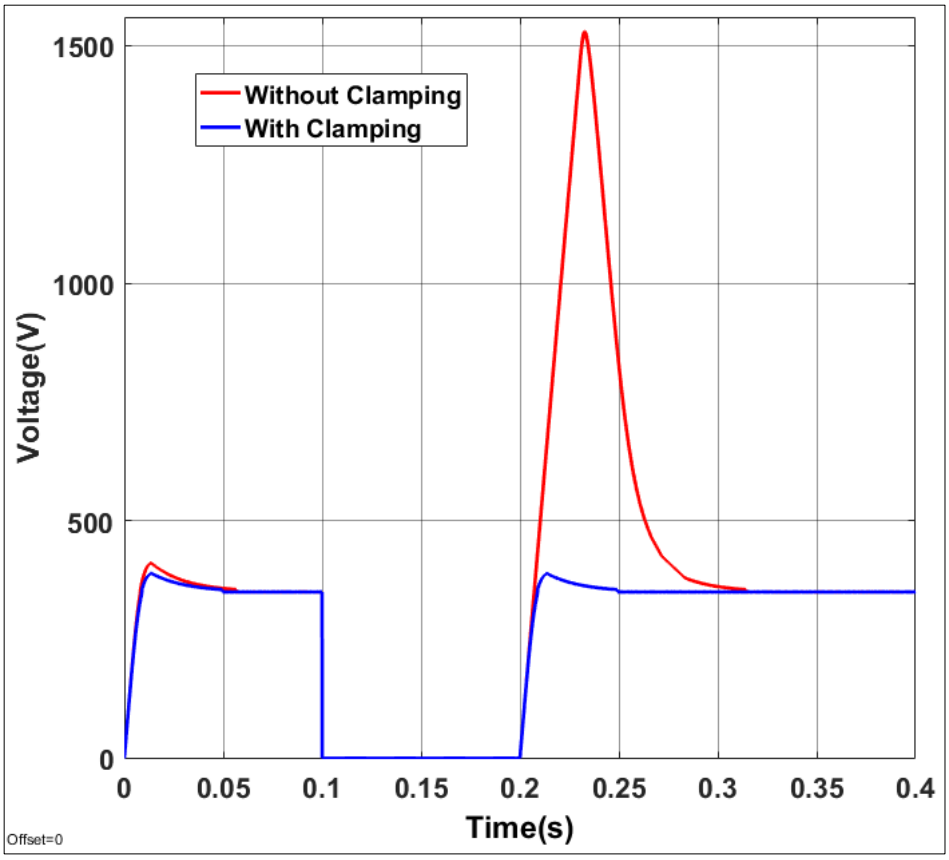

Figure 7.7: Integral windup with and without clamping

7.5 Gate Pulse Generation

The gate pulse generation circuit used for the dual active bridge was expanded with the inclusion of an additional component to the household side. The developed configuration is shown in Figure 7.8.

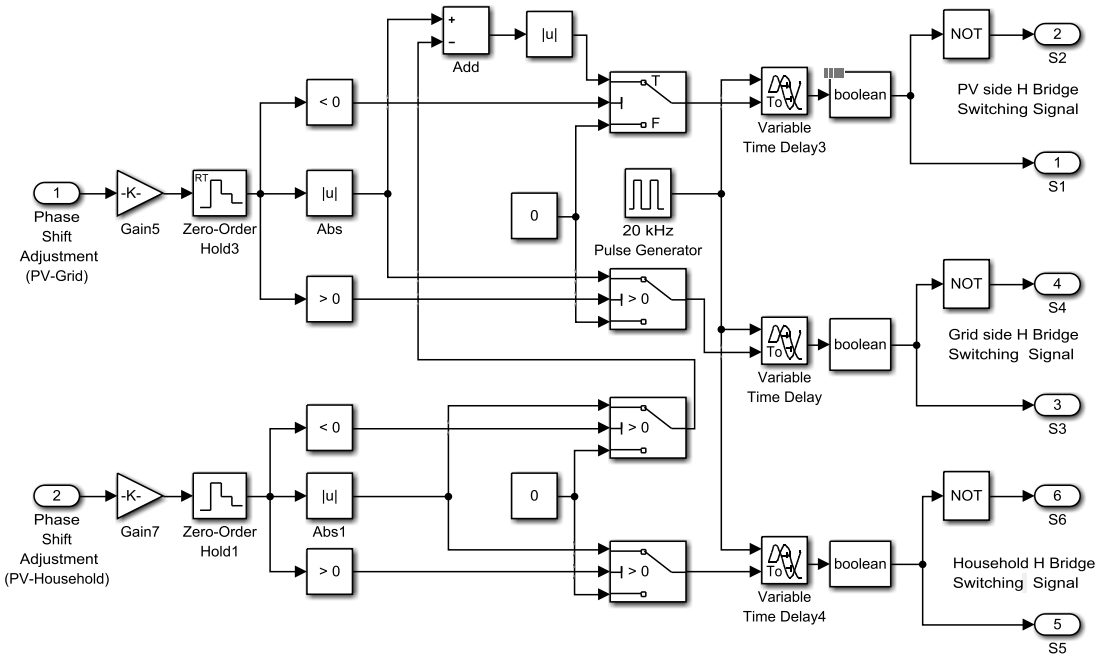

Figure 7.8:Gate pulse generation circuit for the TAB

During the first and second power flow scenarios, a variable time delay proportional to the phase shift is given to the household and grid side bridges. As the household load increases above the PV generation, the grid side controller adjusts the phase shift and delay the PV panel side bridge switching signal in order to draw power from the grid. The household side bridge phase shift is adjusted accordingly with reference to the PV panel side. The phase shift generated when the power is fed from the PV array to the grid and household is shown in Figure 7.10 while the power flow from grid to household is shown in Figure 7.9. The Figure 7.9 shows that the PV array switching pulse is delayed with respect to the grid side switching pulse. As the grid side waveform stays behind, this indicates that the power is being drawn from the grid. The phase shift generated between PV array and household defines the amount of

power drawn from the PV panel, while the shift between the grid side and the household defines the power drawn from grid side to the household.

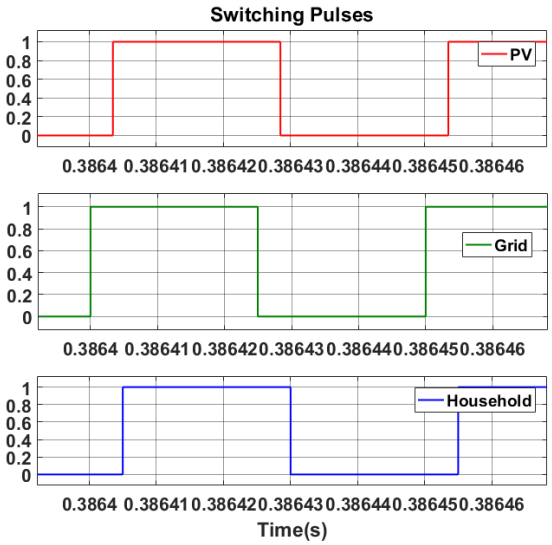

Figure 7.9: Switching pulses of the converters(PV+grid->household)

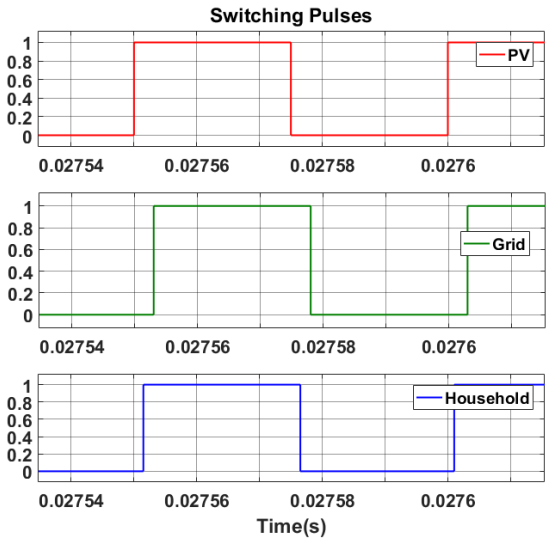

Figure 7.10: Switching pulses of the converters(PV-> grid+household)

7.6 TAB Based PV Inverter

The PV array, grid tie inverter and the household inverter were connected to the respective ports of the TAB. The PV array and the DC link capacitor was connected as the input to the PV side bridge. The grid tie inverter was connected to the grid side bridge with its dq controller. The inverter designed in chapter 5 for the DAB configuration (Figure 5.14) was used for the household side port of the TAB. The advantage over this system is that the household load is connected to an isolated steady DC bus unlike the previous dual active bridge arrangement, which makes it immune to irradiance variations and allows distributed resource interconnection. The block diagram of the TAB is shown in Figure 7.11 with all the PV system components.

The developed Simulink model of the TAB arrangement is shown in Appendix V. In addition to the household loads, a DC load is connected at the household side DC bus to represent a distributed resource.

The system has four controllers. The TAB voltage controllers maintain the output voltages at the household and grid side DC buses. The $\boldsymbol{I_d}$ reference generator

generates the I_{d_Ref} reference for the output grid tie inverter, which maintains the power flow in and out of the grid. The household inverter maintains the output voltage at 230V.

The next chapter contains the simulation results that demonstrate the advantages and improvement comparison over the Transformerless, Dual active bridge and Tri active bridge based topologies.

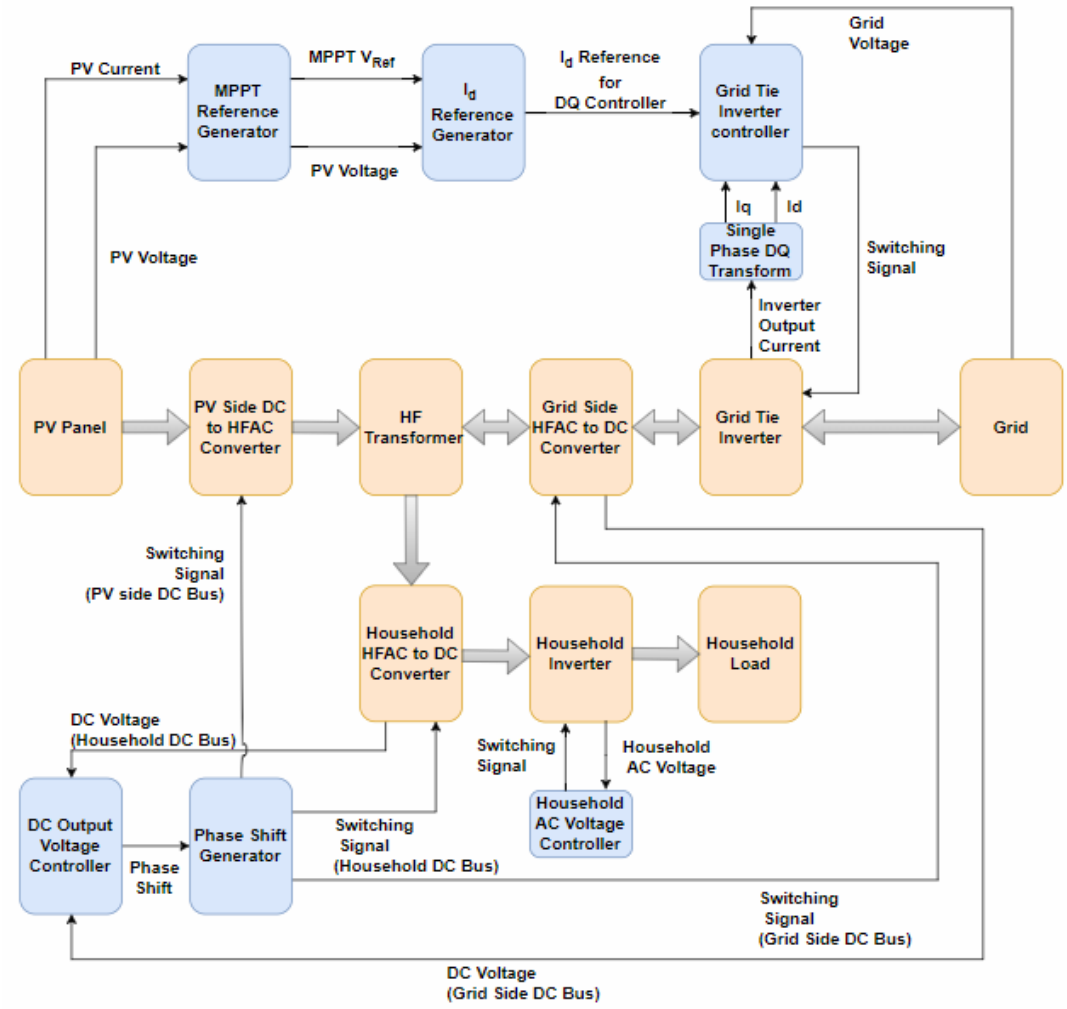

Figure 7.11:Block diagram of the TAB based PV inverter

8 COMPARISON AND SIMULATIONS RESULTS

This chapter contains the power quality comparison and the fault isolation capabilities of the following inverter configurations.

- Transformerless inverter
- Dual active bridge inverter (Household load at grid side)
- Dual active bridge inverter (Household load at PV array side)
- Tri active bridge inverter

The harmonic and fault current limiting capabilities and the behavior of the system during a fault is also discussed. The power flow through the TAB with varying irradiance characteristics and reactive and active household loads were simulated. Finally, the system was simulated with the presence of grid voltage harmonics to compare it with one of the measured household inverters.

8.1 Simulation Setup: Harmonic Analysis

The simulations were conducted on the MATLAB Simulink platform. The controller configurations used in the I_d reference generator, grid tie inverter and the household inverter were the same for all the arrangements. The same output filter tuned in chapter 4 was used at the output of the grid tie inverter.

A variable step solver with a time step of $5x10^{-7}$ s was used. for the simulation. The solver algorithm was set to be determined by the software. The simulation was executed for a period of 2 seconds.

The maximum irradiance for the PV array was taken as 1000 Wm^{-2} with an operating temperature of 40 ºC. The temperature was kept constant throughout the simulation while varying the irradiance. Two loads were used at the household side. A linear load of 2500 W with a power factor of 0.85 and another nonlinear load of the same capacity. The nonlinear load was used to demonstrate the harmonic isolation capability through the DAB and TAB inverter arrangements. As a built in non-linear load was not available in Simulink, it was created by connecting the 2500 W inductive load through a diode bridge as shown in Figure 8.2. An 800 W DC load was connected

to the household side DC bus of the TAB and the PV array side of the DAB. The simulation sequence used for harmonic comparison is shown in Figure 8.1.

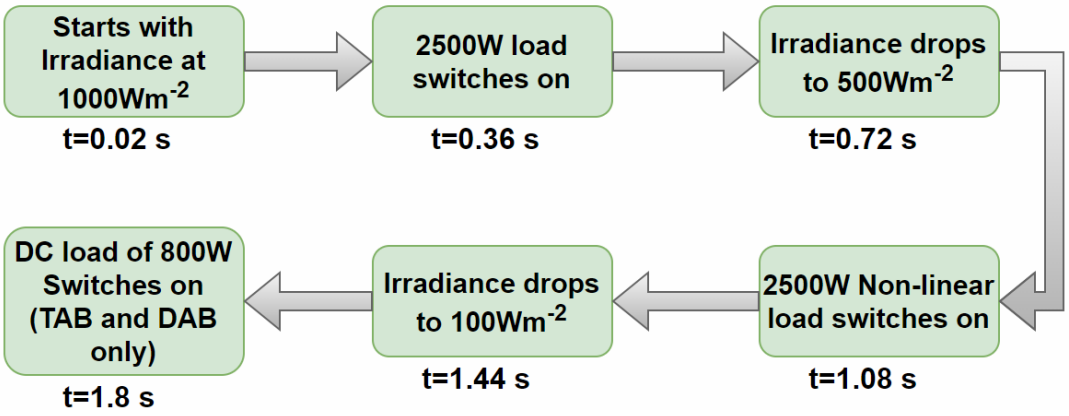

Figure 8.1: Simulation sequence for harmonic analysis

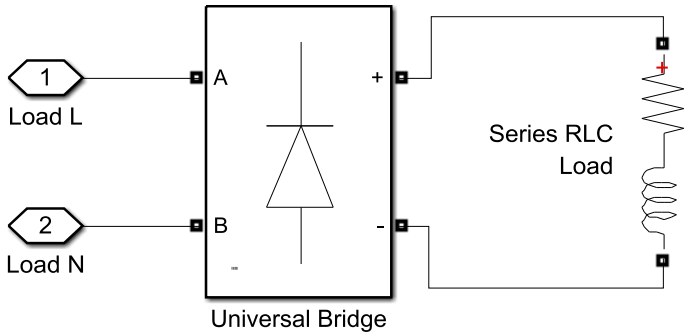

Figure 8.2: Simulink model of the nonlinear load

The TDD and THD was measured at the output of the grid tie inverter. The THD of voltage and the TDD of current can be given using equation 8.1.1 and 8.1.2. As the maximum power output of the PV array is 3120 W, the maximum demand load current (I_L) for the TDD calculation was taken as 14 A.

$$\%THD_V = \frac{\sqrt{\sum_{n=2}^{N} V_n^2}}{V_1} \times 100 \qquad (8.1.1)$$

$\boldsymbol{V_n}$=rms magnitude of individual voltage harmonics

$\boldsymbol{V_1}$=rms magnitude of fundamental in voltage

$$\%TDD_I = \frac{\sqrt{\sum_{n=2}^{N} I_n^2}}{I_L} \times 100 \qquad (8.1.2)$$

$\boldsymbol{I_n}$=rms magnitude of individual voltage harmonics

$\boldsymbol{I_L}$=rms maximum demand load current

As a built-in calculation for TDD was not available in MATLAB, the TDD and THD calculation blocks were built as shown in Figure 8.3. The THD of current was multiplied by the RMS of the fundamental and divided by the RMS of the maximum demand to calculate the TDD.

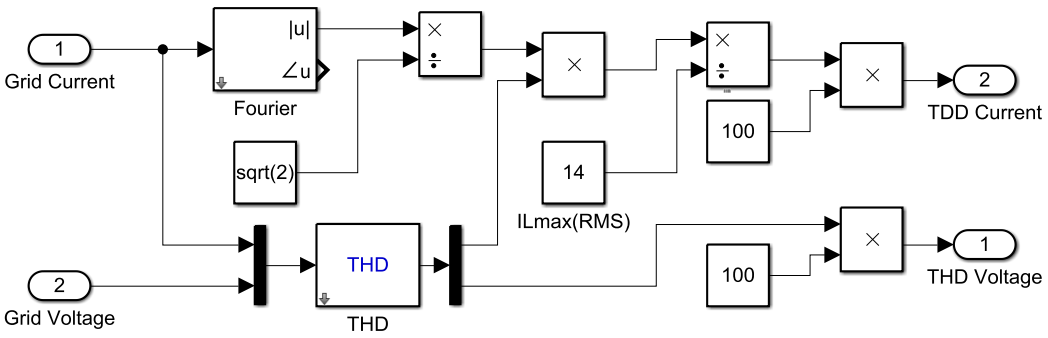

Figure 8.3: THD and TDD calculation block

8.1.1 Transformerless Inverter

The transformerless inverter model was subjected to the simulation sequence shown in Figure 8.1. The block diagram of this inverter and its subsystems is shown in Figure 4.24 of chapter 4. The power flow of the inverter is shown in Figure 8.4. The first plot shows the irradiance variation over the simulated period. Second plot shows the active power output of the PV array and the household power consumption measured at the point of common coupling. The third plot shows the reactive power consumption at the household.

The power output of the inverter has reached from 2875 W to 267 W with the decrease of irradiance. The overshoot seen during irradiance variation can be considered acceptable as in reality the irradiance does not change rapidly as shown in the figure. In this case however the irradiation was varied in a slew rate of 1/8000 in order to limit the simulation time. After the irradiance dropped from 500 Wm^{-2} to 100 Wm^{-2} the active power consumption of the household load has dropped from 5129 W to 5059 W as the grid voltage has slightly varied with the PV array power output.

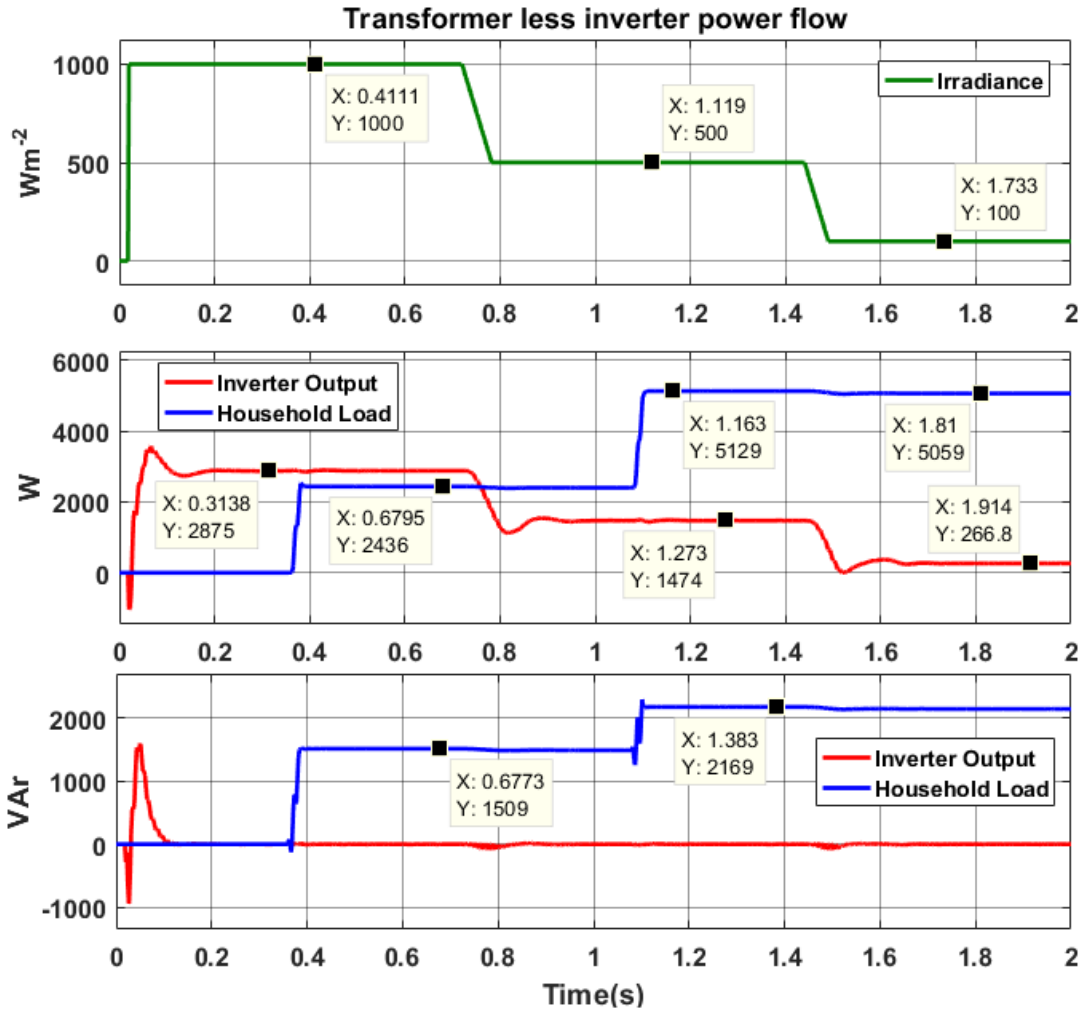

Figure 8.4: Power flow of transformerless inverter

The harmonic measurement of the inverter is shown in Figure 8.5. The measurements indicate a 2.16% of TDD during the maximum power output of the inverter with no loads connected at the household. Once the irradiance decreased to 500Wm^{-2} the TDD has decreased to 1.46%. The THD of voltage stays around 0.15%.

Once the nonlinear household load was turned on at 1.08s, both the TDD and THD have significantly increased. The TDD of current drawn from the grid has increased up to 21% and the THD of voltage increases up to 1.76%. As the household load is directly connected to the grid in this configuration, there is no isolation for load harmonics and the resultant harmonic currents are drawn directly from the grid.

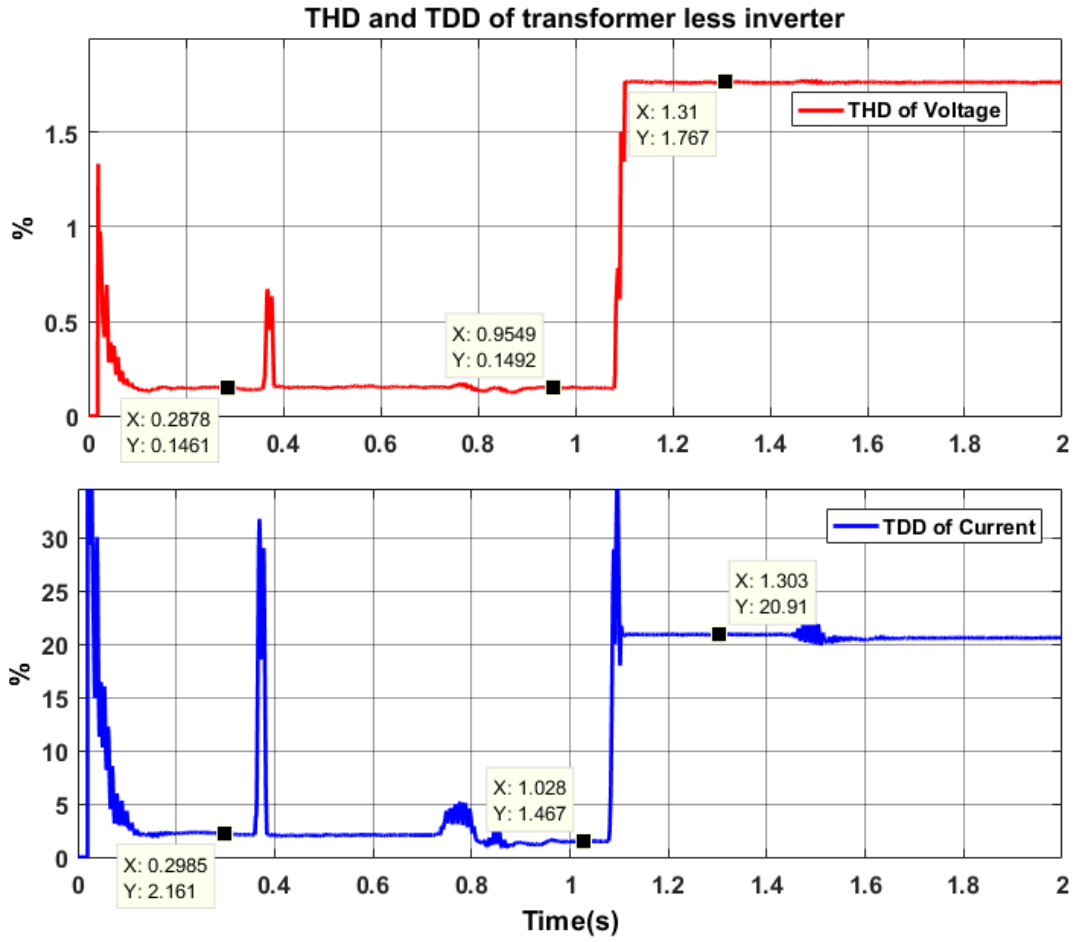

Figure 8.5: THD and TDD of transformerless inverter

The harmonic spectrum of the inverter output current during the maximum PV output is shown in Figure 8.6(a). At the maximum power output, the inverter output current exhibits a third harmonic component of approximately 2.4%. The harmonic spectrum of the current drawn from the grid side is shown in Figure 8.6(b). It shows that the nonlinear load draws a wide range of harmonic currents from the grid which leads to the high amount of TDD shown in Figure 8.5.

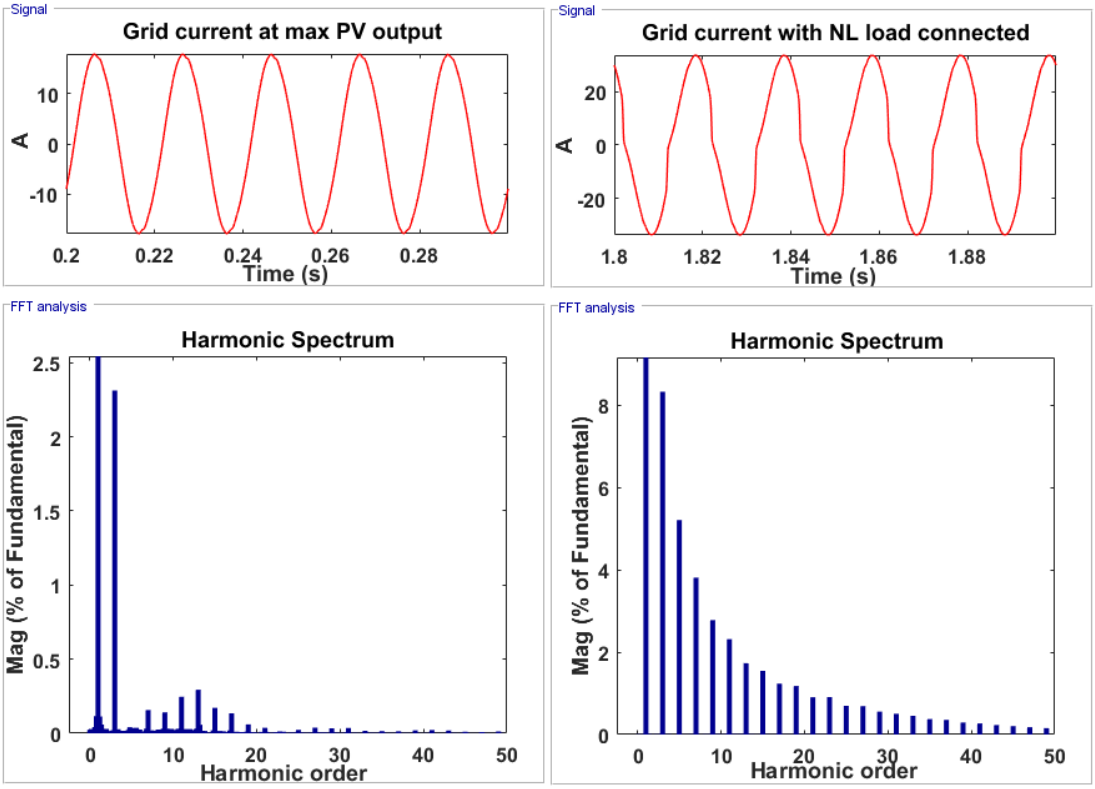

(a) (b)

Figure 8.6: Harmonic spectrum of grid current during maximum power output and connection of the nonlinear load

8.1.2 Dual active bridge inverter (household load at grid side)

The block diagram of this inverter arrangement is shown in Figure 5.13 of Chapter 5. As the household load is connected at the grid side similar to the transformerless inverter, the power flow characteristic is same as shown in Figure 8.4. However, the presence of the dual active bridge has reduced the harmonics generated at maximum PV generation. The TDD of current gives a value of 0.6% during the maximum power output of the inverter which is about 4 times less than the transformerless inverter. It has further reduced to 0.34% as the irradiance dropped to 500Wm^{-2}. The voltage harmonics have stayed around 0.1% until the nonlinear load was switched on. Once the nonlinear load is connected, the TDD and THD values become similar to the transformerless inverter. This is expected as there is no isolation

between the loads and the grid. The THD and TDD variation is shown in Figure 8.7 with the harmonic characteristic of the transformerless inverter.

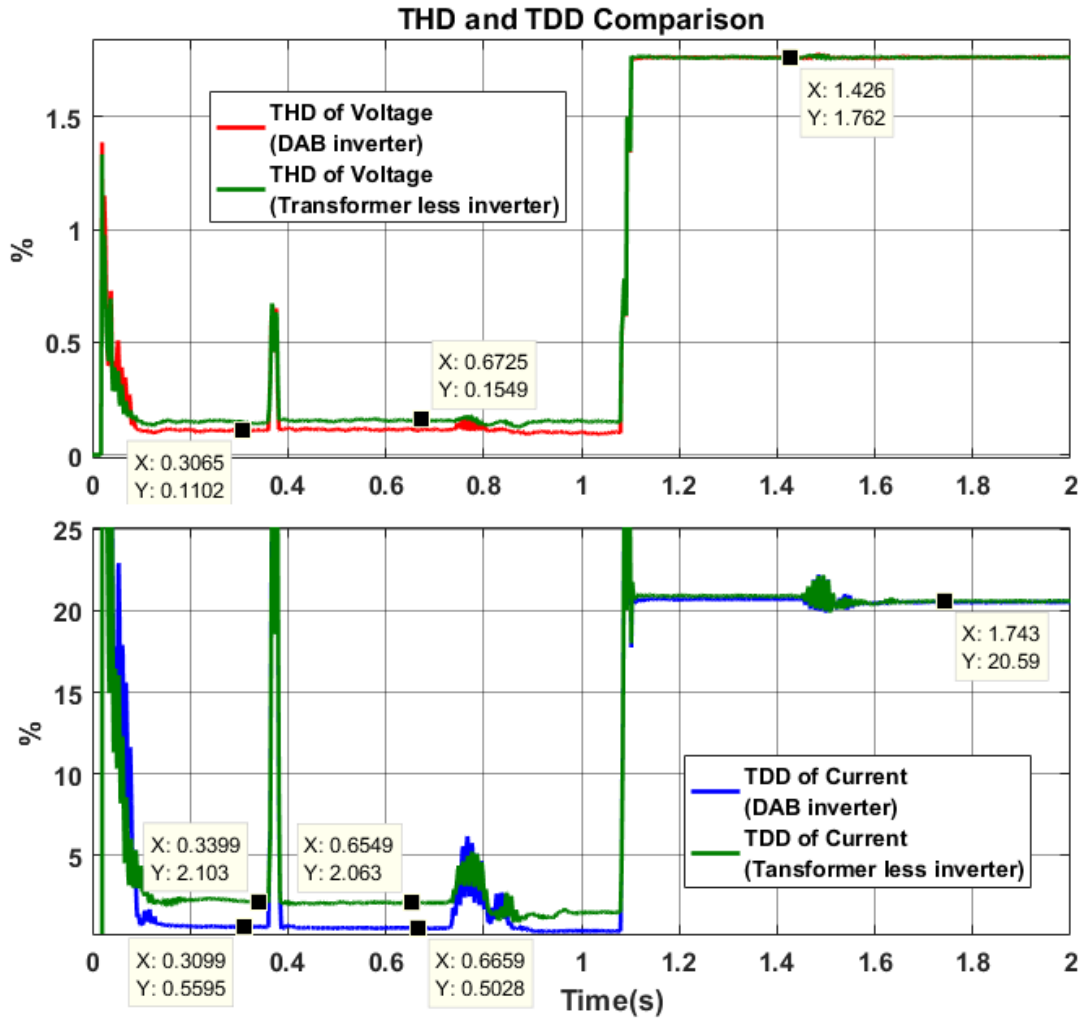

Figure 8.7:THD and TDD comparison of DAB inverter (load at grid side) and the transformerless inverter

The harmonic spectrum for the DAB inverter at its maximum power output is shown in Figure 8.8. The third harmonic component has reduced to 0.35% which is 6 times less than the value shown in Figure 8.6(a) of the transformerless inverter. This shows the lower order harmonic isolation capability of the DAB. The harmonic spectrum with the nonlinear load is not shown as it is similar to the spectrum of the transformerless inverter.

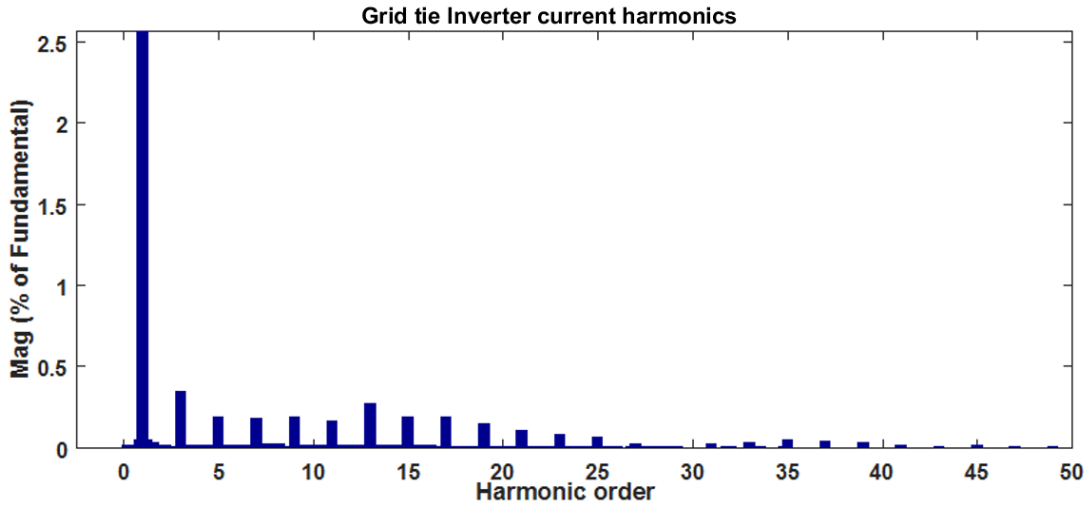

Figure 8.8: Harmonic spectrum for the DAB inverter output current at max PV generation

8.1.3 Dual active bridge inverter (household load at PV array side)

The block diagram of this inverter is shown in Figure 5.15 of Chapter 5. The power flow of this inverter configuration is shown in Figure 8.9. As the household load increases the power output of the grid tie inverter reduces, redirecting power to the household port. Once the irradiance drops below 500 Wm^{-2}, the grid tie inverter operates as a converter drawing power from the grid. Once the non-linear load is switched on at 1.08 s, the power generated by the PV array becomes insufficient to cater the household load. The required power is drawn from the grid through the grid tie inverter. The power is shown as negative as the direction of current is inverted by 180 º and is drawn inwards.

The Figure 8.9 also shows that the irradiance variations have affected the household power output at 0.72 s and 1.44 s. Furthermore, load transients fluctuate the power output taking about 500ms to reach steady state. Even though an 800 W DC load was connected at the DC bus, the actual power consumed is around 774 W as the voltage of the DC bus had varied with irradiance.

The harmonic comparison with the Transformerless inverter is shown in Figure 8.10. At max PV generation, the plots indicate a THD and TDD similar to the previous

DAB arrangement. However, the power fluctuations have affected the harmonic variations as well. The biggest advantage of this arrangement can be seen upon the point where the nonlinear load is switched on. Unlike the directly connected Transformerless and DAB inverters, this configuration prevents harmonic currents being drawn from the grid.

However, there are some disadvantages present. The irradiance variations have caused fluctuations at the household side power output. Furthermore, an isolated steady DC bus is not available for distributed resource interconnection as the PV side DC bus voltage varies with irradiance and temperature in a range of about 80 V. These drawbacks can be mitigated with the TAB inverter configuration as it provides an isolated DC bus at the household with a steady DC voltage maintained at 350 V.

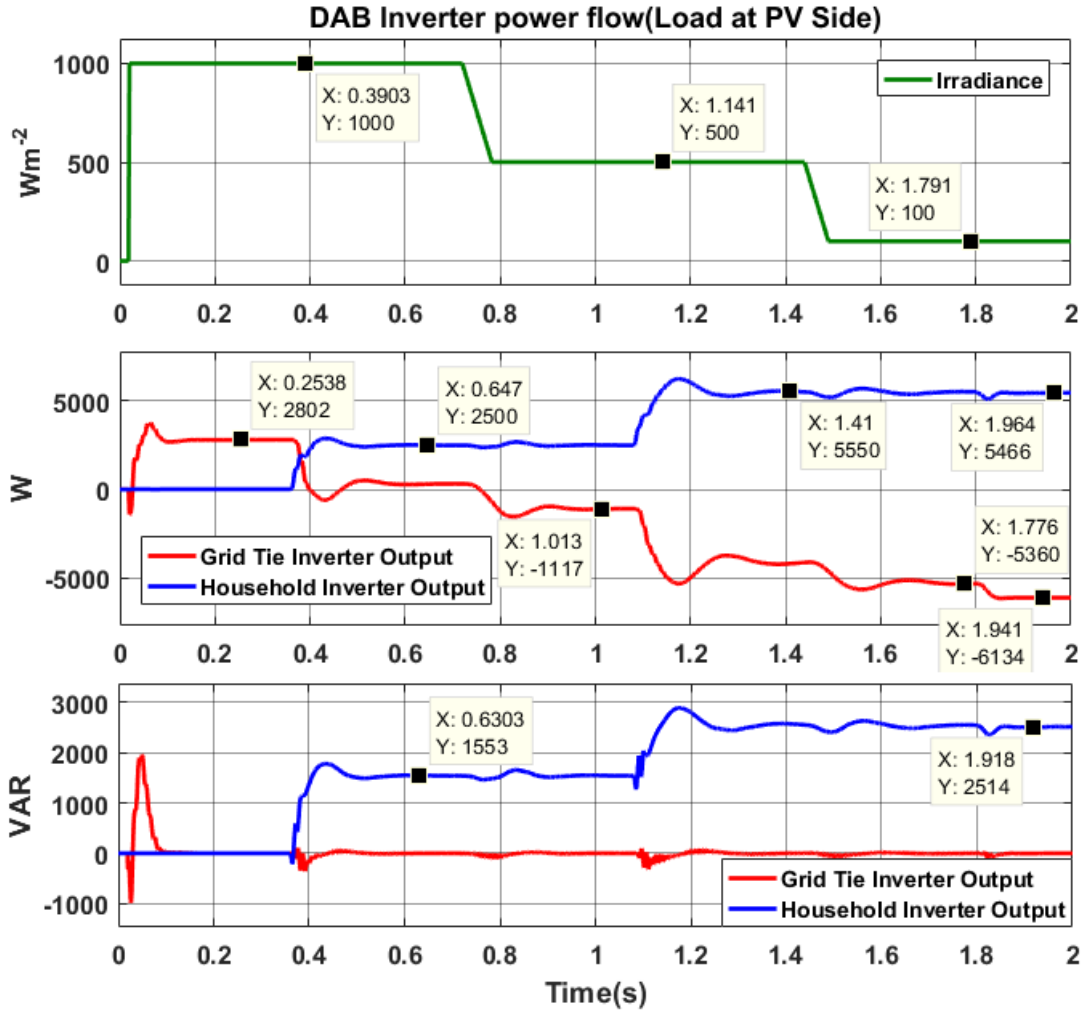

Figure 8.9: Power flow for the DAB inverter (load at PV array side)

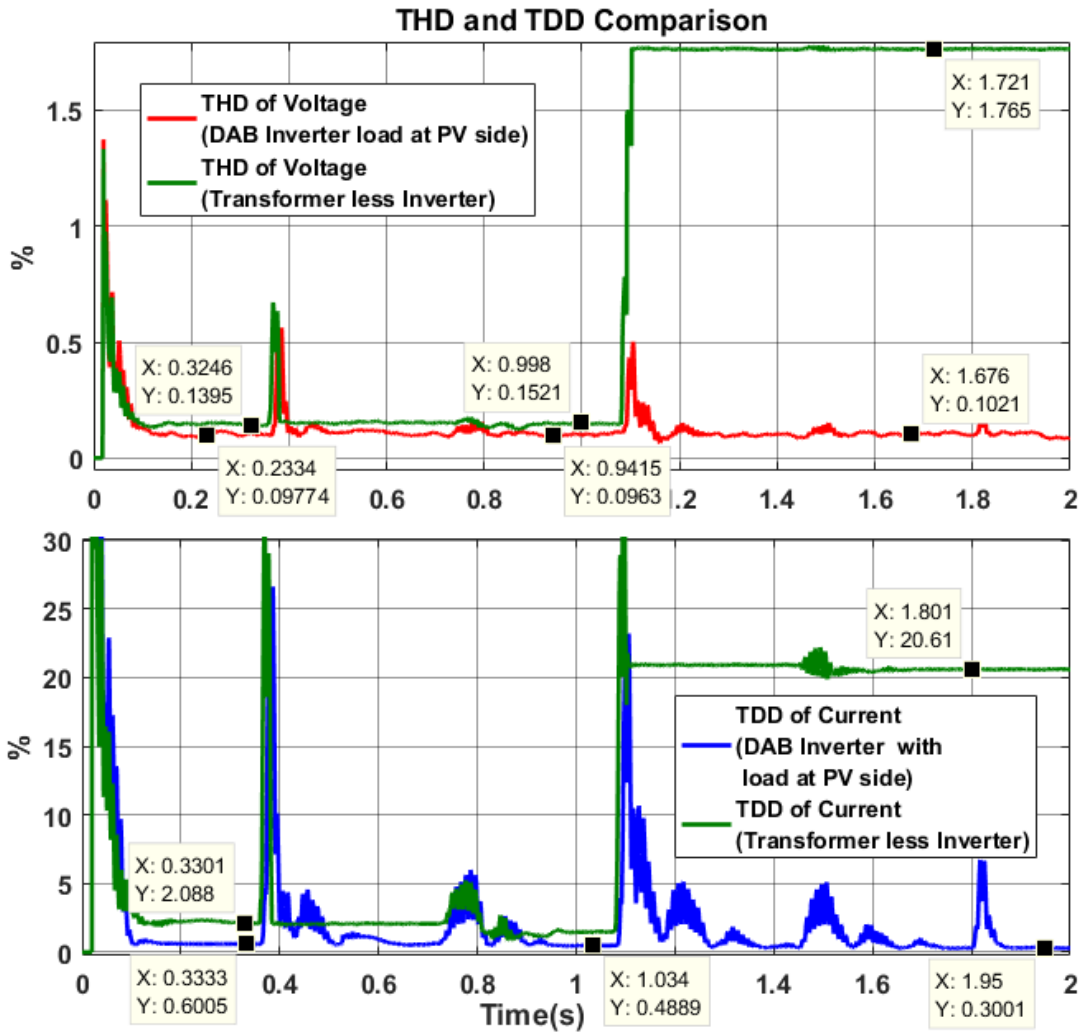

Figure 8.10: THD and TDD comparison of DAB inverter (load at PV array side) and the transformerless inverter

8.1.4 TAB based PV inverter

The block diagram of this inverter is shown in Figure 7.11 of Chapter 7. Unlike the previous DAB configuration, the load transients have a minimal impact on the household side power. The power flow shown in Figure 8.11 indicates that steady state is achieved in about 150 ms after the load is switched on. No fluctuations can be seen at the household inverter output due to the irradiance changes.

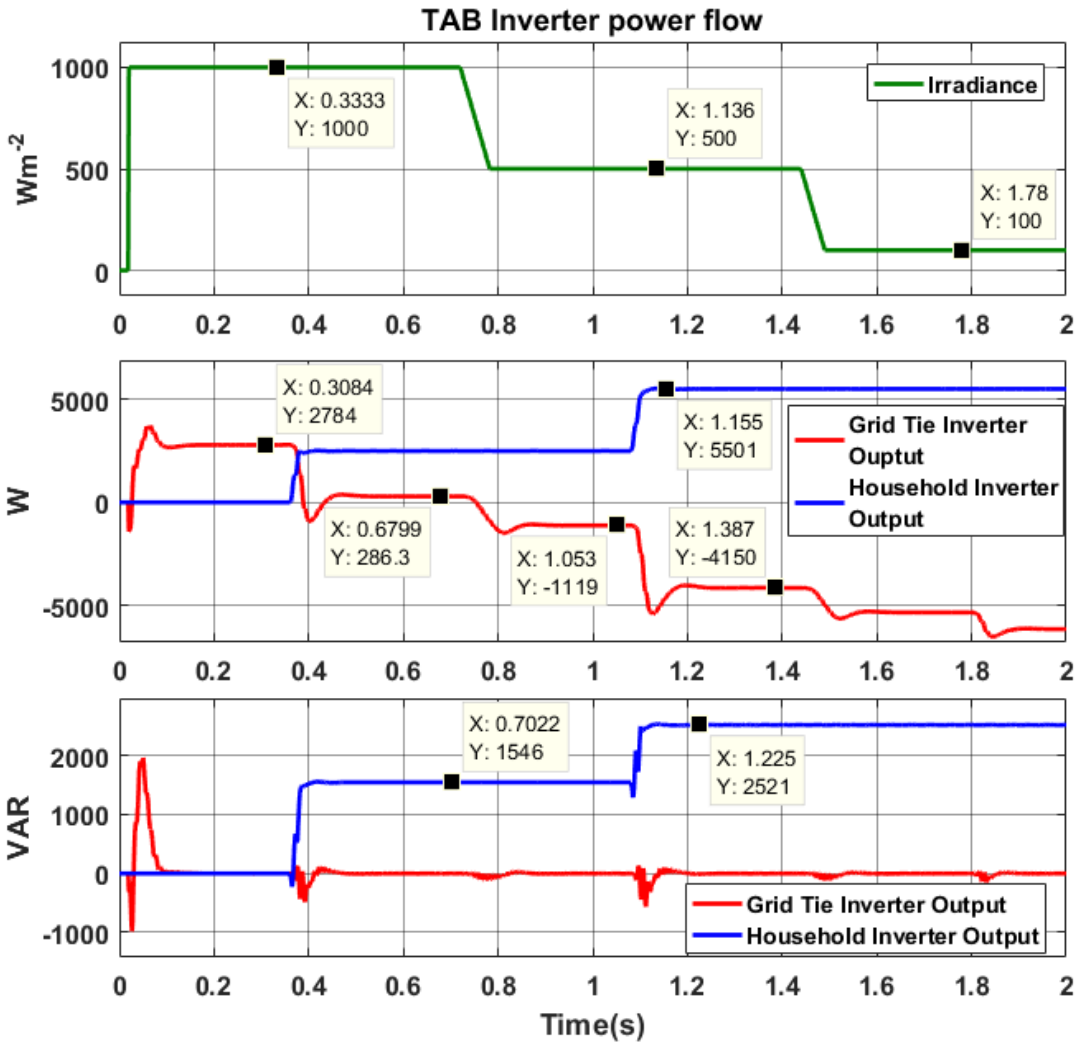

Figure 8.11: Power flow of the TAB inverter

The TDD and THD measurements at the output of the Grid tie inverter is shown in Figure 8.12. The steady state TDD and THD values shown are similar to the previous DAB inverter. The load transients take only about 50 ms to stabilize the TDD and THD compared with the transformerless inverter. Once the non-linear loads are connected the TDD and THD stays around 0.3% and 0.1% respectively.

The variation of the household side RMS voltage of the TAB and the DAB inverters are shown in Figure 8.13. The fluctuations and overshoots due to the irradiance variations are visible with the DAB inverter while it has been completely eliminated in the TAB inverter.

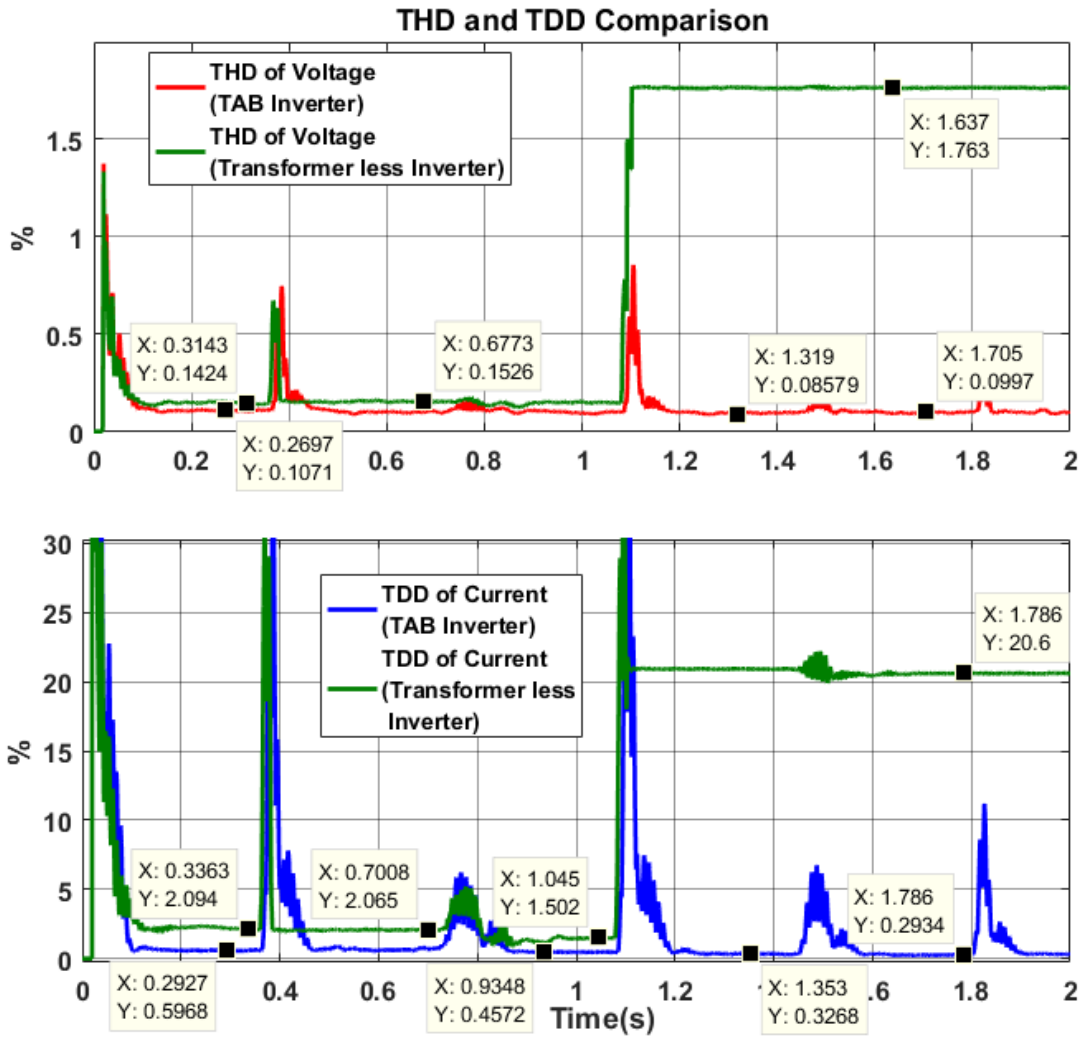

Figure 8.12: THD and TDD comparison of TAB and the transformerless inverter

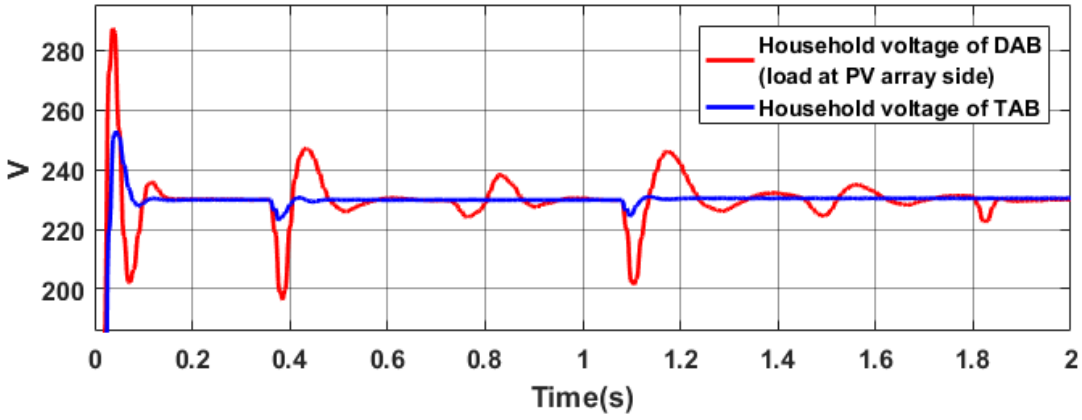

Figure 8.13: Household side RMS voltage variation of the TAB inverter compared with the DAB inverter (load at PV array side)

The current harmonic spectrums of the grid tie and household inverter outputs at 1.6 s are shown in Figure 8.14. The Grid tie inverter harmonics present are below 0.1% even after the nonlinear load was connected. At the same time the current harmonics spectrum of the household side of the TAB shows a spectrum similar to Figure 8.6(b) of the transformerless inverter. This shows that the harmonics generated from the household loads do not propagate towards the grid.

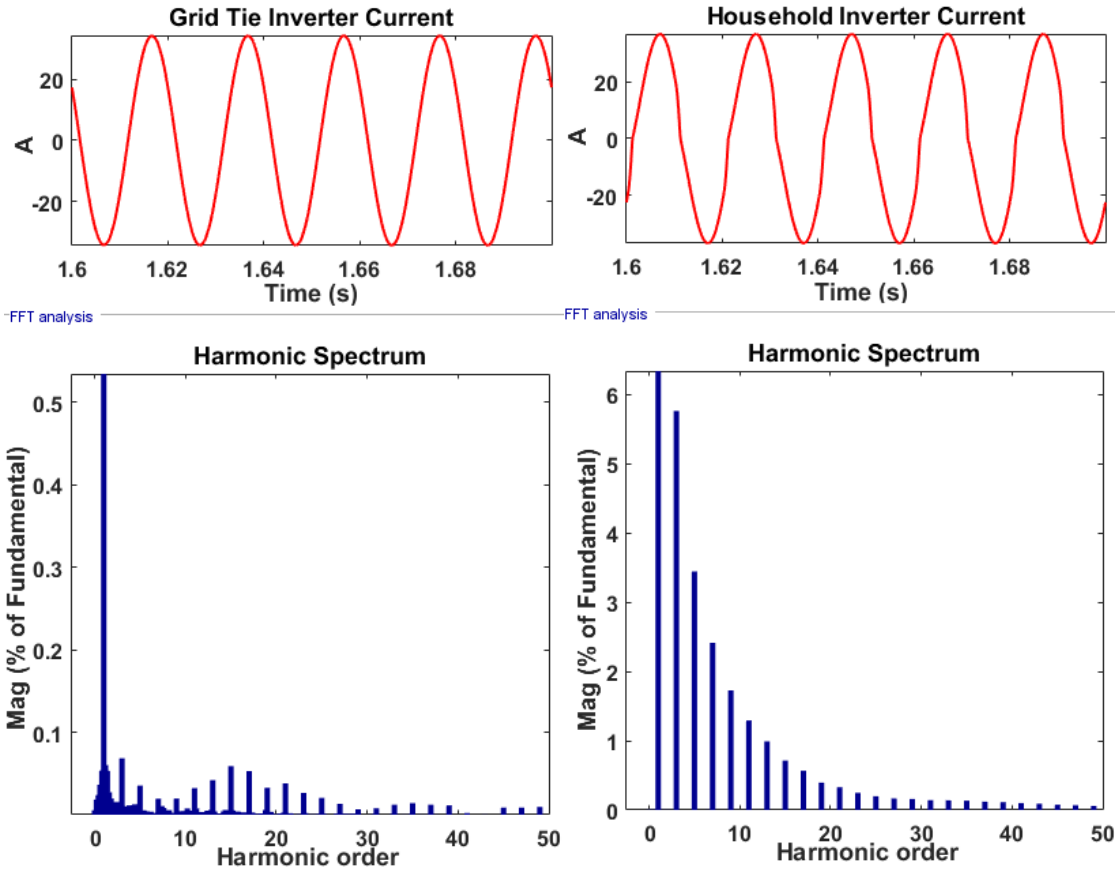

Figure 8.14: Harmonic spectrum of the grid current and the household inverter current with the non-linear load

8.2 Simulation Setup: Existing Voltage Harmonics

The above simulations were carried out with the inverter connected to a grid model that had ideal conditions. In the actual condition, the LV grid contains voltage harmonics generated due to existing nonlinear loads. Therefore, it is necessary to

simulate the designed TAB inverter with the presence of grid voltage harmonics to get a more accurate understanding about its harmonic performance.

In order to simulate this, the individual voltage harmonics obtained at the maximum power output in inverter number 3 were used to create a harmonic voltage source in Simulink. The individual harmonics of the FFT spectrum were added and given as a reference signal to a controlled voltage source to create the required harmonic source. The developed voltage source was connected in series at the consumer side of the conductor impedance in the developed grid model. The modified grid model and the harmonic generator code is shown in Figure 8.15.

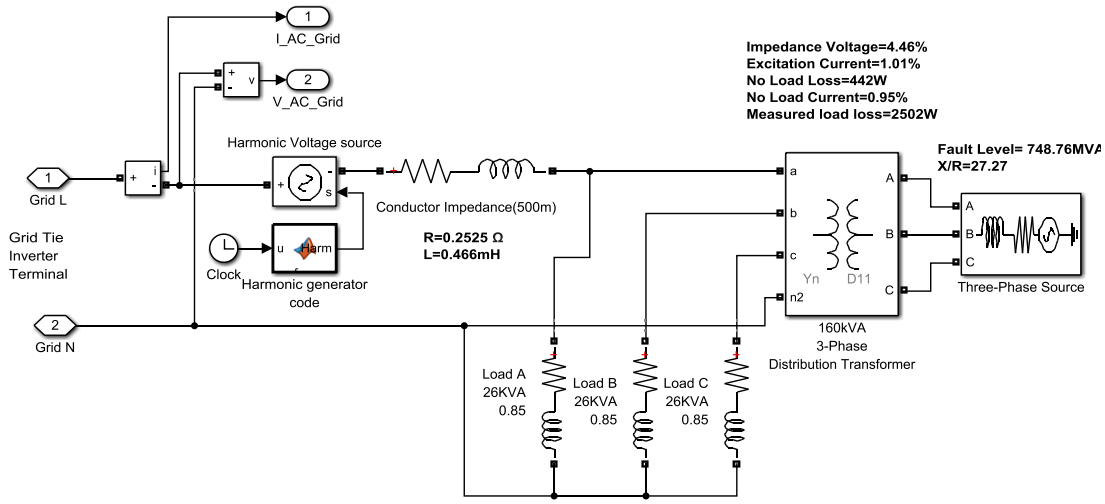


```
function Harm = fcn(u)
%#codegen
wt=2*pi*50*u;
H_arr=[325  0.57525 7.27675 0.23075 1.63475 0.13975 ...
    1.3975  0.1105  2.0475  0.104   0.69225 0.104   ...
    0.67275 0.09425 0.60775 0.10075 1.16675 0.0845  ...
    0.22425 0.08125 0.429   0.06825 0.22425 0.04875 ...
    0.07475 0.0715  0.2795  0.06175 0.13975 0.052   ...
    0.23075 0.039   0.12025 0.0585  0.10075 0.07475 ...
    0.195   0.08125 0.0845  0.0585  0.15275 0.06175 ...
    0.10725 0.10725 0.078   0.13975 0.13325 0.104   ...
    0.1755  0.07475];
Harm=0.442; %DC component
for n=2:50
H = H_arr(n)*sin(n*wt);
Harm=Harm+H;
end
```

Figure 8.15: Simulink model and MATLAB code for the harmonic source

The harmonic spectrum obtained by the Fluke 435 Series-II instrument is shown in Figure 8.16. The simulated harmonic spectrum of the grid voltage after connection the harmonic source is shown in Figure 8.17.

The figures indicate an exact similar harmonic spectrum to the measured voltage harmonic spectrum of inverter 3. The simulation results for the TDD and THD of TAB and transformerless inverters are shown in Figure 8.18.

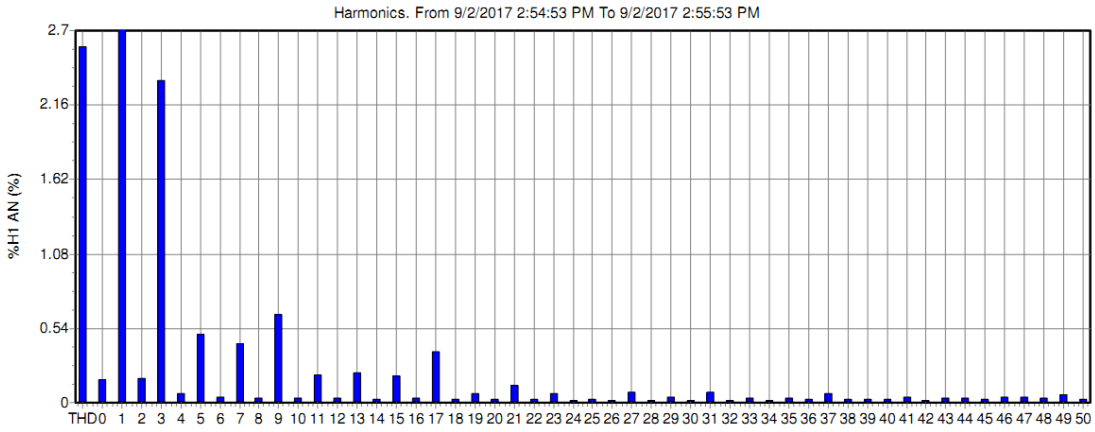

Figure 8.16: Grid voltage harmonic spectrum measured using fluke 430 Series II

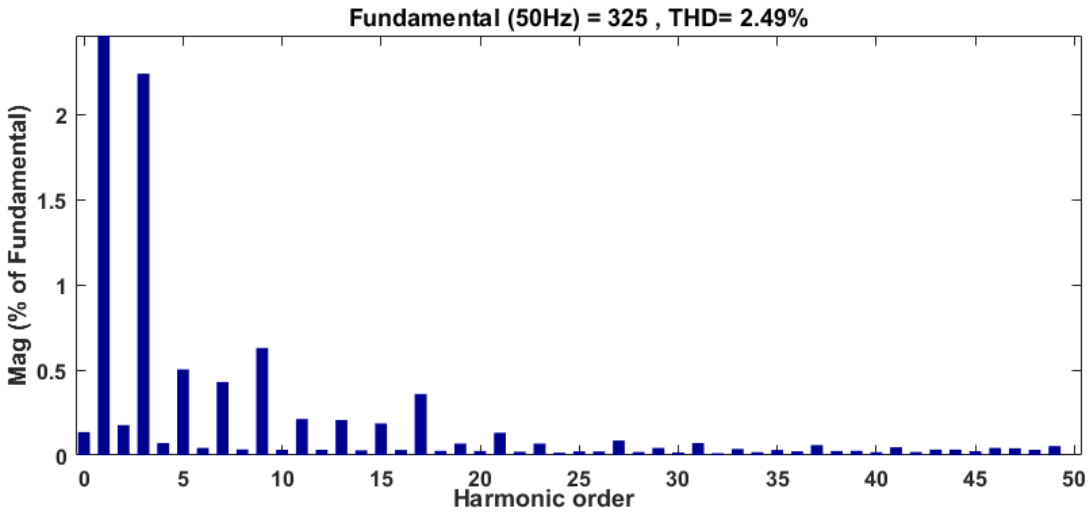

Figure 8.17:Grid voltage harmonic spectrum generated by the Simulink model

The TDD of the transformerless inverter has reached up to 5% during the maximum power output, while in the TAB inverter it has reached only up to 3.4%. As

the irradiance reduced, the TDD of the transformerless inverter has increased up to 5.5%, where it has remained unchanged in the TAB inverter. Similar to the previous simulated results, the TAB has maintained a low TDD and THD with the nonlinear load connected at household side whilst it has increased with the transformerless configuration.

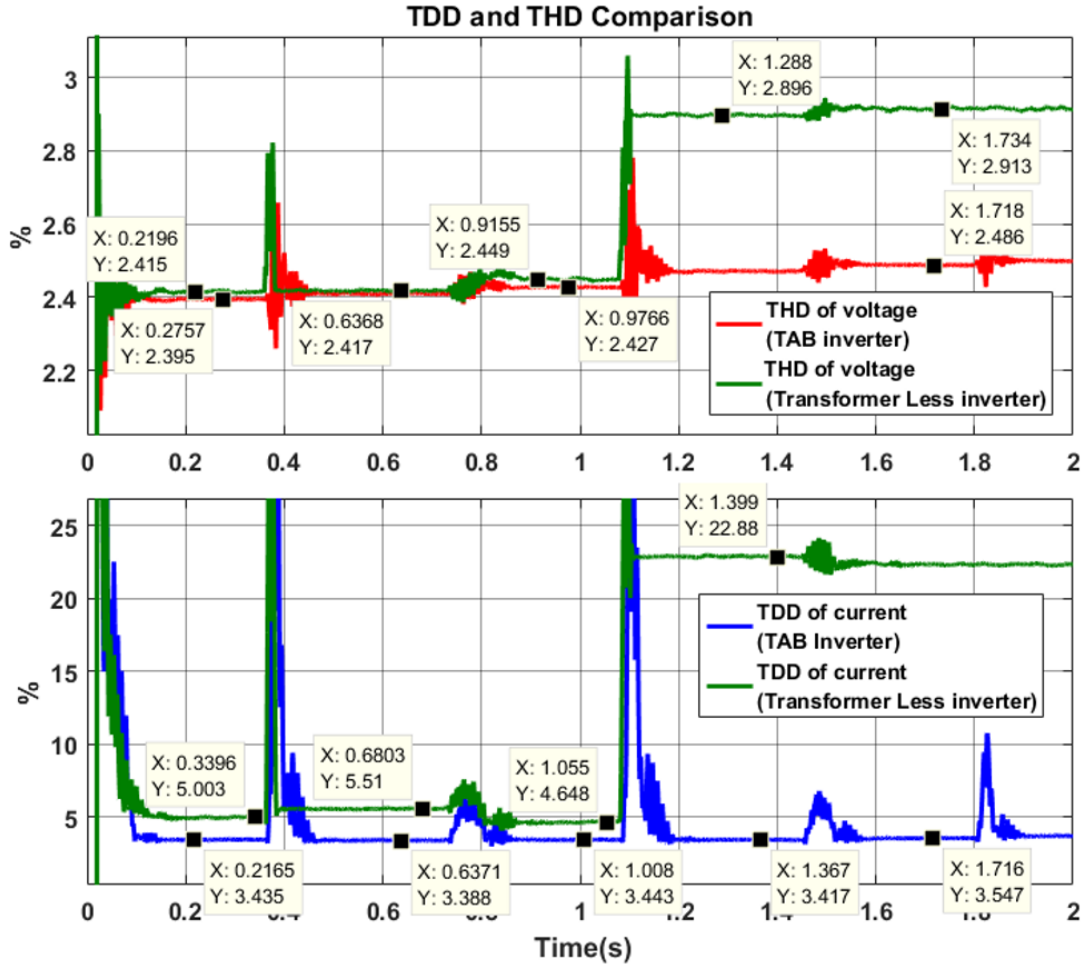

Figure 8.18: THD and TDD comparison of TAB inverter and the transformerless inverter with grid voltage harmonics present.

8.3 Simulation Setup: Fault Current Limiting

The Transformerless inverter does not inherently provide fault isolation or fault current limiting capabilities. If a fault occurs at the DC bus between the PV array and the inverter, the fault is fed through the anti-parallel diodes of the inverter.

Furthermore, as the household is connected directly to the grid, any fault at the household is fed by the grid before the breaker mechanism interrupts the current. This is common for line to line and line to ground faults in the transformerless system.

The DAB and TAB arrangements can limit this current by controlling the current through converter bridges. During a line to ground fault, there is no current flow from the grid as the two configurations provide galvanic isolation through the high frequency transformer.

However, during a DC fault at the PV array, the voltage at the DC bus drops to zero. This is seen by the I_d reference generator, and as explained in chapter 5, the the I_d reference generator generates a negative I_{d_ref} resulting in a reversal of the power flow. This reverse current can be controlled by limiting the output of the PI controller. In the DAB configurations with loads at grid side, the negative saturation limit of the PI controller can be set to zero as there is no requirement for bidirectional power flow. But in the TAB configuration and the DAB with loads at the PV array side, there is a requirement for bidirectional power flow. Therefore, the negative saturation limit is set to -42, which is the peak value for an RMS current of 30A. This is done in the simulation by limiting the output of the I_d reference generator shown in Figure 4.15 of chapter 4. The modified configuration is shown in Figure 8.19. The saturation limiter setting can be configured in the PI controller with anti-windup clamping. In this case it is shown externally for illustration purposes.

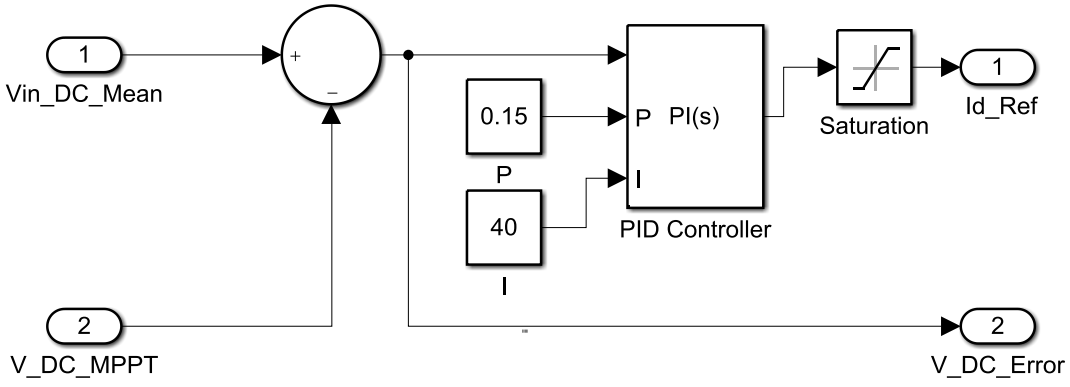

Figure 8.19:Current limiting configuration in Simulink

The saturation limit of the PI controller is configurable unlike the current rating of a fuse or a breaker characteristic while providing inherent current limiting. This configuration is invalid for the Transformerless inverter as the fault current has an alternative path and is not dependent on the generated I_{d_ref}.

In order to simulate this condition, a line to line fault was created at the PV array side of the DC bus and at the household load. The response of the grid voltage and current was observed during the fault. The simulation sequence is shown in Figure 8.20. The faults were created when the household load is at its maximum and the PV array output is at its maximum.

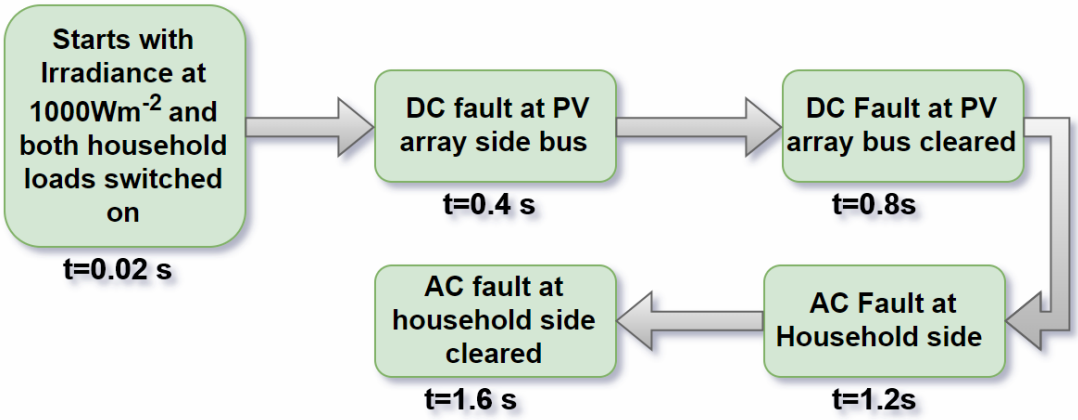

Figure 8.20:Simulation sequence for fault current limiting

8.3.1 Transformerless inverter

The grid voltage and current variation during a fault is shown in Figure 8.21. The DC fault at the PV array draws a current up to 116 A. The fault at the household draws a current of 660 A. As a result of the fault, the grid voltage during the DC fault has dropped to 200 V and to 13 V during the household fault. The fault current at the PV array has been limited due to the filter impedances.

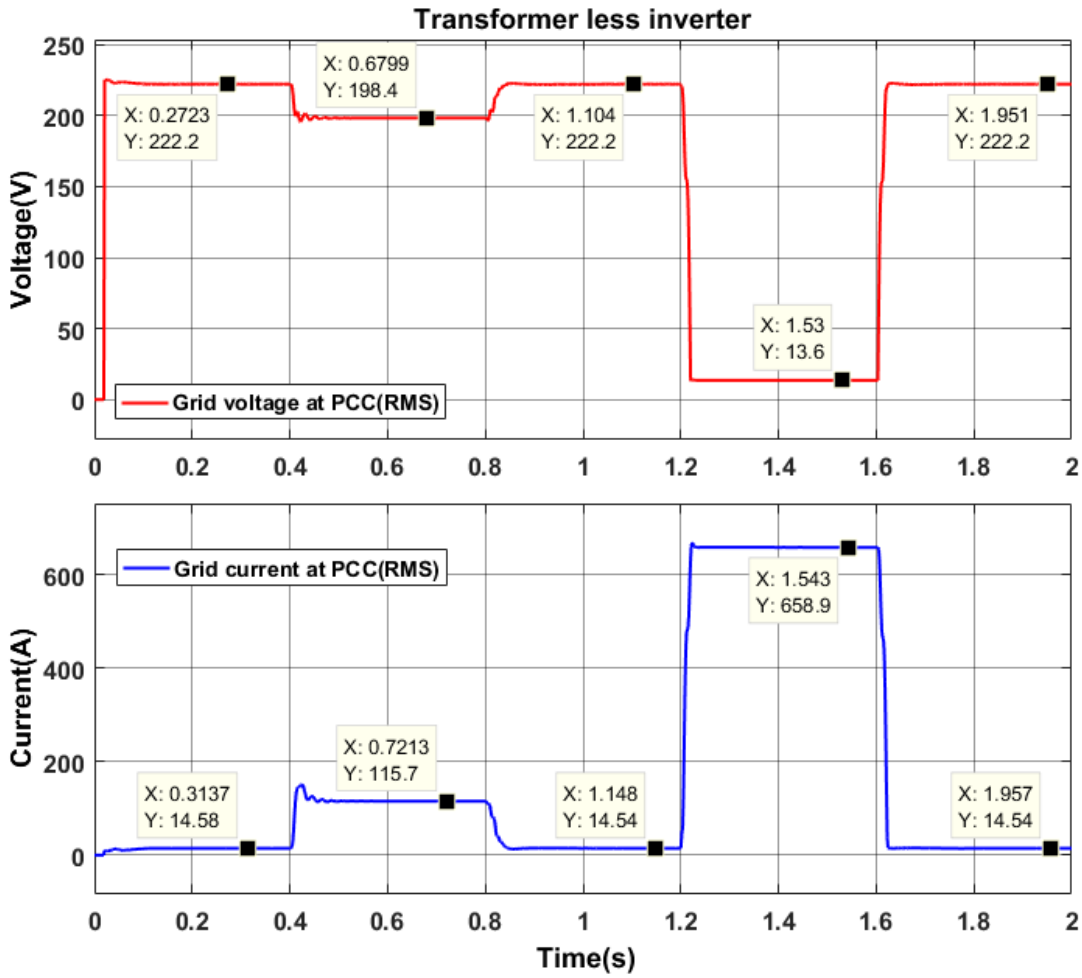

Figure 8.21: Grid voltage and current during the fault of the Transformerless inverter

8.3.2 Dual active bridge inverter (load at grid side)

This configuration provides isolation for the PV array through the HF transformer. The response on the grid voltage and current at the PCC is shown in Figure 8.22. Once the fault occurs at 0.2 s, the power output of the PV array becomes unavailable. As a result, power is drawn from the grid to facilitate the household load requirement. Since the RMS calculation block provides only the magnitude, this can be noted by observing the output current of the inverter. The RMS output current of the inverter is shown in Figure 8.23. It indicates that during the fault at the PV array, the current drawn towards the fault is about 0.7 A. This current is allowed to flow towards the PV array as it is required to restore the voltage at the PV array side after the PV array side fault is cleared.

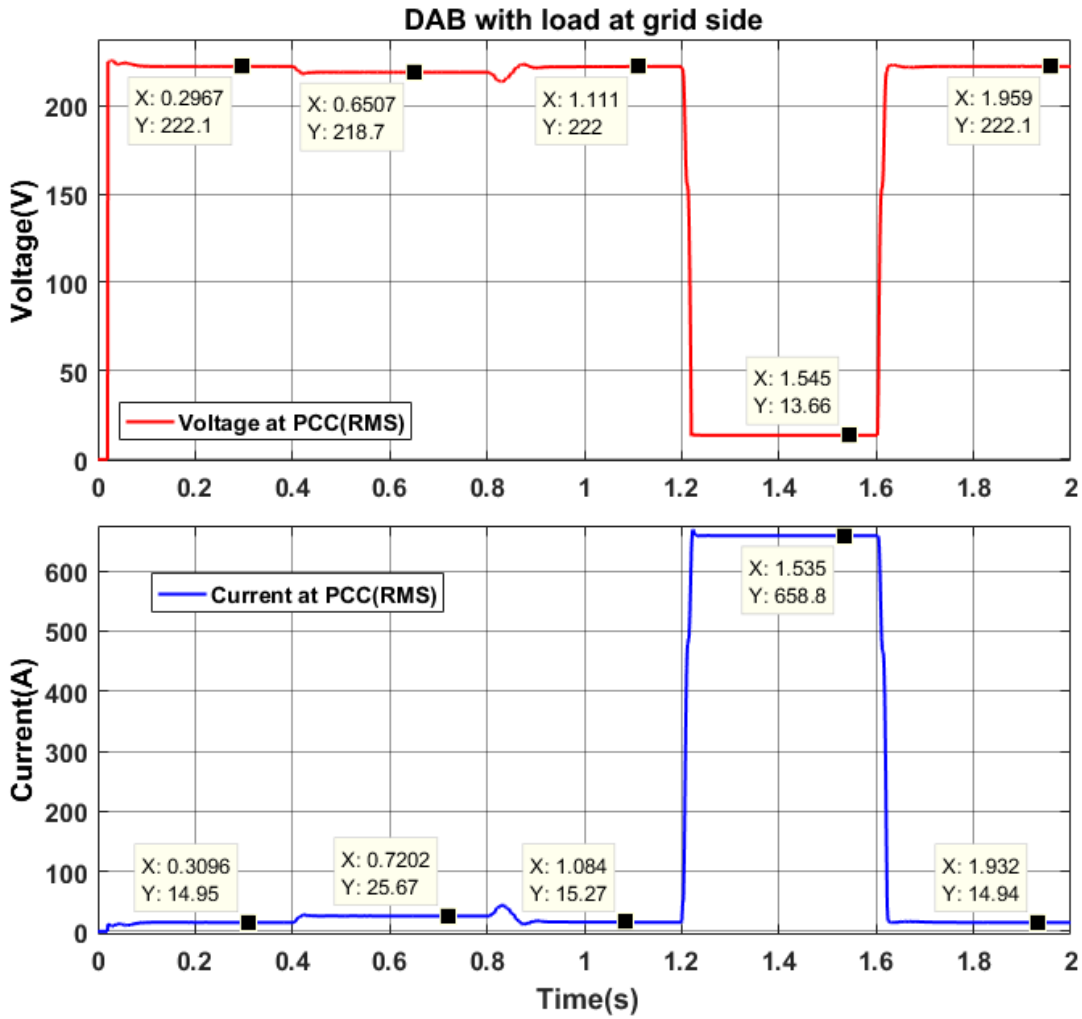

Figure 8.22 :Grid voltage and current during the fault of the DAB inverter (household load at grid side)

During the fault at the household, the currents and voltages behave similar to the transformerless configuration as it is directly connected to the grid. The current output measurement of the inverter indicates that the fault is being fed by the inverter.

However, this current is configurable and can be controlled by changing the upper saturation limit of the I_d reference generator. In this case the saturation limit is set to 30 as the peak value of the allowable maximum output current. This gives a peak RMS current of 21 A during the fault. One the fault is cleared; stability is achieved in about 150 ms in both the cases.

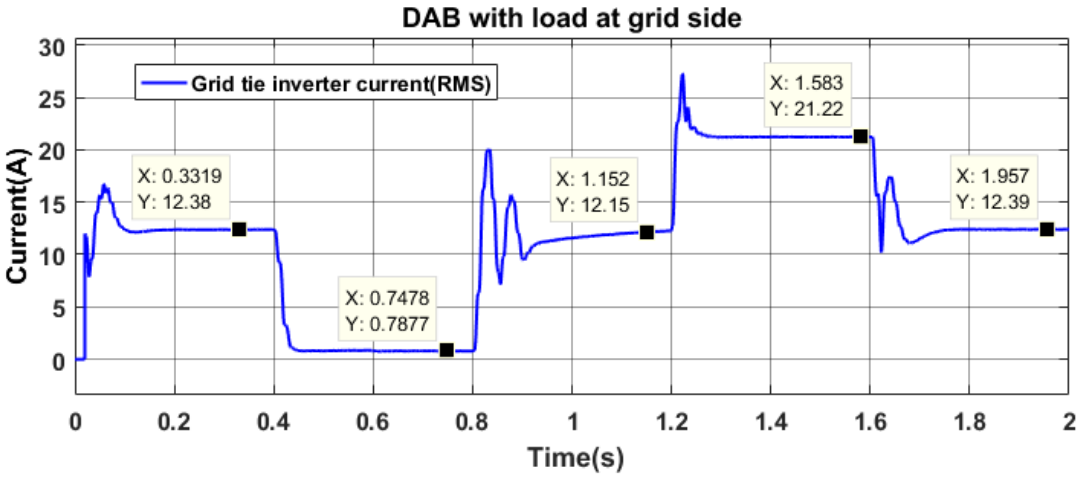

Figure 8.23:Grid tie inverter output during the fault

8.3.3 Dual active bridge inverter (load at PV array side)

This configuration has both the household and PV array isolated from the grid. Therefore, fault current limiting is possible for both the PV and household faults. The voltage and current response at the PCC is shown in Figure 8.24. Unlike the previous arrangements, both the fault currents reach only up to 30 A during the fault. As the household loads are allowed to go up to 30 A in 7 kW domestic supply, this value was set for the saturation limit of the I_d reference generator.

However, as shown in Figure 8.24, the response after clearing the fault is sluggish and takes about 500 ms to reach a steady state. Furthermore, household faults and PV array faults are not independent from each other, as both of them are connected to a DC bus without any form of isolation. Therefore, during a PV array fault, the household loads are disrupted. The household voltage and current during the fault is shown in Figure 8.25. It shows that the voltage and current output of the inverter goes to zero during the fault at the PV array side.

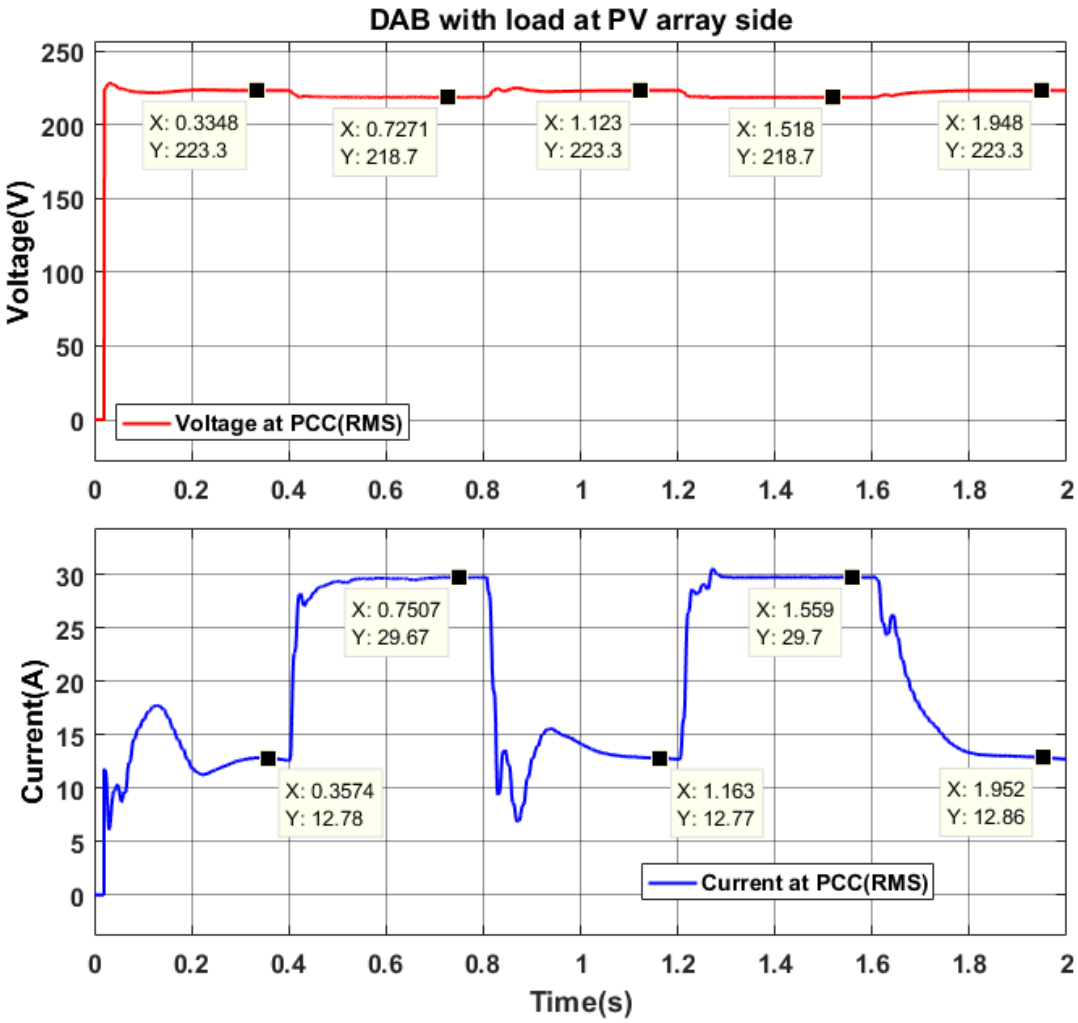

Figure 8.24: Grid voltage and current during the fault of the DAB inverter (household load at PV array side)

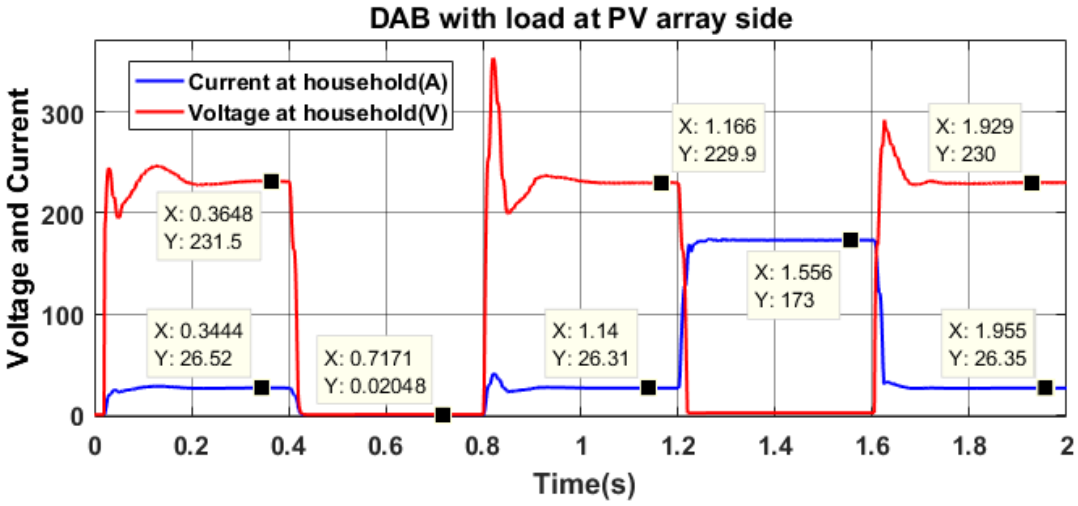

Figure 8.25: Household inverter output current and voltage during the fault

8.3.4 Tri active bridge inverter

The tri active bridge configuration provides an isolation between the PV array and the household side unlike the previous DAB configuration. The response of the system is shown in Figure 8.26. The grid voltage shows a variation of about 5 V during the PV fault. The fault current reaches 30 A and gets clamped.

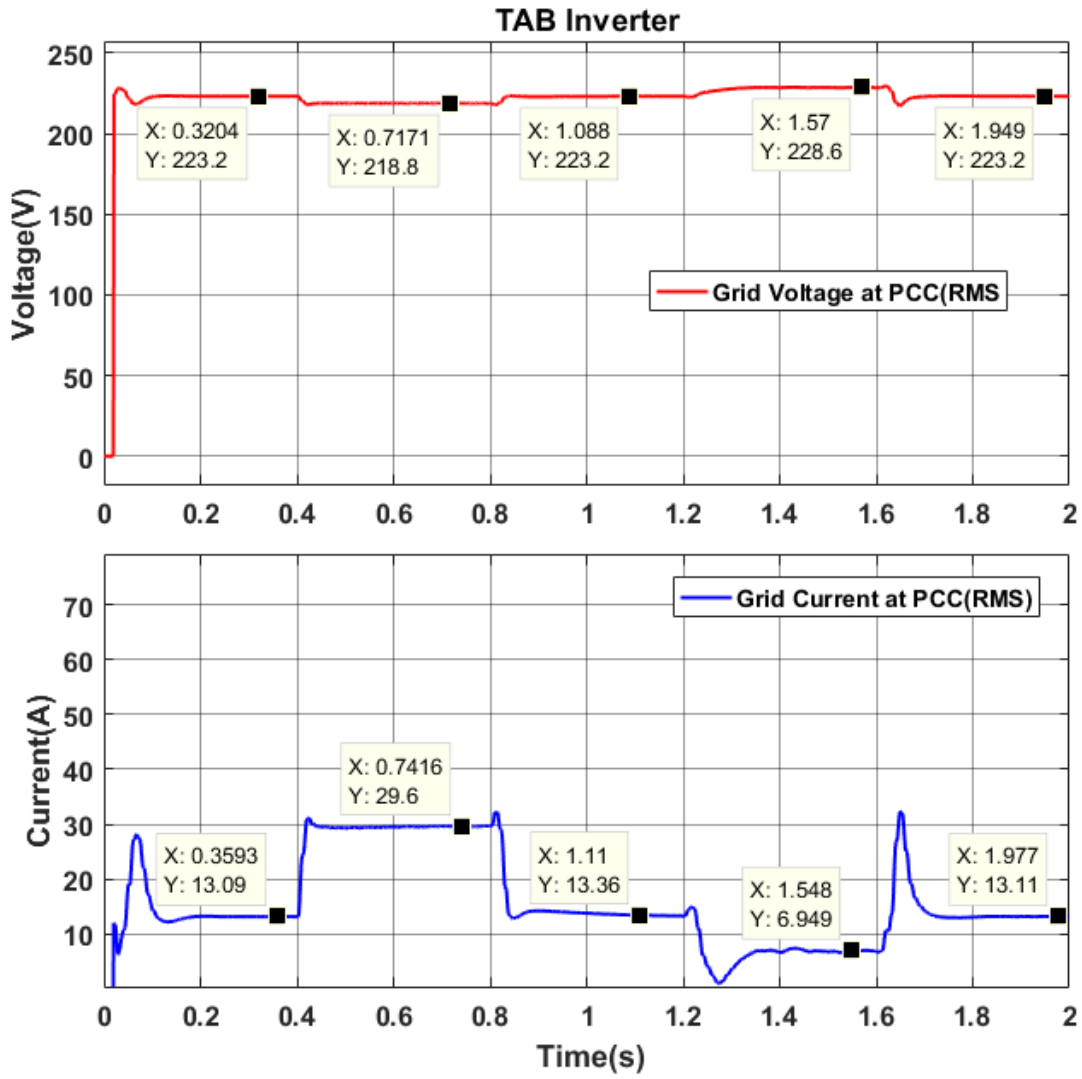

Figure 8.26: Grid voltage and current during the fault of the TAB inverter

During the household fault, the grid voltage has varied only by 5 V. The current at PCC drops to zero and increases back as the power generated by the PV array gets redirected from household port to grid port during the fault. Unlike the DAB inverter, the household load doesn't draw a current of 30A from the grid during the fault. The

fault draws about 570 W from the PV array. The rest of the power generated by the PV array (1588 W) is injected to the grid. Furthermore, the response after clearing the fault is faster than the DAB as it reaches steady state around 200 ms.

The response on the household voltage and current is shown in Figure 8.27. Except for transient at the initiation of the fault, the voltage and the current stays uninterrupted throughout the PV side fault.

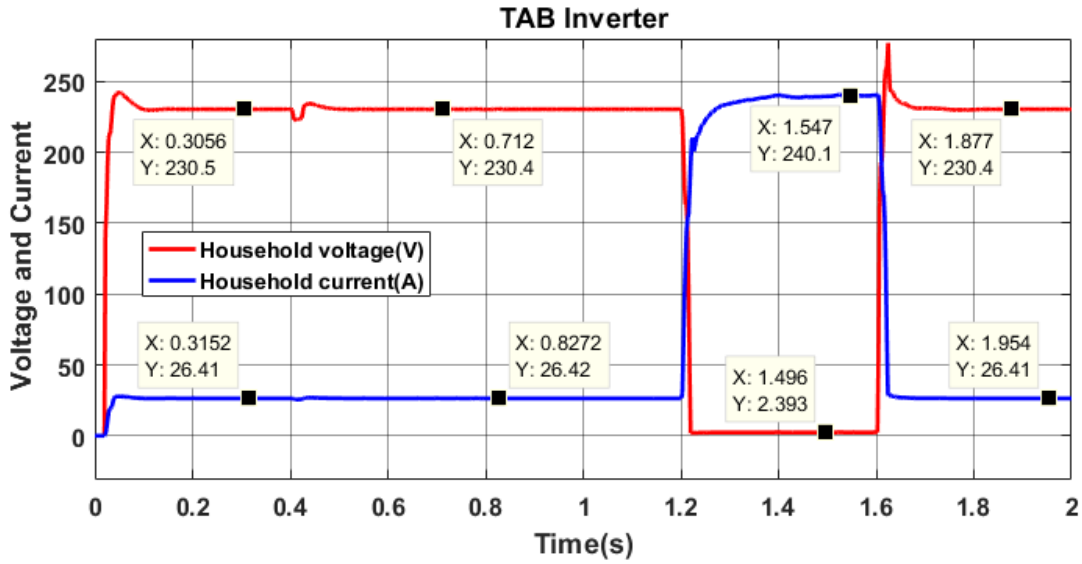

Figure 8.27: Household inverter output current and voltage during the fault

8.4 Summary

The summary of the measurements is given in Table 8.1. The conclusions based on the simulation results are given in chapter 9 with suggestions for future work.

Table 8.1: Summary of simulation results

Inverter Topology		**Transformerless inverter**	**DAB Inverter (load at Grid Side)**	**DAB inverter (load at PV side)**	**TAB inverter**
Harmonic Analysis					
THD Voltage (%)	Max PV out	0.146	0.11	0.097	0.107
	Nonlinear load	1.767	1.762	0.0858	0.102
TDD Current (%)	Max PV out	2.161	0.559	0.601	0.6
	Nonlinear load	20.91	20.59	0.3	0.293
3rd Harmonic current at max power output (% of fundamental)		2.4	0.35	0.35	0.35
TDD with grid voltage harmonics present (% at max PV output)		5.003	--	--	3.435
Time to reach steady state after a load transient(ms)		40-50	40-50	250-300	100
Fault current limiting					
Fault current(A)	PV fault	115.7	0.78	29.67	29.6
	Household fault	658.9	658.8	29.67	No impact to grid
Grid voltage drop(V)	PV fault	23.8	3.4 (due to loads)	4.6	4.6
	Household fault	208.6	208.4	4.6	No impact
Recovery time (ms)		100	100	500	200

9 CONCLUSIONS AND FUTURE WORK

9.1 Summary

The main objective of this thesis was to study the power quality issues of the existing transformerless inverters and present a solar PV inverter configuration based on a solid-state transformer (SST) topology. A measurement survey was carried out on 3 numbers of transformerless inverters to assess their output power quality. Upon recognizing the drawbacks of the existing configurations, three inverter configurations were developed based on the dual active bridge (DAB) and Tri active bridge (TAB) configurations utilized in the solid-state transformer. The existing transformerless inverter was designed and modelled initially to compare the improvements of the SST based configurations.

The selection procedure for a 3 kW PV array was presented. Two MPPT algorithms were developed and compared. A single phase dq controller was used at the grid tie inverter to control the power flow to the grid. The reference for the dq controller was generated by comparing the DC bus voltage with the output of the MPPT reference algorithm. A LCL filter was designed to minimize the switching frequency harmonics when interfacing the output inverter to the grid. To simulate the system accurately, the LV grid was modelled with the 33kV grid and distribution transformer parameters obtained from CEB.

A DAB based inverter was designed with the selection of required inductance to satisfy a power flow of 7 kW. The output voltage controller was designed and tuned for the DAB. Two configurations of the DAB were presented. One with the household load connected at the grid side and the other with the household load connected at the PV array side DC bus through an additional inverter.

A harmonic model was mathematically derived for the TAB to model the currents and voltages of its converters. The developed model was simulated in MATLAB Simulink platform for validation. Based on the developed mathematical model, controllers were derived to maintain the output voltages of the TAB ports. The designed PV array, Grid tie inverter and the Household side inverter were linked with the respective ports of the TAB and the DAB to complete the PV system.

The three developed systems were simulated and compared with the transformerless system in the MATLAB Simulink platform to assess their power quality improvements. The load side harmonic isolation capabilities and the fault current limiting capabilities of the DAB and TAB based PV inverter systems were presented. Finally, the TAB and Transformerless systems were simulated with the presence of grid voltage harmonics. The LV grid voltage harmonic spectrum of a measured inverter was used to create the individual harmonics in the LV grid model.

9.2 Conclusions and Recommendations

The TAB and DAB based inverters provide significant improvements over the existing transformerless inverter. The isolation of the load side harmonics is the biggest advantage as it prevents the consumers from polluting the LV gird with harmonics generated by non-linear loads. Nowadays consumers use LED and CFL lighting systems, inverter bases refrigerators and air conditioners that draw significantly large harmonic currents from the grid. A study conducted on harmonics generated by LED lamps show that they generate significantly large(approx. 30% of fundamental) 3^{rd},7^{th} and 9^{th} order harmonics [47] . TAB system can isolate these load side harmonics from the grid providing better power quality at the LV grid.

Furthermore, as the third harmonic component present is insignificant in all DAB and TAB systems, it reduces the losses in neutral conductors and distribution transformers. The third harmonic present in the transformerless inverter can only be reduced by significantly increasing the size of the DC link capacitor. Considering the voltage rating of the capacitor this is not a cost-effective solution. But the DAB and TAB systems will not require such high capacitances as the lower order harmonics will not propagate through the converters and the HF transformer.

DC current injection was not observed in any of the configurations. However as mentioned in the literature review, the galvanically isolated PV systems have significantly low DC current injection compared their transformerless counterparts. This can be verified during in the physical implementation.

The fault current limiting capability is the other most significant improvement. Unlike the transformerless inverter, the TAB provides full controllability over the power flow at each port. The results shown in this thesis are based on preconfigured fault current limits of the I_d reference generator. In addition to this, the phase shifts generated by the converter bridge output voltage controllers can be dynamically limited, blocking any power flow through the ports. They can be set to trigger based on a detection of a fault.

Both the TAB and DAB systems can be used to replace the transformerless PV inverters at household and commercial buildings. The household voltage fluctuations present at the second DAB configuration (load at PV array side), can be reduced by increasing the value of the DC link capacitor at the PV array side. This would however increase the cost of the system.

For larger commercial installations, the system can be scaled up and the inverters can be upgraded to three phases.

The world is moving towards smart grid solutions that incorporate more active devices such as solid-state transformers, distributed resources and distributed storage options. People are moving away from depending on utility grid for their electricity requirements to fulfilling their energy requirements using renewable sources such as solar PV and battery storage. Electric vehicles are gaining popularity and are even being promoted by governments. The TAB and DAB inverters will be a useful addition for smart grid solutions as they provide the functionalities of a solid-state transformer. Due to their active nature of operation, they can provide both the consumer and the utility a far superior controllability and significantly better power quality over the existing passive devices.

9.3 Future Work

The developed TAB system can be improved for future work. Some of the future improvements on the TAB inverter are shown in the following sections.

9.3.1 Protective devices

Two of the above-mentioned systems galvanically isolate the household from the grid connection. This causes the grounding link between the distribution transformer and the household neutral to be severed. Even though this provides immunity for line to ground faults, the system can become hazardous if any live or neutral component of the system makes contact with the ground. In the typical household system, if the live component is grounded this will be detected by a RCCB which will break the circuit once a fault current exceeds 30 mA. In the TAB however, the neutral side of the converter output will have to be firmly grounded at the output of the converter to allow the RCCB to detect and interrupt any fault currents exceeding 30mA.

9.3.2 Energy storage and independent operation

The TAB can be used with a battery storage for independent operation with the grid. A battery storage can be connected at the household side DC bus to provide power to the household in times where the grid power is not available. Batteries can also be charged using the PV array to provide power to the household during nighttime as a demand side response to reduce the nighttime peak.

9.3.3 Physical implementation

This thesis provides only design and simulation results for the TAB and DAB systems. It needs to be physically implemented in order get its maximum benefit and to understand its behavior in actual conditions. The high frequency transformer design is also necessary for the physical implementation. The use of digital controllers and deadtime of the switching devices will introduce additional complexities and will have to be taken into consideration during implementation.

Switching losses associated with the conversion modules can reduce the efficiency of the system. The snubber circuits can be implemented for the switching devices with soft switching to reduce the losses and device ratings. As the transformer ratios of the developed systems are identical, soft switching can be obtained by tuning

the snubber capacitances with the transformer leakage inductances. This will reduce the losses present at hard switching.

9.3.4 Reactive power flow

The dq controller used at the grid tie inverter allows active and reactive power to be controlled independently. If the system is used with a battery storage, the output inverter can be configured to provide active and reactive power to the grid during nighttime for voltage regulation. The electricity utilities can have a certain level of control over this to obtain reactive power to the grid whenever required.

Reference List

[1] Public Utilities Commission of Sri Lanka, “Net Metering Development in Sri Lanka,” 2015.

[2] CEB, “CEB Statistical Digest,” 2016. .

[3] S. V. S. Kumary, V. A. Aman, M. Than, G. M. Shafiullah, and A. Stojcevski, “Modelling and Power quality analysis of a Grid-connected Solar PV System,” no. October, pp. 5–10, 2014.

[4] Mathworks, “Single-Phase, 240 Vrms, 3500 W Transformerless Grid-Connected PV Array,” *Matlab R2017b Documentation*. [Online]. Available: https://www.mathworks.com/help/physmod/sps/examples/single-phase-240-vrms-3500-w-transformerless-grid-connected-pv-array.html.

[5] L. Ma *et al.*, “Leakage Current Analysis of Single-phase Transformer-less Grid -connected PV Inverters,” in *IECON*, 2015, pp. 887–892.

[6] T. Kheng, S. Freddy, N. A. Rahim, W. Hew, and H. S. Che, “Comparison and Analysis of Single-Phase Transformerless Grid-connected PV Inverters,” vol. 29, no. 10, p. 8993, 2014.

[7] V. Salas, E. Olías, M. Alonso, F. Chenlo, and A. Barrado, “DC current injection into the network from PV grid inverters,” *Conf. Rec. 2006 IEEE 4th World Conf. Photovolt. Energy Conversion, WCPEC-4*, vol. 2, no. June, pp. 2371–2374, 2007.

[8] B. Liu, Y. Zha, T. Zhang, and S. Chen, “Solid state transformer application to grid connected photovoltaic inverters,” *2016 Int. Conf. Smart Grid Clean Energy Technol. ICSGCE 2016*, pp. 248–251, 2017.

[9] N. C. Foureaux, L. Adolpho, S. M. Silva, J. A. D. S. Brito, and B. D. J. Cardoso Filho, “Application of solid state transformers in utility scale solar power plants,” *2014 IEEE 40th Photovolt. Spec. Conf. PVSC 2014*, vol. 2, pp. 3695–3700, 2014.

[10] S. Falcones, X. Mao, and R. Ayyanar, “Topology comparison for solid state

transformer implementation," *IEEE PES Gen. Meet. PES 2010*, pp. 1–8, 2010.

[11] A. Q. Huang and R. Burgos, "Review of Solid-State Transformer Technologies and Their Application in Power Distribution Systems," *IEEE J. Emerg. Sel. Top. Power Electron.*, vol. 1, no. 3, pp. 186–198, 2013.

[12] R. W. a a De Doncker, D. M. Divan, and M. H. Kheraluwala, "A three-phase soft-switched high-power-density DC/DC converter for high-power applications," *IEEE Trans. Ind. Appl.*, vol. 27, no. 1 pt 1, pp. 63–73, 1991.

[13] D. Segaran, D. G. Holmes, and B. P. McGrath, "Enhanced load step response for a bidirectional DCDC converter," *IEEE Trans. Power Electron.*, vol. 28, no. 1, pp. 371–379, 2013.

[14] S. Poshtkouhi *et al.*, "A dual-active-bridge based bi-directional micro-inverter with integrated short-term Li-Ion ultra-capacitor storage and active power smoothing for modular PV systems," *2014 IEEE Appl. Power Electron. Conf. Expo. - APEC 2014*, pp. 643–649, 2014.

[15] H. Tao, A. Kotsopoulos, J. L. Duarte, and M. A. M. Hendrix, "A soft-switched three-port bidirectional converter for fuel cell and supercapacitor applications," *PESC Rec. - IEEE Annu. Power Electron. Spec. Conf.*, vol. 2005, no. 1, pp. 2487–2493, 2005.

[16] S. Falcones, R. Ayyanar, and X. Mao, "A DC-DC Multiport-converter-based solid-state transformer integrating distributed generation and storage," *IEEE Trans. Power Electron.*, vol. 28, no. 5, pp. 2192–2203, 2013.

[17] N. A. Rahim, K. Chaniago, and J. Selvaraj, "Single-phase seven-level grid-connected inverter for photovoltaic system," *IEEE Trans. Ind. Electron.*, vol. 58, no. 6, pp. 2435–2443, 2011.

[18] F. A. Ramírez and M. A. Arjona, "A Space Vector Modulation Algorithm for a Grid-Connected Single-Phase Seven Level Inverter," pp. 2–7.

[19] H. Dehbonei, C. V. Nayar, and L. Borle, "A novel modulation technique for a single phase H-bridge inverter," *Int. J. Electron.*, vol. 91, no. 1, pp. 41–55,

2004.

[20] Mitsubishi Electric, “PV-UD185MF5 185Wp Datasheet.” [Online]. Available: https://www.mitsubishielectricsolar.com/images/uploads/documents/specs/UD5_spec_sheet_185W.pdf.

[21] S. M. Ferdous, M. A. Mohammad, F. Nasrullah, A. M. Saleque, and A. Z. M. S. Muttalib, “Design and simulation of an open voltage algorithm based maximum power point tracker for battery charging PV system,” *2012 7th Int. Conf. Electr. Comput. Eng.*, no. 2, pp. 908–911, 2012.

[22] B. O. Kang and J. H. Park, “Kalman filter MPPT method for a solar inverter,” *2011 IEEE Power Energy Conf. Illinois, PECI 2011*, 2011.

[23] T. Esram and P. L. Chapman, “Comparison of Photovoltaic Array Maximum Power Point Tracking Techniques,” *IEEE Trans. Energy Convers.*, vol. 22, no. 2, pp. 439–449, 2007.

[24] Research and Development branch of CEB, “Study on Harmonics Generation by Grid Connected PV Inverters,” 2015.

[25] IEEE Power and Energy Society, “IEEE Recommended Practice and Requirements for Harmonic Control in Electric Power Systems,” 2014.

[26] Transmission Division of Ceylon Electricity Board, “Grid Code,” 2015.

[27] IEEE Standards Coordinating Committee 21, “IEEE Guide for Conducting Distribution Impact Studies for Distributed Resource Interconnection,” 2013.

[28] Resource Management Associates (RMA) Pvt Ltd and GEO-NET Umweltconsulting GmbH of Germany, “Technical Assistance Consultant’s Report on Sri Lanka Clean Energy and Network Efficiency Improvement Project(Wind and Solar Resource Assessment),” 2013.

[29] A. Algaddafi, K. Elnaddab, A. Al, and A. N. Esgiar, “Comparing the Performance of Bipolar and Unipolar Switching Frequency to Drive DC-AC Inverter,” 2016.

[30] U. A. Miranda, M. Aredes, and L. G. B. Rolim, “A DQ synchronous reference frame control for single-phase converters,” *PESC Rec. - IEEE Annu. Power Electron. Spec. Conf.*, vol. 2005, pp. 1377–1381, 2005.

[31] J. F. Sultani, J. A. Gow, and E. Tez, “Modelling, Design and Implementation of D-Q Control in Single-Phase Grid-Connected Inverters for Photovoltaic Systems Used in Domestic Dwellings,” DE MONTFORT UNIVERSITY 2013, 2013.

[32] G. Franceschini, E. Lorenzani, C. Tassoni, and A. Bellini, “Synchronous reference frame grid current control for single-phase photovoltaic converters,” *Conf. Rec. - IAS Annu. Meet. (IEEE Ind. Appl. Soc.)*, pp. 1–7, 2008.

[33] B. Crowhurst, E. F. El-Saadany, L. El Chaar, and L. A. Lamont, “Single-phase grid-tie inverter control using DQ transform for active and reactive load power compensation,” *PECon2010 - 2010 IEEE Int. Conf. Power Energy*, pp. 489–494, 2010.

[34] C. Transmission Planning Branch, “Transmission System Expansion Plan 2017-2020,” 2017.

[35] Teshmont Consultants LP, “Transformer Modelling Guide,” 2014.

[36] K. H. Ahmed, S. J. Finney, and B. W. Williams, “Passive filter design for three-phase inverter interfacing in distributed generation,” *5th Int. Conf. Compat. Power Electron. CPE 2007*, vol. XIII, no. 2, pp. 49–58, 2007.

[37] A. Reznik, M. G. Simoes, A. Al-Durra, and S. M. Muyeen, “LCL filter design and performance analysis for small wind turbine systems,” *2012 IEEE Power Electron. Mach. Wind Appl.*, pp. 1–7, 2012.

[38] Manish Bhardwaj and B. Subharmanya., “PV Inverter Design Using Solar Explorer Kit,” 2013.

[39] K. George, “Design and Control of a Bidirectional Dual Active Bridge DC-DC Converter to Interface Solar , Battery Storage , and Grid-Tied Inverters,” 2015.

[40] M. H. Kheraluwala, D. W. Novotny, and D. M. Divan, “Design considerations for high power high frequency transformers,” *21st Annual IEEE Conference on Power Electronics Specialists*. pp. 734–742, 1990.

[41] G. Waltrich, J. L. Duarte, M. A. M. Hendrix, and J. J. H. Paulides, “Three-port bi-directional converter for electric vehicles : focus on high-frequency coaxial transformer Three-Port Bi-directional Converter for Electric Vehicles : Focus on High-Frequency Coaxial Transformer,” no. March, pp. 25–28, 2010.

[42] S. Inoue and H. Akagi, “A bidirectional isolated dc-dc converter as a core circuit of the next-generation medium-voltage power conversion system,” *IEEE Trans. Power Electron.*, vol. 22, no. 2, pp. 535–542, 2007.

[43] P. Systems, “Design of a Three-port Solid State Transformer for High Power applications Guirguis Zaki Guirguis Abdelmessih,” 2015.

[44] D. S. Segaran, “Dynamic Modelling and Control of Dual Active Bridge Converters for Smart Grid Applications,” 2013.

[45] D. Segaran, B. P. McGrath, and D. G. Holmes, “Adaptive dynamic control of a bi-directional DC-DC converter,” *2010 IEEE Energy Convers. Congr. Expo.*, pp. 1442–1449, 2010.

[46] C. Zhao, S. D. Round, and J. W. Kolar, “An isolated three-port bidirectional dc-dc converter with decoupled power flow management,” *IEEE Trans. Power Electron.*, vol. 23, no. 5, pp. 2443–2453, 2008.

[47] S. Uddin, H. Shareef, A. Mohamed, and M. A. Hannan, “An analysis of harmonics from LED lamps,” *2012 IEEE Int. Power Eng. Optim. Conf. PEOCO 2012 - Conf. Proc.*, pp. 182–186, 2012.

Appendix A: PV array datasheet

YL 280 P-35b / 1970x990 SERIES

ELECTRICAL PARAMETERS

Electrical parameters at STC (1,000 W/m², 25°C, AM 1.5 according to EN 60904-3)

Module type		YL 260 P-35b	YL 265 P-35b	YL 270 P-35b	YL 275 P-35b	YL 280 P-35b
Power output	[W]	260.0	265.0	270.0	275.0	280.0
Power output tolerances	[%]	+/- 3	+/- 3	+/- 3	+/- 3	+/- 3
Module Efficiency	[%]	13.3	13.6	13.8	14.1	14.4
Voltage at Pmax, V_{mpp}	[V]	35.0	35.3	35.3	35.5	35.5
Current at Pmax, I_{mpp}	[A]	7.43	7.50	7.65	7.75	7.89
Open circuit voltage V_{oc}	[V]	44.6	44.6	44.8	45.0	45.0
Short circuit current I_{sc}	[A]	8.04	8.15	8.20	8.30	8.35
Max. system Voltage	[V]			1,000 VDC		

Parameters of the thermal characteristics

NOCT (Nominal Operating Cell Temperature)	[°C]	46 +/- 2
Temperature coefficient beta of I_{sc}	[1/K]	+ 0.0006
Temperature coefficient alpha of V_{oc}	[1/K]	- 0.0037
Temperature coefficient gamma of P_{mpp}	[1/K]	- 0.0045

MECHANICAL PARAMETERS

Dimensions (length [mm] / width [mm] / thickness [mm])	1,970 / 990 / 50
Thickness with junction box [mm]	50
Weight [kg]	26.0
Junction box (manufacturer / protection degree / number of diodes)	CIXI / IP65 / 6
Junction box dimensions (length / width / thickness [mm])	151 / 122 / 25
Positive cable & negative cable (manufacturer / length [mm] / cable cross-section [mm²])	CIXI / 1,200 / 4.0
Plug connector (manufacturer / type / protection degree)	MC4 / UV resistance and self-locking / IP67
Front cover (material / thickness [mm])	Tempered Glass, 4.0mm
Cell type (quantity / technology)	72 / polycrystalline / 156 x 156
Encapsulation materials	Ethylene Vinyl Acetate (EVA)
Rear cover (material / thickness [mm])	Le - PET - PVDF / 0.287
Frame (material)	robust anodized aluminum alloy

OPERATING CONDITIONS

Operating temperature [°C]	- 40 to + 85
Max. wind load / Max. snow load [Pa]	2.4K / 5.4K

PACKAGING

Number of modules per box	21
Box size (length [mm] / width [mm] / depth [mm])	1,995 / 1,130 / 1,131
Box Gross weight in kg	586
Boxes per pallet	1

IV CURVES

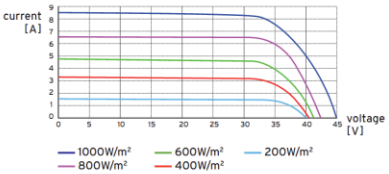

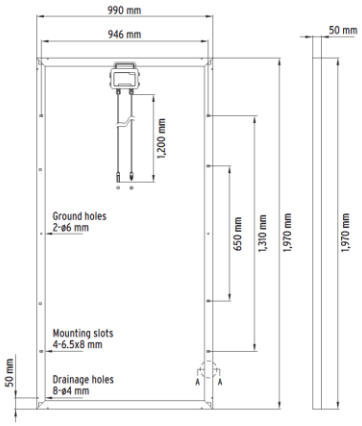

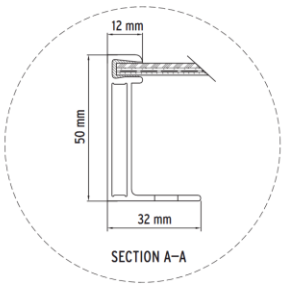

Electrical equipment, check with your installer

* The data does not refer to a single module and they are not part of the offer, they serve for comparison only to different module types.

Yingli Green Energy Holding Co. Ltd.
commerce@yinglisolar.com
0086 - (0)312 - 8929802

Subject to modifications and errors

DS-YL280P-35b-EU-EN-200908-A153-v01

www.yinglisolar.com

YINGLI SOLAR
Power Your Life

Appendix B: Simulink model -Transformerless inverter

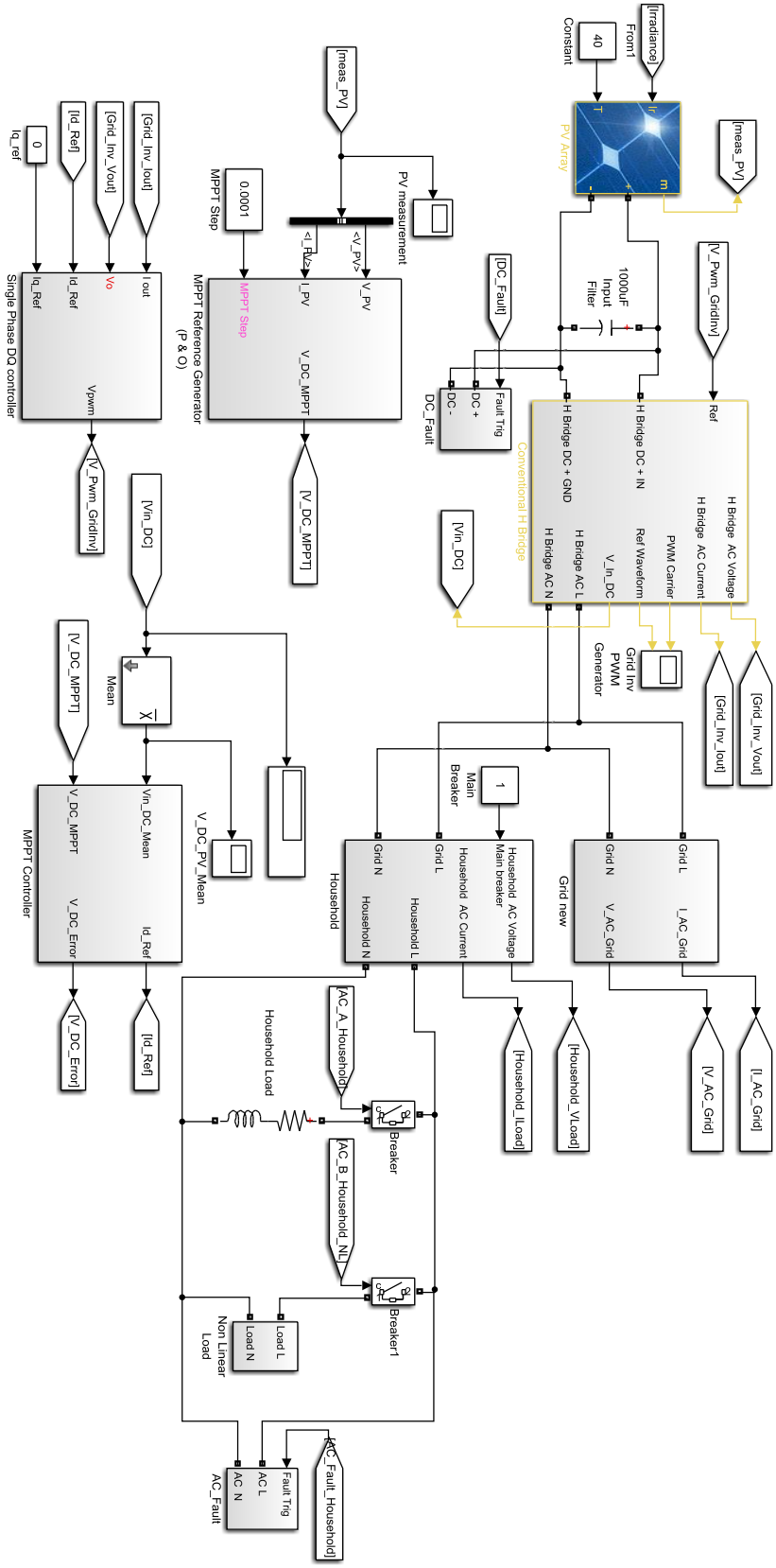

Appendix C: Simulink model-DAB inverter (load at grid side)

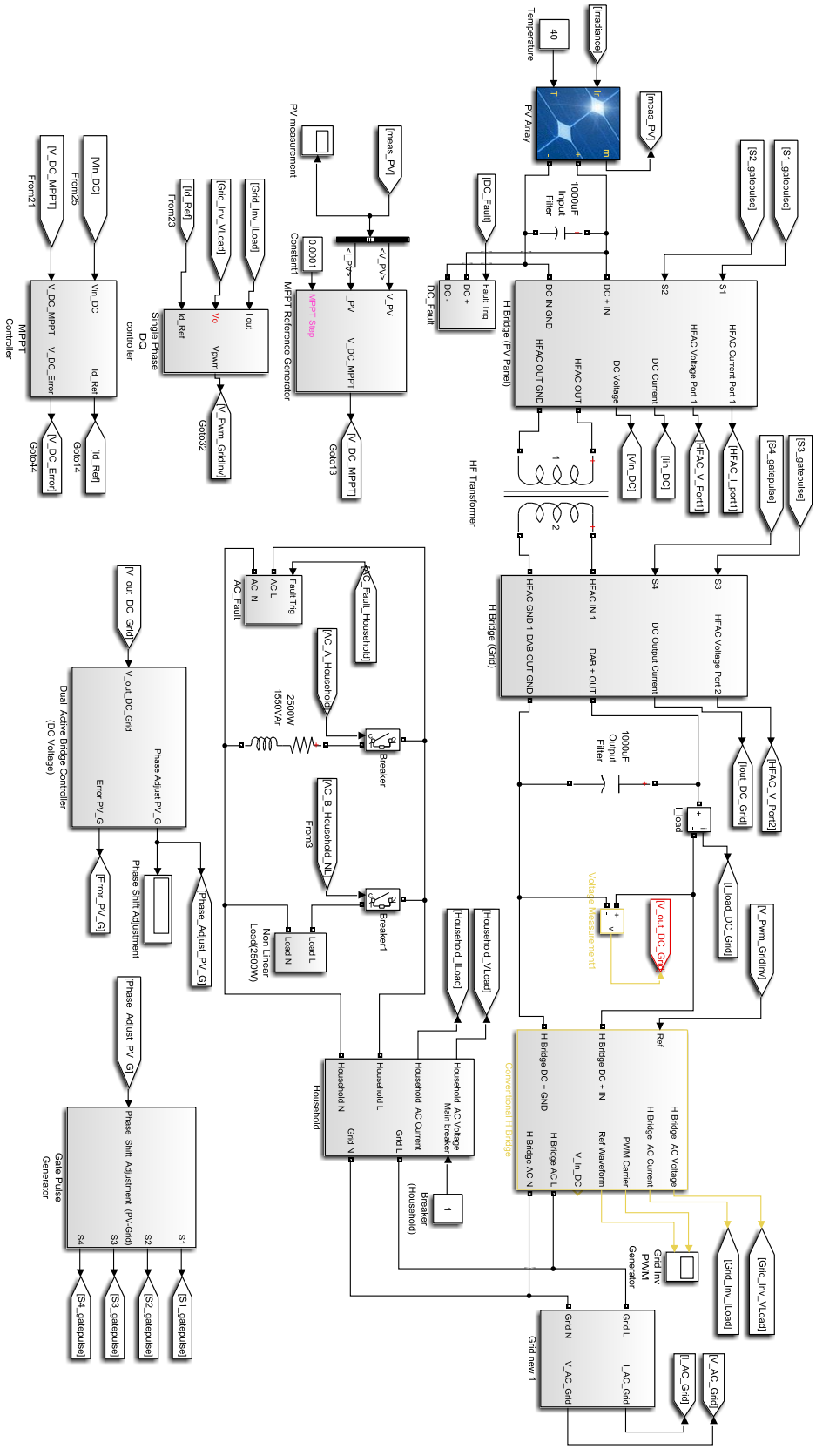

Appendix D: Simulink model-DAB inverter (load at PV array side)

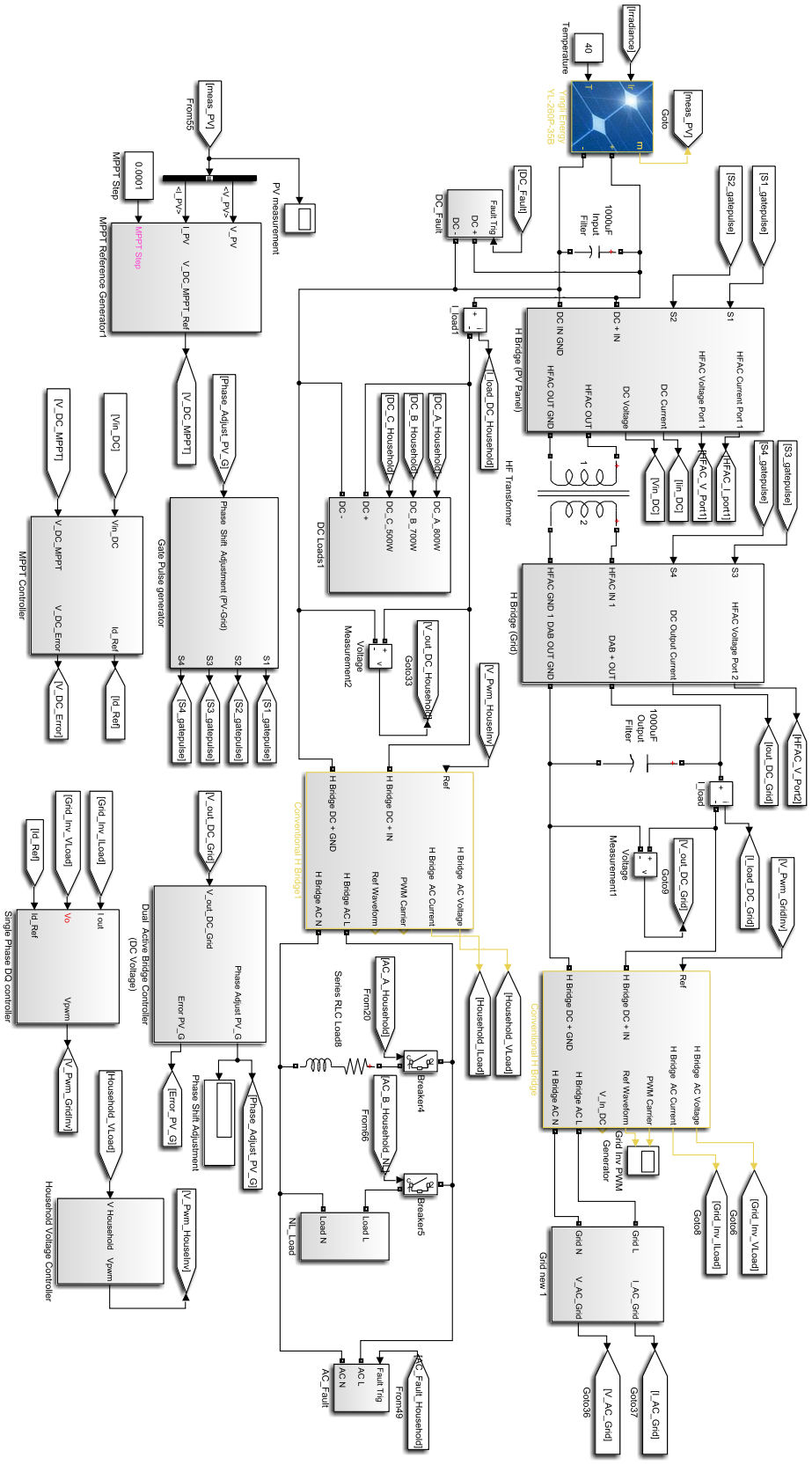

Appendix E: MATLAB code for the mathematical model of the TAB

```
clear all
clc
syms n t
syms V_h % comment out when plotting household side voltage

%no of Fourier terms

N=30;

%winding resistances

R_pv=10e-3;
R_h=10e-3;
R_g=10e-3;

%leakage inductances

f=20000;
L_pv=25e-6;
L_h=25e-6;
L_g=25e-6;

%phase shifts

delta_pv=30;
delta_g=60;
delta_h=70;

RL_g=10;
RL_h=10;
C_g=1e-3;
C_h=1e-3;

V_pv=420;
% V_h=350; %uncomment when plotting currents
V_g=350;

%Hz to rad/s

Ws=2*pi*f;
%W=(2*n+1)*Ws;

%delta pi transformation

Zpvh=((R_pv+j*Ws*L_pv)*(R_h+j*Ws*L_h)+(R_pv+j*Ws*L_pv)*(R_g+j*Ws*L_g
)+(R_h+j*Ws*L_h)*(R_g+j*Ws*L_g))/(R_g+j*Ws*L_g);
Zpvg=((R_pv+j*Ws*L_pv)*(R_h+j*Ws*L_h)+(R_pv+j*Ws*L_pv)*(R_g+j*Ws*L_g
)+(R_h+j*Ws*L_h)*(R_g+j*Ws*L_g))/(R_h+j*Ws*L_h);
Zgh=((R_pv+j*Ws*L_pv)*(R_h+j*Ws*L_h)+(R_pv+j*Ws*L_pv)*(R_g+j*Ws*L_g)
+(R_h+j*Ws*L_h)*(R_g+j*Ws*L_g))/(R_pv+j*Ws*L_pv);

Rpvh=real(Zpvh);
```

```
Rpvg=real(Zpvg);
Rgh=real(Zgh);

Lpvh=imag(Zpvh)/Ws;
Lpvg=imag(Zpvg)/Ws;
Lgh=imag(Zgh)/Ws;

%deg to rad transformation

d_pv=delta_pv*pi/180;
d_h=delta_h*pi/180;
d_g=delta_g*pi/180;

%mathermatical model

Zn_pvh=(sqrt(Rpvh^2+((2*n+1)*Ws*Lpvh)^2));
Psin_pvh=(atan(((2*n+1)*Ws*Lpvh)/Rpvh));
Zn_gh=(sqrt(Rgh^2+((2*n+1)*Ws*Lgh)^2));
Psin_gh=(atan(((2*n+1)*Ws*Lgh)/Rgh));
Zn_pvg=(sqrt(Rpvg^2+((2*n+1)*Ws*Lpvg)^2));
Psin_pvg=(atan(((2*n+1)*Ws*Lpvg)/Rpvg));



IL_pvh_tot=((1/(2*n+1))*((((V_pv)/Zn_pvh)*sin((2*n+1)*(Ws*t-d_pv)-
Psin_pvh))-(((V_h)/(Zn_pvh))*sin((2*n+1)*(Ws*t-d_h)-Psin_pvh))));
IL_pvh=(4/pi)*symsum(IL_pvh_tot, n, 0, N);

IL_pvg_tot=((1/(2*n+1))*((((V_pv)/Zn_pvg)*sin((2*n+1)*(Ws*t-d_pv)-
Psin_pvg))-(((V_g)/(Zn_pvg))*sin((2*n+1)*(Ws*t-d_g)-Psin_pvg))));
IL_pvg=(4/pi)*symsum(IL_pvg_tot, n, 0, N);

IL_gh_tot=-((1/(2*n+1))*((((V_h)/Zn_gh)*sin((2*n+1)*(Ws*t-d_h)-
Psin_gh))-(((V_g)/(Zn_gh))*sin((2*n+1)*(Ws*t-d_g)-Psin_gh))));
IL_gh=(4/pi)*symsum(IL_gh_tot, n, 0, N);

%transformer output and input currents

IL_pv=(IL_pvg+IL_pvh);
IL_h=(IL_pvh+IL_gh);
IL_g=(IL_pvg-IL_gh);

IL_pv_sW_tot=(1/(2*n+1))*sin((2*n+1)*(Ws*t-d_pv));
IL_pv_sW=(4/pi)*symsum(IL_pv_sW_tot, n, 0, N);

IL_h_sW_tot=(1/(2*n+1))*sin((2*n+1)*(Ws*t-d_h));
IL_h_sW=(4/pi)*symsum(IL_h_sW_tot, n, 0, N);

IL_g_sW_tot=(1/(2*n+1))*sin((2*n+1)*(Ws*t-d_g));
IL_g_sW=(4/pi)*symsum(IL_g_sW_tot, n, 0, N);

%converter output and input currents

IL_pv_out=IL_pv_sW*IL_pv;
```

```
IL_h_out=IL_h_sW*IL_h;
IL_g_out=IL_g_sW*IL_g;

I_h_simp_tot=(1/(2*n+1)^2)*((V_pv*cos((2*n+1)*(d_pv-
d_h)+Psin_pvh)/(Zn_pvh))-
(V_h*(((cos(Psin_pvh))/(Zn_pvh))+((cos(Psin_gh))/(Zn_gh))))+(V_g*cos
((2*n+1)*(d_g-d_h)+Psin_gh)/(Zn_gh)));
I_h_simp=(8/(pi^2))*symsum(I_h_simp_tot, n, 0, N);

I_g_simp_tot=(1/(2*n+1)^2)*((V_pv*cos((2*n+1)*(d_pv-
d_g)+Psin_pvg)/(Zn_pvg))-
(V_g*(((cos(Psin_pvg))/(Zn_pvg))+((cos(Psin_gh))/(Zn_gh))))+(V_h*cos
((2*n+1)*(d_h-d_g)+Psin_gh)/(Zn_gh)));
I_g_simp=(8/(pi^2))*symsum(I_g_simp_tot, n, 0, N);

% fplot(IL_pv,[0,0.0002])  %uncomment to plot currents
% hold all
%

%household side and grid side voltages

V_h_c = -((V_h)/(RL_h*C_h))+(1/C_h)*IL_h_out;           %comment out
when plotting currents
V_h_csimplfd = -((V_h)/(RL_h*C_h))+(1/C_h)*I_h_simp;     %comment
out when plotting currents
%
% V_g_c = -((V_g)/(RL_g*C_g))+(1/C_g)*IL_g_out;
% V_g_csimplfd = -((V_g)/(RL_g*C_g))+(1/C_g)*I_g_simp;
%
%
opts = odeset('MaxStep',50e-8);
F = matlabFunction(V_h_c,'vars',{'t','V_h'});
[t,V_h] = ode113(F,[0 0.2],0,opts);


plot(t,V_h)
hold all
```

Appendix F: Simulink model -TAB inverter